Modeling and simulation of flow in cerebral aneurysms

Julia Mikhal

De promotiecommissie:

Voorzitter en secretaris:

Prof. dr. ir. A.J. Mouthaan	Universiteit Twente

Promotoren:

Prof. dr. ir. B.J. Geurts	Universiteit Twente
Prof. dr. ir. C.H. Slump	Universiteit Twente

Leden:

Prof. dr. ing. V. Armenio	Università degli Studi di Trieste
Prof. dr. S.A. van Gils	Universiteit Twente
Prof. dr. J.G.M. Kuerten	Universiteit Twente
Prof. dr. C.B.L.M. Majoie	Academisch Medisch Centrum Amsterdam
Prof. dr. A.E.P. Veldman	Rijksuniversiteit Groningen
Prof. dr. ir. F.N. van de Vosse	Technische Universiteit Eindhoven

MESA+ INSTITUTE FOR NANOTECHNOLOGY

UNIVERSITY OF TWENTE.

MIRA BIOMEDICAL TECHNOLOGY AND TECHNICAL MEDICINE

The research presented in this thesis was done in the group Multiscale Modeling and Simulation (Dept. of Applied Mathematics), in collaboration with the group Signals and Systems (Dept. of Electrical Engineering), Faculty EEMCS, University of Twente, The Netherlands.

Computing resources were granted by the National Computing Facilities Foundation (NCF), with financial support from the Dutch Organization for Scientific Research (NWO).

Printed by Wöhrmann Print Service, Zutphen, The Netherlands.
Cover photo ‘Lights and Water’ © James Adamson.

ISBN : 978-90-365-3433-8 DOI : 10.3990/1.9789036534338

MODELING AND SIMULATION OF FLOW IN CEREBRAL ANEURYSMS

PROEFSCHRIFT

ter verkrijging van
de graad van doctor aan de Universiteit Twente,
op gezag van de rector magnificus,
prof. dr. H. Brinksma,
volgens besluit van het College voor Promoties
in het openbaar te verdedigen
op vrijdag 19 oktober 2012 om 12:45 uur

door

Iuliia Olegivna Mikhal
geboren op 6 juni 1984
te Kharkiv, Oekraïne

Dit proefschrift is goedgekeurd door de beide promotoren:

Prof. dr. ir. B.J. Geurts en Prof. dr. ir. C.H. Slump

To my parents

Contents

Chapter 1
Introduction

There is a growing medical interest in the prediction of flow and forces inside cerebral aneurysms [48, 103], with the ultimate goal of supporting medical procedures and decisions by presenting viable scenarios for intervention. The clinical background of cerebral aneurysms and possible hemorrhages is well introduced in the literature such as [93, 101]. These days, with the development of high-precision medical imaging techniques, the geometry and structure of blood vessels and possible aneurysms that have formed, can be determined for individual patients. To date, surgeons and radiologists have to make decisions about possible treatment of an aneurysm based on size, shape and location criteria alone. In this thesis we focus on the role of Computational Fluid Dynamics (CFD) for identifying and classifying therapeutic options in the treatment of aneurysms.

CFD allows to add qualitative and quantitative characteristics of blood flow inside the aneurysm to the complex process of medical decision making. We contribute to this by computing the precise patient-specific pulsatile flow in all spatial and temporal details, using a so-called 'Immersed Boundary' (IB) method. This requires a number of steps, from preparing the raw medical imagery to define the complex patient-specific flow domain, to the execution of high-fidelity simulations. Subsequently, detailed interpretation of the consequences of the flow should be given jointly by medical experts and CFD specialists in terms of flow visualization and quantitative measures of relevance to medical practice. We compute the flow inside the aneurysm to predict high and low stress regions, indicative of possible growth of an aneurysm. We also visualize vortical structures in the flow indicating the quality of local blood circulation. We show that, as the size of the aneurysm increases, qualitative changes in the flow behavior can arise, which express themselves as high-frequency variations in the flow and shear stresses. These rapid variations could be used to quantify the level of risk associated with the growing aneurysm. Such computational modeling may lead to a better understanding of the progressive weakening of the vessel wall and its possible rupture.

Before presenting the content of this thesis, we will briefly discuss the medical motivation of the problem, the various roles CFD can play and give an overview of numerical methods being used for blood flow simulations. Subsequently, the focus points of each chapter will be presented and finally the general outline of this thesis will be given.

Cerebral Aneurysm. Medical motivation. The medical condition known as cerebral aneurysm is one of the cardiovascular diseases that involves vessel walls of cerebral vessels. Bulge formations might develop on the vessel walls, and over time, under permanent pulsating forces, the aneurysm may grow further and even rupture. The degradation of endothelial cells in the vessel walls is often associated with regions of relatively low shear stress [9] while locations of relatively high shear stress could be important for initial formation of a bulge [84]. Commonly, cerebral aneurysms are located in or near the Circle of Willis [101] – the central vessel network for the supply of blood to the human brain. The risk-areas are at 'T' and 'Y'-shaped junctions in the vessels [34]. Treatment of cerebral aneurysms often involves insertion of a slender coil. This coiling procedure represents considerable risk during a surgical intervention, as well as uncertainty about the long-term stability of coiled aneurysms [86, 94]. Blood vessels and aneurysms are rather complex by their structure and geometrical shapes. The walls of blood vessels contain several layers of different types of biological cells, which provide elasticity to the vessels and determine their compliance [76]. The shape of cerebral aneurysms developing in patients can be inferred by using several techniques such as CTA (Computed Tomographic Angiography), DSA (Digital Subtraction Angiography) and 3DRA (Three-Dimensional Rotational Angiography) [64]. In these procedures a small part of the brain is scanned, and aneurysms even of a size less than 3 *mm* can be observed [8, 95]. These techniques allow a reconstruction of three-dimensional arteries and aneurysms and hence an approximate identification of the blood vessels and parts of the soft tissue in the scanned volume.

Computational Fluid Dynamics. The tremendous potential of CFD in supporting medical decisions and proposing therapeutic options in the treatment of cerebral aneurysms, was already anticipated in [57]. The value of numerical simulations for treating aneurysms will likely increase further with better quantitative understanding of hemodynamics in cerebral blood flow. A primary challenge for any CFD method, whether it is a body-fitted method [35] or an IB method [37, 62, 73], is to capture the flow near solid-fluid interfaces. In this region the highest velocity gradients may occur, leading to correspondingly highest levels of shear stress, but also potentially highest levels of numerical error. In methods employing body-fitted grids, the quality of predictions is directly linked to the degree to which grid-lines can be orthogonal to the solid-fluid interface and to each other. Also, variation in local mesh sizes and shapes of adjacent grid cells is a factor determining numerical error. The generation of a suitable grid is further complicated as the raw data that define the actual aneurysm geometry

often require considerable preprocessing steps before any grid can be obtained. These steps include significant smoothing, segmentation and geometric operations eliminating small side vessels that are felt not to be too important for the flow. On the positive side, the main benefit of a body-fitted approach is that discrete variables are situated also at the solid-fluid interface, which makes implementation of no-slip boundary conditions quite straightforward. Hence, in body-fitted approaches the no-slip property can be accurately imposed, but only on a 'pre-processed' smoothed and often somewhat altered geometry [15, 24]. These finite element or finite volume based approaches can be used to predict the patient's main flow structures of clinical value as suggested by [14, 15, 34, 39].

Numerical method. Immersed Boundary Method. A significant amount of work has been done on simulation of flow in the brain and in the cardiovascular system [6, 14, 28, 38, 48, 71, 76]. As an alternative to the body-fitted approach, the IB method was designed primarily for capturing viscous flow in domains of realistic complexity [73]. In the IB approach which we adopt, the actual geometry of the aneurysm can be extracted directly from the voxel information in the raw medical imagery, without the need for smoothing of the geometry. Grid generation is no issue for IB methods since the geometry of the flow domain is directly immersed in a Cartesian grid. The location of the solid-fluid interface is known only up to the size of a grid cell, and the shape of the interface is approximated using a 'staircase' representation, stemming from the fact that any grid cell is labeled either entirely 'solid' or entirely 'fluid'. Refinements in which a fraction between 0 and 1 of a cell can be fluid-filled [18] are not taken into consideration here. The medical imagery from which we start has a spatial resolution that is not too high when small-scale details are concerned. This calls for a systematic assessment of the sensitivity of predictions to uncertainties in the flow domain [61]. Using the staircase approximation, the problem of capturing near-interface properties can only be addressed by increasing the spatial resolution. This also gives an insight into the error-reduction by systematic grid-refinement for flow in complex geometries.

Thesis contents. In this thesis we present a numerical model for the simulation of blood flow inside cerebral aneurysms. We illustrate the process of predicting flow and forces that arise in vessels and aneurysms, starting from patient-specific data obtained using medical imaging techniques. Once the three-dimensional geometry is reconstructed, we discuss fluid properties of blood which allows to compute the flow. The flow of an incompressible Newtonian fluid in the human brain is simulated by using a volume penalizing IB method, in which the aneurysm geometries are represented by the so-called masking function. We impose pulsatile flow forcing, based on direct measurement of the mean flow velocity in a vessel during a cardiac cycle and focus on effects due to changes in the flow regime. In slow or very viscous flows the pulsatile forcing dominates the fluid dynamical response, while at faster or less viscous flows the incompressible flow shows a transition to complex flow coined 'turbulent' by

Ferguson [23]. The natural nonlinearity of the governing equations dominates the pulsatile flow forcing at higher flow rates. We consider a full range of physiologically relevant conditions and show high frequencies to emerge in the pulsatile response. The strong qualitative transitions in flow behavior and shear stress levels inside an aneurysm cavity at increased flow rates may contribute to the long-term risk of aneurysm rupture.

In brief, the main topics addressed in this thesis are:

- **IB Method: development, validation, application to model geometries.** A volume-penalizing IB method for blood flow simulations inside the human brain is developed and tested on the basis of simple model geometries. First, we validate our method for the classical case of Poiseuille flow in a cylindrical tube. Subsequently, we simulate the laminar flow inside simplified model geometries, motivated by shapes of real cerebral vessels and aneurysms. Blood is approximated as an incompressible Newtonian fluid, governed by the Navier-Stokes equations. Numerically we solve the system by means of skew-symmetric finite volume discretization, closely following [100]. A forcing term is added to the Navier-Stokes equations to represent complex geometries by immersing the tissue-fluid interfaces in the Cartesian grid. The key element of our IB method is the so-called 'masking function', which identifies fluid and solid parts of the computational domain. The masking function is a binary function, taking values '0' in the fluid (blood) part and '1' in solid (tissue) parts of the domain. Even with the coarse staircase representation of the boundaries, reliable results can be obtained at grids with about 16 grid cells across a vessel opening. The flow regime is characterized by the value of the Reynolds number (Re), which for cerebral blood flow is about $Re = 250$. We present simulations at different Reynolds numbers, analyzing changes in the flow behavior in curved vessels and in modeled aneurysms. We not only consider the developing velocity and pressure fields, but also compute shear stresses that are important in relation to the possible development of aneurysms.

- **Steady flow in realistic cerebral aneurysms, reconstructed from 3DRA data.** Moving on to realistic aneurysms, we illustrate the process of reconstructing the 3D geometry from medical images and assess the sensitivity of flow predictions to various steps of this reconstruction. A segment of the cerebrovascular system of a person suffering from a brain aneurysm was available from a recording obtained with three-dimensional rotational angiography (3DRA). The raw angiography data allows to define the masking function that represents the vessel and aneurysm shape. We apply segmentation and simplification processes to obtain the 3D geometry, containing the main vessel and an aneurysm on it. Individual voxels in the digital data form the smallest unit of localization of the solid-fluid interface. A computational cell is assigned to be 'solid' or 'fluid' on the basis of the digital imagery - in this way we generate the masking function. Further, to obtain a 'sin-

gle inflow/single outflow' representation of the main structure, we cut away parts of the geometry at some distance from the aneurysm bulge and connect the ends of the vessels with a smooth connecting tube to achieve a setting in which periodic boundary conditions can be imposed. We analyze the sensitivity of flow predictions to these cutting and connecting steps by computing the steady flow in the physiologically relevant flow regime at $Re = 250$. We analyze the sensitivity of predictions by incorporating several geometries that differ somewhat in the precise location of the cuts by which the relevant vessel segment is identified, or by the smoothness of the connecting vessel segment that is added, i.e., a smoothly differentiable and a linear connecting vessel. Due to uncertainties in the initial medical imagery we also assess the reliability of our numerical predictions by introducing 'practical bounding solutions'. Next to the basic geometry, directly reconstructed from the medical data, we consider a few slightly smaller and slightly larger bounding geometries. Numerical solutions computed in these bounding geometries appear to also bound a number of key properties of the basic solution computed in the basic geometry from above and from below. The bounding solution approach allows to present not only the basic solution but also the sensitivity range caused by limitations in the quality of the medical images.

- **Pulsatile flow simulations and pathological transition.** Numerical simulation of realistic *pulsatile* flow in cerebral aneurysms is the next important step towards medical application. This step completes a first, rough computational model that connects medical imagery to predictions of (some) clinical relevance. Pulsatile flow forcing is obtained by incorporating direct measurements of the time-dependent averaged flow velocity over the cross-section of a brain artery during a cardiac cycle. Transcranial Doppler (TCD) sonography is a non-invasive technique, which can be used to measure the flow velocity near the actual aneurysm [101]. This allows to complete a full patient-specific model as far as vessel geometry and cardiac signature are concerned. We consider a full range of physiologically relevant conditions and show that the flow undergoes a transition from an orderly state at low Reynolds numbers ($Re = 100, 200$), in which the pulsatile forcing is closely followed in time, to a complex response with strongly increased high-frequency components at higher Reynolds numbers ($Re = 400$), i.e., at higher flow rates and larger aneurysm sizes. The results obtained for the shear stress correspond to values found in literature [29, 70], thereby providing an additional validation of the computational model. The numerical reliability of the predicted transition is quantified on the basis of the bounding solutions approach. We compute the spectrum of the response of the flow by monitoring the solution at various locations and flow conditions. We quantify the significant increase of small-scale, high-frequency structures at higher Reynolds numbers. This observation of complex flow transition in case aneurysms are involved was reported in a clinical study [23]. It may have fast and inexpensive clinical screening applications in the future.

Outline. The organization of the thesis is as follows. In Chapter 2 we present the computational model, based on the Navier-Stokes equations, discuss skew-symmetric finite volume discretization and introduce the IB method for defining complex vessel and aneurysm geometries. We focus on the validation of the numerical method for the classical case of Poiseuille flow in a cylindrical pipe and for model vessels and aneurysm geometries. We establish first-order convergence with grid refinement. Also, numerical shear stresses are computed and the simulations are validated also in this respect, i.e., with reference to the derivatives of the velocity, next to validation in terms of the velocity itself. The process of reconstruction of the geometry from medical imagery is presented in Chapter 3. We illustrate steady flow inside a realistic aneurysm geometry and discuss the sensitivity of flow predictions to the reconstruction steps. In Chapter 4 we present the inclusion of realistic pulsatile flow in the computational model. We consider different flow regimes, which correspond to physiologically relevant situations ranging from 'normal' to unhealthy, high Reynolds number flow conditions. We show a strong transition from simple laminar flow with a small relevant frequency content to complex flow with many high frequencies as the Reynolds number, i.e., the flow velocity or aneurysm size, increase sufficiently. Concluding remarks and an outlook for further research are given in the last chapter.

Chapter 2
Immersed boundary method for the computation of flow in vessels and cerebral aneurysms

Abstract

A volume-penalizing immersed boundary method is presented for the simulation of laminar incompressible flow inside geometrically complex blood vessels in the human brain. We concentrate on cerebral aneurysms and compute flow in curved brain vessels with and without spherical aneurysm cavities attached. We approximate blood as an incompressible Newtonian fluid and simulate the flow with the use of a skew-symmetric finite-volume discretization and explicit time-stepping. A key element of the immersed boundary method is the so-called masking function. This is a binary function with which we identify at any location in the domain whether it is 'solid' or 'fluid', allowing to represent objects immersed in a Cartesian grid. We compare three definitions of the masking function for geometries that are non-aligned with the grid. In each case a 'staircase' representation is used in which a grid cell is either 'solid' or 'fluid'. Reliable findings are obtained with our immersed boundary method, even at fairly coarse meshes with about 16 grid cells across a velocity profile. The validation of the immersed boundary method is provided on the basis of classical Poiseuille flow in a cylindrical pipe. We obtain first order convergence for the velocity and the shear stress, reflecting the fact that in our approach the solid-fluid interface is localized with an accuracy on the order of a grid cell. Simulations for curved vessels and aneurysms are done for different Reynolds number (Re). The validation is performed for laminar flow at $Re = 250$, while the flow in more complex geometries is studied at $Re = 100$ and $Re = 250$, as suggested by physiological conditions pertaining to flow of blood in the Circle of Willis.

2.1 Introduction

Healthy blood circulation depends on many factors among which are the properties of blood itself, the size of the vessels through which blood flows and the general flow speed. The walls

of the blood vessels may become hard or weak over time, injured or infected and this can lead to different diseases such as atherosclerosis, the formation of aneurysms, thrombosis, stroke and others. Forces on vessel walls play a role in the progress of the disease, especially in the injured vessels [13]. The prediction of the flow and stresses in the course of a gradually developing disease constitutes a challenging multiscale problem. This ranges from an analysis of short-time pulsatile flow to long-term medical prognosis. We are interested particularly in flow inside small cerebral vessels and aneurysms which may gradually develop due to weakening of the vessel walls. In this chapter we show the use of an immersed boundary method to simulate incompressible Newtonian flow in complex vessels and aneurysm models. We identify resolution requirements such that numerically reliable results can be obtained for a range of physiologically relevant conditions.

Understanding flow patterns inside an aneurysm may help to describe long-term effects such as the likelihood of the growth [9] or even rupture [84] of the aneurysm, or the accelerated deterioration of the vessel wall due to low shear stress [21]. Such capability would allow a more complete planning of surgery and predict the effectiveness of certain procedures, and compare different options. Treatment of cerebral aneurysms often involves insertion of a slender coil. This procedure represents considerable risk and uncertainty about the long-term stability of coiled aneurysms [86, 94]. Numerical simulation could support decisions regarding, whether, which and how much coil to insert. It could also help in a follow-up monitoring of a patient.

A significant amount of work has been done on Computational Fluid Dynamics (CFD) of flow in the human brain and in the cardiovascular system [6, 14, 28, 38, 48, 71, 76]. As a numerical approach, the finite element method is most commonly used to represent geometries of blood vessels. Often, the data are obtained from rather coarse biomedical imagery. The highly complex geometry is defined with some uncertainty by this imagery, and some smoothing and interface approximation need to be included to allow simulation with a body-fitted approach [6, 15, 24]. As an alternative approach the immersed boundary (IB) method was designed primarily for capturing viscous flow in domains of realistic complexity [73]. In particular, we consider a volume penalization method. In this method, fluid is penalized from entering a solid part of a domain of interest by adding a suitable forcing term to the equations governing the fluid flow [42]. This method is also known as ‘fictitious domain’ method [1] and physically resembles the Darcy penalty method [79] or the Navier-Stokes/Brinkman equations for flow in porous domains [97]. Here, we consider in particular the limit in which the porous domain becomes impenetrable and flow in complex solid domains can be represented. This method is discussed as one of the ‘immersed boundary’ methods in the recent review paper by [62], and in the sequel will be referred to as ‘volume penalization immersed boundary method’, a label that was also adopted in [41].

Originally, the main motivation and application for IB methods was in simulation of the human heart by Peskin (a complete review is in [73]). Further, the IB method was widely ap-

plied in the bio-medical area. Among such applications are the modeling of biofilm processes [20], arteriolar flow [2], swimming organisms [19] and cell growth [51]. Another main sector of application of the IB method is in engineering, where classical problems are flow around a cylinder and around a road vehicle, flow in a wavy channel or inside a stirred tank [37], aerodynamics and parachute simulation by [43], acoustic waves by [81], and many others.

We present the development and application of an IB method for computing flow and shear stresses in cerebral aneurysms. As a numerical method we use the finite-volume discretization with a skew-symmetric treatment of the nonlinear convective fluxes. Flow is simulated at various flow conditions in several vessel geometries with and without aneurysm attached and shown to yield reliable results already at modest resolution. We concentrate on a generic model aneurysm with which the flow and forces are studied at a range of physiologically relevant Reynolds numbers.

The shape of cerebral aneurysms developing in patients can be inferred by using three-dimensional rotational angiography [64]. In this procedure a small volume of brain tissue can be scanned, and aneurysms even of a size less than 3 *mm* can be depicted [95]. This technique allows a reconstruction of three-dimensional arteries and aneurysms and hence an approximate identification of the fluid and the solid parts in the scanned volume. A volume-penalization IB method is applied to represent the aneurysm geometry. In the IB approach the domain is characterized by a so-called masking function, which takes the value '0' in the fluid part and '1' in solid parts of the domain. The raw angiography data allows for a simple 'staircase approximation' of the solid-fluid interface that defines the vessel and aneurysm shape. Individual voxels in the digital data form the smallest unit of localization of the solid-fluid interface. This raw information specifies the masking function in the sense that a computational cell is assigned to be 'solid' or 'fluid' on the basis of the digital imagery. We will adopt the 'staircase' geometry representation in this chapter and do not incorporate any additional smoothing of the geometry or sophisticated reconstruction methods.

For a more complete modeling of the dynamics in the vessel system, flow-structure interaction often plays a role [76]. In that case also parameters and models that characterize, e.g., mechanical properties of arterial tissue, influence of brain tissue and the influence of the cerebrospinal fluid are required. The amplitude of the wall motion in intracranial aneurysms was found to be less than 10% of an artery diameter. Despite the rather modest motion of the vessel, effects may accumulate over long time. Even modest movement can affect the vessel walls, which might play a role in possible aneurysm rupture as was hypothesized in [68]. For realistic pulsatile flows some movement of the aneurysm walls was observed during a cardiac cycle [69]. In this chapter we take a first step and restrict to developing the IB approach for rigid geometries. This allows to obtain the main flow characteristics inside relatively large cerebral aneurysms for which the relative wall movement can be neglected [48].

The type of blood flow and the resulting forces on vessel walls depend largely on the shape of the vessel and on the viscosity of blood. These elements vary from one person to another,

which makes the precise blood flow per heart beat a patient-specific characteristic that is hard to obtain. Rather, the patient's main flow structures that characterize the general type of blood motion and associated forces appear accessible by simulation and modeling. These are computational predictions, leading to patient-specific results of clinical value as suggested by [14, 15, 34, 39]. The distribution of shear stresses at the vessel wall and the flow pattern inside the aneurysm are considered to be relevant to characterizing the general quality of circulation. Regions of high and low shear stress are often visualized as potential markers for aneurysm growth. High shear stress levels were reported near the 'neck' of a saccular aneurysm, and may be relevant during the initiating phase [84]. Low wall shear stress has been reported to have a negative effect on endothelial cells and may be important to local remodeling of an arterial wall and to aneurysm growth and rupture [9]. A low wall shear stress may facilitate the growing phase and may trigger the rupture of a cerebral aneurysm by causing degenerative changes in the aneurysm wall. The situation is, however, more complex, as illustrated by the phenomenon of spontaneous stabilization of aneurysms after an initial phase of growth [44]. It is still very much an open issue what the precise correlation is between shear stress patterns and general circulation on the one hand, and developing medical risks such as aneurysm rupture, on the other hand. In this complex problem, hemodynamic stimuli are but one of many factors.

Cerebral aneurysms are most often located in the Circle of Willis – the central vessel network for the supply of blood to the human brain. Common risk-areas are at 'T' and 'Y'-shaped junctions in the vessels [34]. This motivates to analyze the flow in basic vessels and aneurysms by modeling them as curved cylindrical tubes to which spherical cavities are attached. This choice is not restrictive for the development of the computational approach; rather it constitutes a stepping stone problem toward simulation of actual patient-based geometries. The computational model for the simulation of blood flow through the larger vessels in the human brain is based on the incompressible Navier-Stokes equations. In this chapter we illustrate the IB approach by predicting flow in basic curved cylindrical and spherical geometries.

A primary challenge for any CFD method, whether it is a body-fitted method [35] or an IB method [37, 62, 73], is to capture the flow near solid-fluid interfaces. In this region the highest velocity gradients may occur, leading to correspondingly highest levels of shear stress, but also potentially highest levels of numerical error. In our IB approach, the actual geometry of the aneurysm can be extracted directly from the voxel information in the raw medical imagery, without the need for smoothing of the geometry. The location of the solid-fluid interface is known only up to the size of a grid cell, and the shape of the interface is approximated using a 'staircase' representation, stemming from the fact that any grid cell is labeled either entirely 'solid' or entirely 'fluid'. The problem of capturing near-interface properties can only be addressed by increasing the spatial resolution. In this chapter we study for curved vessels and model aneurysms the error-reduction upon increasing the spatial resolution. We establish

first order convergence of both the velocity field and its spatial derivatives for Poiseuille flow. Convergence is also assessed more qualitatively by systematic grid-refinement for flow in complex geometries.

Numerical accuracy was investigated extensively for a second-order IB method in [32, 50]. Simulation results for sufficiently smooth solutions were analyzed and actual second order convergence for the velocity and pressure fields was observed. No results were included for convergence of the gradient of the velocity. For a volume penalizing IB method applied to Stokes flow, i.e., very viscous, smooth flow, it was shown rigorously in [65] that first-order convergence of the velocity field can be expected, which was actually achieved in test simulations. In case the solid-fluid interface is allowed to be smoothed, or if it is already sufficiently smooth by itself, a so-called ghost-cell IB method can be shown to yield first order [7] or in selected situations second order [25] converging velocity fields for flow over an undulating channel [89]. In this reference, a direct comparison between a body-fitted and an IB method was also made for the shear stress at a selected flow condition - the results were found to be nearly identical. A comparable result may be found in [40] where a study is made of the accuracy with which turbulent wall pressure fluctuations can be predicted for sufficiently smooth surfaces. In this chapter we extend the convergence study and show first-order convergence of velocity and shear stress in complex domains also in combination with the staircase approximation of the interfaces.

The quality of predictions depends strongly on the spatial resolution that can be adopted. From a study of Poiseuille flow we will show that about 16 grid points across a velocity profile suffice to obtain reliable flow predictions, e.g., yielding an L_2-norm of the error with respect to the exact solution less than 10%. For general geometries that are not aligned with the underlying Cartesian grid, first order convergence upon grid-refinement is established. Using an energy-conserving skew-symmetric discretization by [100] the IB approach was found to provide the main flow structure and associated stress levels. Flow emerging from a steady pressure drop was investigated and the laminar velocity field and shear stress distribution were computed. Flow in curved vessels and model aneurysms is considered at $Re = 100$ and $Re = 250$ to comply with clinical data in [39, 76]. At the higher Reynolds number the flow displays some unsteadiness, consistent with findings of [24], associated with the nonlinearity in the Navier-Stokes equations, even at constant flow rate.

The organization of this chapter is as follows. In Section 2.2 we present the computational model, based on the IB method and we discuss the strategies to generate the masking function. We validate the IB method for Poiseuille flow in Section 2.3 and discuss the convergence of numerical predictions. An analysis of shear stress levels in model vessels and aneurysms is given in Section 2.4. Concluding remarks are in Section 2.5.

2.2 Computational model for flow inside cerebral aneurysms

In this section we first present the incompressible Navier-Stokes equations as the mathematical model describing the flow of blood inside the human brain (Subsection 2.2.1). Then we describe the numerical method to perform simulations of the flow (Subsection 2.2.2). A key element of the adopted IB method is the 'masking function', which identifies for each point in space whether it is 'solid material' or 'fluid domain'. In Subsection 2.2.3 we look into how masking functions are generated and introduce the model geometries.

2.2.1 Incompressible flow in complex domains

There are various approaches to model flow of blood in the human brain. A comprehensive overview is given by [76]. In one approach, the blood is approximated as a Newtonian fluid [14]. More refined models, e.g., the Carreau-Yasuda model, include the shear-thinning behavior of blood and allow to capture non-Newtonian rheology [6, 28, 38]. Under physiological flow conditions in sufficiently large arteries the non-Newtonian corrections were found to be quite small [15, 28, 38, 71]. The main flow characteristics appeared to be the same as for a Newtonian fluid at somewhat different stress and velocity levels. In this chapter we concentrate on arteries of the Circle of Willis. Typical fine-scale structures in the blood are on the order of 10^{-6} m. A length-scale that characterizes the cross section of a typical cerebral vessel inside the Circle of Willis is on the order of 10^{-3} m [39]. This difference in length-scale of three orders of magnitude motivates to approximate blood as an incompressible Newtonian fluid [76].

A common location of cerebral aneurysms within the Circle of Willis is on the internal carotid artery (ICA), where a typical volumetric flow-rate is reported to be $Q_r^* = 245 \pm 65\ ml/min$ [34], while the diameter of the ICA is approximately $D^* = 0.42 \pm 0.09\ cm$ [39], leading to a reference velocity $U_r^* = 0.2947\ m/s$ and a corresponding Reynolds number estimated as $Re = 177$ computed by $Re = U_r^* L_r^* / \nu_r^*$ in which we used as reference length the radius of the artery $L_r^* = R^* = D^*/2$ and a kinematic viscosity $\nu_r^* = 3.5 \cdot 10^{-6}\ m^2/s$ [76]. The Reynolds number *Re* is the only parameter which is required to specify the flow conditions. It quantifies the ratio between the magnitude of the (destabilizing) convective transport and the (stabilizing) viscous processes. It is well known that for relatively low Reynolds numbers flow is laminar and steady [106] under steady boundary conditions, which implies a smooth velocity and pressure field. With increasing Reynolds number the flow can develop more detailed vortical structures, e.g., associated with separated flow near abrupt changes in the shape of a vessel. A further increase in *Re* usually implies that the flow becomes unsteady even under steady boundary conditions and the range of vortices becomes much wider [106].

The range of Reynolds numbers arising in the flow in the Circle of Willis, as estimated above, corresponds to laminar, possibly unsteady flow.

The Navier-Stokes equations provide a full representation of Newtonian fluid mechanics, expressing conservation of mass and momentum. The total physical domain Ω, consists of a fluid part Ω_f and a solid part Ω_s. The interface between the two will be identified as $\partial\Omega$ at which no-slip conditions apply. The governing equations are given in dimensional form by:

$$\frac{\partial \mathbf{u}^*}{\partial t^*} + \mathbf{u}^* \cdot \nabla^* \mathbf{u}^* = -\nabla^* \left(\frac{P^*}{\rho^*}\right) + \nu^* \nabla^{*\,2} \mathbf{u}^* + \frac{\mathbf{f}^*}{\rho^*} \tag{2.1}$$

$$\nabla^* \cdot \mathbf{u}^* = 0 \tag{2.2}$$

Here $\mathbf{u}^*$ is the velocity of the fluid, ρ^* is the mass density, P^* is the pressure and $\mathbf{f}^*$ is a forcing term that will play a central role in this chapter as it is used to represent the impenetrability of complex shaped solid vessel walls, i.e., the no-slip condition. By choosing reference velocity U_r^* and reference length L_r^* we can express in a standard way reference time as $t_r^* = L_r^*/U_r^*$.

Throughout this thesis we work with a computational domain endowed with periodic boundary conditions for the velocity components. The pressure is not periodic as we allow for a mean pressure gradient to drive the flow according to an imposed flow rate. For that purpose, we decompose pressure P^* in a strictly periodic component p^* and a linear spatial dependence with amplitude a^* a function of time. This approach was pioneered, e.g., in [63]. When imposing a pressure difference, e.g., in the x-direction, this decomposition implies $P^* = p^* + a^*(t^*)x^*$. The amplitude of the mean pressure gradient $a^*(t^*)$ is adapted continuously to maintain the prescribed flow rate. The gradient of the pressure is $\nabla^* P^* = \nabla^* p^* + a^*$. Using reference density $\rho_r^* = \rho^*$ we find as reference scale for the pressure $p_r^* = (U_r^*)^2 \rho_r^*$ and for the mean pressure gradient $a_r^* = (U_r^*)^2 \rho_r^* / L_r^*$.

For the forcing term we select a direct volume penalization in which

$$\frac{\mathbf{f}^*}{\rho^*} = -\frac{1}{\varepsilon^*} H \mathbf{u}^* \tag{2.3}$$

where ε^* is a forcing time scale and H is the masking function: $H(\mathbf{x}) = 1$ if $\mathbf{x} \in \Omega_s$ and $H(\mathbf{x}) = 0$ if $\mathbf{x} \in \Omega_f$. Based on the reference velocity and length we set the reference forcing time scale as $\varepsilon_r^* = L_r^*/U_r^* = t_r^*$, which suggests that by setting $\varepsilon \ll 1$ the dimensional control parameter $\varepsilon^* = \varepsilon_r^* \varepsilon \ll \varepsilon_r^* = t_r^*$, i.e., much smaller than the reference time scale.

After choosing all reference parameters we obtain the non-dimensional form of the Navier-Stokes equations:

$$\frac{\partial \mathbf{u}}{\partial t} + \mathbf{u} \cdot \nabla \mathbf{u} = -\nabla P + \frac{1}{Re} \nabla^2 \mathbf{u} - \frac{1}{\varepsilon} H \mathbf{u} \tag{2.4}$$

$$\nabla \cdot \mathbf{u} = 0 \tag{2.5}$$

In this chapter we will consider only stationary, i.e., non moving walls. By adding the forcing to the incompressible momentum equations we formally arrive at the Brinkman equation for

flow in a porous medium with permeability related to the parameter ε [52]. Note that, with the inclusion of $\mathbf{f}$ as in (2.3) we arrive at a one-velocity field model for the flow in the entire domain Ω.

The basis of the volume penalization method is the masking function which distinguishes fluid parts from solid parts of the domain. In regions where $H = 0$ the Navier-Stokes system is solved. In the solid regions $H = 1$ and the forcing is dominant if the non-dimensional parameter ε is very small. As a result, the governing equation reduces to $\partial_t \mathbf{u} \approx -\mathbf{u}/\varepsilon$ if $|\mathbf{u}| \gg \varepsilon$ in the solid domain. Hence, any nonzero $\mathbf{u}$ is exponentially sent back to $\mathbf{0}$ on a time-scale ε. If $|\mathbf{u}| \leq \varepsilon$ the forcing is not dominant in the solid, but control over $|\mathbf{u}|$ is already obtained, i.e., $|\mathbf{u}|$ takes on negligible values in the solid. We take $\varepsilon = 10^{-10}$ relative to the dimensionless time-scale L_r/U_r in the sequel. Such low values of the control parameter ε imply that the forcing term effectively yields a Brinkman equation in which 'porous' regions are virtually impenetrable, i.e., solid material. The detailed specification and the ways of generating the masking function are presented later in Subsection 2.2.3.

2.2.2 Numerical method for simulating incompressible flow with an immersed boundary approach

In this subsection we sketch the numerical method used for the simulation of flow through complex shaped domains. First, we describe the direct numerical simulation approach and specify the volume penalization IB method afterwards.

We employ a staggered allocation of the flow variables $(\mathbf{u}, p) = (u, v, w, p)$ as basis for our flow solver [27]. In two dimensions this is sketched in Figure 2.1, where a primary grid cell with the pressure defined in the center and the Cartesian velocity components at the cell surfaces is presented. The locations at which the velocities and the pressure are stored are referred to as the velocity- and the pressure-points, respectively. In addition, we introduce the corner-points of the primary grid cells as relevant locations for the definition of the IB method later on.

The principles of conservation of mass and momentum as expressed in (2.4) and (2.5), form the basis for the discrete computational model that is used for the actual simulations. In the Navier-Stokes equations (2.4) the rate of change of momentum is obtained from the nonlinear convective flux, the linear viscous flux, the gradient of the pressure and the contribution from the forcing term. These contributions to the total flux each have a particular physical character that needs to be represented properly in the discrete formulation. In particular, the convective flux is skew-symmetric, implying that this flux only contributes to the transport of kinetic energy of the solution in physical space; it does not generate nor dissipate this energy. This property of the convective flux was the point of departure in [99] in which (then called) 'anti-symmetric' convective discretization was developed and applied

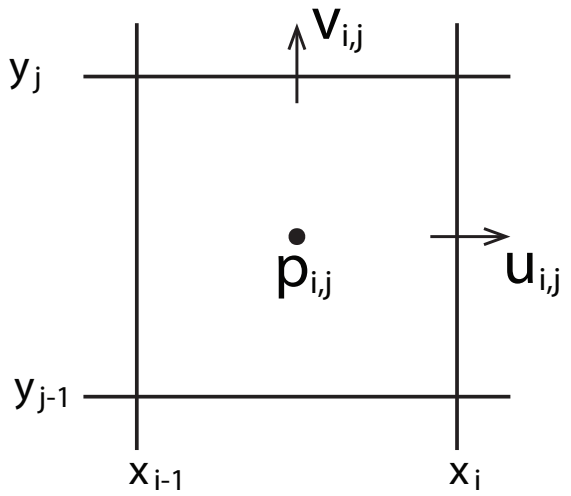

Fig. 2.1 Sketch of a primary grid cell in 2D with staggered allocation of the variables. The pressure p is in the middle of the grid cell, while the velocities (u and v) are defined at the centers of the faces.

to perform direct numerical simulation of turbulent flow at reduced computational effort. An important, and probably independent, contribution to second-order skew-symmetric discretization of the convective terms in the Navier-Stokes equations is in the work of [66]. Here we follow the formulation chosen in [100]. These discretization methods are examples of a more general philosophy of developing discretization schemes which 'respect' basic properties of the underlying system of equations, known as mimetic discretization [83]. Likewise, the viscous flux contributes only to dissipation of energy, which has to be strictly maintained in a numerical method. We motivate this in some more detail next.

Starting from the original momentum equation without the forcing term

$$\frac{\partial \mathbf{u}}{\partial t} = -(\mathbf{u}\cdot\nabla)\mathbf{u} - \nabla P + \frac{1}{Re}\nabla\cdot\nabla\mathbf{u} \tag{2.6}$$

we are interested in the kinetic energy, given by

$$E = \frac{1}{2}\int_{\Omega} dV|\mathbf{u}|^2 = \frac{1}{2}\int_{\Omega} dV\mathbf{u}\cdot\mathbf{u} = \frac{1}{2}(\mathbf{u},\mathbf{u}) \tag{2.7}$$

where $\mathbf{u}\cdot\mathbf{u}$ is the vector inner product and $(\mathbf{u},\mathbf{u})$ is the corresponding 'function inner product' in terms of the velocity field $\mathbf{u}$. Note, that in (2.7) we effectively integrate only over Ω_f as $\mathbf{u} = \mathbf{0}$ in Ω_s. The evolution of the kinetic energy follows from

$$\frac{dE}{dt} = \int_{\Omega} dV\mathbf{u}\cdot\frac{\partial \mathbf{u}}{\partial t} \tag{2.8}$$

In order to obtain the integrand in (2.8) we multiply the Navier-Stokes equation (2.6) by $\mathbf{u}$. Integrating by parts we can derive the contribution of each of the fluxes in (2.6). In fact, the convective and pressure terms do not contribute to the evolution of energy, and we find

$$\frac{dE}{dt} = -\frac{1}{Re}\int_{\Omega} dV(\nabla\mathbf{u} : \nabla\mathbf{u}) \leq 0 \tag{2.9}$$

where $\nabla\mathbf{u} : \nabla\mathbf{u} = \partial_i u_j \partial_i u_j$ in which we sum over repeated indices. This suggests that the energy of any solution decreases in time because of viscous fluxes only.

A more elaborate derivation can be found in [100], which departs from the expressions

$$E = \frac{1}{2}(\mathbf{u},\mathbf{u}) \quad \text{and} \quad \frac{dE}{dt} = \frac{1}{2}\frac{d}{dt}(\mathbf{u},\mathbf{u}) \tag{2.10}$$

where energy is written in terms of the function inner product $(\mathbf{u},\mathbf{u})$ as defined in (2.7). This yields the symmetric expression

$$\begin{aligned}\frac{dE}{dt} = &-\frac{1}{2}\Big(((\mathbf{u}\cdot\nabla)\mathbf{u},\mathbf{u}) + (\mathbf{u},(\mathbf{u}\cdot\nabla)\mathbf{u})\Big) - \frac{1}{2}\Big((\nabla P,\mathbf{u}) + (\mathbf{u},\nabla P)\Big) \\ &+ \frac{1}{2Re}\Big((\nabla\cdot\nabla\mathbf{u},\mathbf{u}) + (\mathbf{u},\nabla\cdot\nabla\mathbf{u})\Big)\end{aligned} \tag{2.11}$$

Since $(\nabla P,\mathbf{u}) = -(P,\nabla\cdot\mathbf{u})$ and the skew-symmetry $((\mathbf{u}\cdot\nabla)\mathbf{v},\mathbf{w}) = -(\mathbf{v},(\mathbf{u}\cdot\nabla)\mathbf{w})$ holds we obtain again (2.9), i.e., no contribution from pressure and the convective flux. This is the basis for the discretization.

In a discrete setting the Navier-Stokes equations in matrix-vector notation are written as

$$\boldsymbol{\Lambda}\frac{d\mathbf{u}_h}{dt} = -\mathbf{C}\mathbf{u}_h - \mathbf{D}\mathbf{u}_h + \mathbf{M}^T\mathbf{P}_h \tag{2.12}$$

$$\mathbf{M}\mathbf{u}_h = \mathbf{0} \tag{2.13}$$

where $\mathbf{u}_h$ is the vector containing the discrete velocity solutions $u_i^{(h)}$, $\mathbf{P}_h$ is the discrete pressure, $\boldsymbol{\Lambda}$ is a matrix with the volumes of the grid cells on its diagonal, $\mathbf{C}$ and $\mathbf{D}$ are the coefficient matrices corresponding to the discretization of the convective $((\mathbf{u}\cdot\nabla)\mathbf{u})$ and diffusive $(-\Delta\mathbf{u}/Re)$ operators, respectively. The discretization of the pressure gradient is given by $-\mathbf{M}^T$, while the coefficient matrix $\mathbf{M}$ itself represents the discretization of the divergence operator, integrated over the control volumes [100].

The discrete approximation for the kinetic energy can be given using the midpoint rule, as

$$E_h = \mathbf{u}_h^T\boldsymbol{\Lambda}\mathbf{u}_h \tag{2.14}$$

Similar to the continuous case (2.11) we compute the evolution of the energy in the discrete model as

$$\frac{dE_h}{dt} = -\mathbf{u}_h^T(\mathbf{C}+\mathbf{C}^T)\mathbf{u}_h - \mathbf{u}_h^T(\mathbf{D}+\mathbf{D}^T)\mathbf{u}_h + \mathbf{u}_h^T(\mathbf{M}^T\mathbf{P}_h) + (\mathbf{M}^T\mathbf{P}_h)^T\mathbf{u}_h \tag{2.15}$$

For a discrete solution we also require the convective conservation of energy, which implies skew-symmetry of the matrix $\mathbf{C}$ of the convective operator: $\mathbf{C}+\mathbf{C}^T=\mathbf{0}$. The two terms related to the numerical pressure gradient can be rewritten as

$$\mathbf{u}_h^T(\mathbf{M}^T\mathbf{P}_h)+(\mathbf{M}^T\mathbf{P}_h)^T\mathbf{u}_h=(\mathbf{M}\mathbf{u}_h)^T\mathbf{P}_h+\mathbf{P}_h\mathbf{M}\mathbf{u}_h=\mathbf{0} \tag{2.16}$$

where the numerical divergence operator $\mathbf{M}$ satisfies equation (2.13). Thus, pressure terms also cancel and do not influence the stability of the spatial discretization. By comparison with the expression for the energy evolution (2.9), the second term in the right-hand side of (2.15) should provide a strict decrease of the energy:

$$\frac{dE_h}{dt}=-\mathbf{u}_h^T(\mathbf{D}+\mathbf{D}^T)\mathbf{u}_h\leq 0 \tag{2.17}$$

This implies that the coefficient matrix $\mathbf{D}$ of the diffusion operator is a positive-definite matrix. Thus, discretely we obtain the same properties for the energy decay as in the continuous case.

In this chapter we closely follow the symmetry preserving finite volume discretization as put forward by [100]. We use central differencing of second order accuracy, which maintains explicitly the skew-symmetry in the discrete equations. Since the energy is preserved under the convective operator the skew symmetric discretization allows to obtain a stable solution on any grid. For proper capturing of the solenoidal property (2.5) of the velocity field we approximate the gradient operator by the transpose of the numerical divergence operator. The contributions of the convective, viscous and pressure-gradient fluxes are integrated in time using a generalization of the explicit second order accurate Adams-Bashforth method. Care is taken of accurately representing the skew-symmetry also in the time-integration. Full incorporation would require an implicit time-stepping, which, however, is computationally too demanding. Instead, time-integration starts from a modification of the leapfrog method with linear inter/extrapolations of the required 'off-step' velocities and an implicit treatment of the incompressibility constraint. Optimization for largest stability region of the resulting scheme yields a particular so-called 'one-leg' time-integration method, with a mathematical structure that is akin to the well-known Adams-Bashforth scheme. More details can be found in [100].

A special role is played by the forcing term in the Navier-Stokes equations (2.4), which represents the volume penalization accounting for solid objects inside and at the boundaries of the flow domain. The role of the forcing term is to yield an accurate approximation of the no-slip condition at solid boundaries. In conventional computational fluid dynamics such a forcing term is not needed since the flow domain is endowed with a body-fitted grid on which the equations are discretized. The grid-lines in such cases are defined such that they either closely follow the contours of the solid boundaries, or they are (preferably) at right angles with them. In such a discrete formulation the no-slip boundary condition can be imposed eas-

ily. The body-fitted grid is efficient if the fluid domain Ω_f is not too complex and does not contain too many separate objects around which the fluid should flow [46]. For considerably more complex flow domains or in case the location of the solid-fluid interface is not perfectly known, as in case of medical imagery, the body-fitted grid approach is limited by the generation of suitable meshes. These should not only align with the solid boundaries, but also be sufficiently smooth near these boundaries to allow an accurate solution in the boundary layers [53]. In our discrete model the forcing term contributes strongly to the stiffness of the equations. When an explicit time-stepping method would be adopted for the forcing term, as is done for the other dynamic contributions, this would result in extremely small time-steps in view of numerical stability. Therefore, the linear forcing term is integrated in time using the implicit Euler scheme [54].

2.2.3 Masking function strategy

In this subsection, we first consider three options for creating a general masking function and illustrate these for a circle on a 2D Cartesian grid. We also present the procedure with which the specification of the masking function of any curved cylindrical 3D-tube was taken up. The validation and comparison of the masking strategies will be presented in Section 2.3.

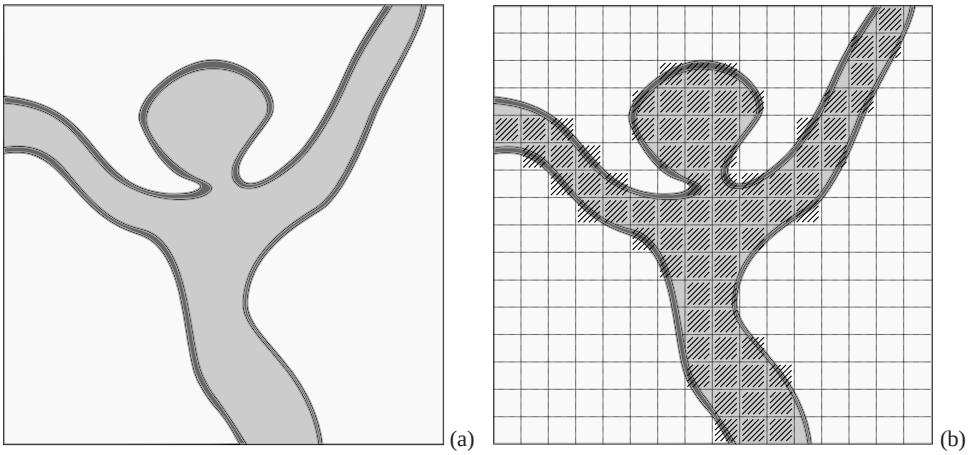

Fig. 2.2 Sketch of complex flow domain (a) (grey area). On a Cartesian grid the definition of the masking function can be based, e.g., on the ‘material’ (‘solid’ or ‘fluid’) found at the cell center (b).

The masking function technique is a simple and fast way to indicate the location of an object. Illustration of the masking function for a flow domain is given in Figure 2.2. A simple approach to distinguish which grid cells are inside the solid domain and which are outside is

the following: if the center of the grid cell is of type ‘solid’ or ‘fluid’, then that entire grid cell is taken to be of that type. Figure 2.2(b) illustrates how, based on this rule, some cells become internal (hatched) and others are outside the fluid part of the domain.

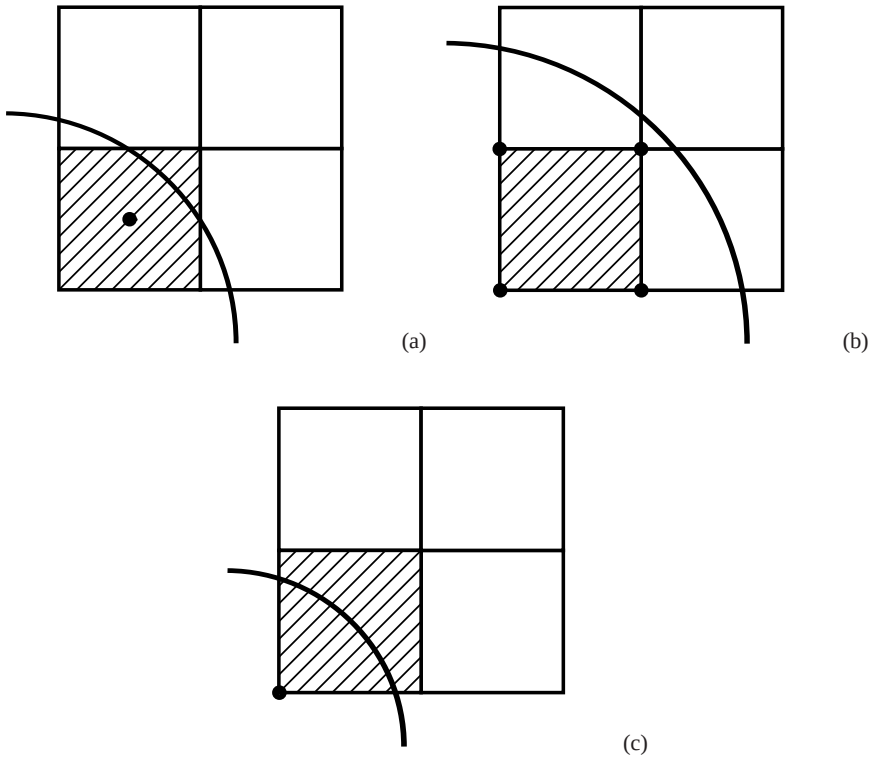

Fig. 2.3 Strategies to define a masking function for a grid cell on a Cartesian grid. For convenience we illustrate here 2D grid cells. We propose three ways to define fluid cells (hatched) and thus the fluid domain. The ‘basic’ strategy (a) is the one where the property at the center of the cell defines that of the whole cell. The two other strategies differ in the number of corner points that are inside the fluid domain. Thus we obtain the so-called ‘inner’ strategy (b) when the cell is denoted to be ‘fluid’ if all its corners are inside the fluid domain and the ‘outer’ strategy (c) when we call the cell ‘fluid’ if at least one of its corners belongs to the fluid domain.

In three-dimensional domains we formulate the problem in a rectangular block of size $L_x \times L_y \times L_z$ that is large enough to contain the flow domain of interest. A uniform Cartesian grid with mesh-spacings $h_{x,y,z} = L_{x,y,z}/N_{x,y,z}$ for the three coordinate directions is defined, using $N_{x,y,z}$ grid cells in each direction. In our basic method, if the center of a cell is solid (fluid) then we take the whole cell to be solid (fluid) and $H = 1$ ($H = 0$) (Figure 2.3(a)). Next to this basic method we can introduce two closely related methods based on the corner-nodes

of a grid cell. We consider 3D cells and first determine the solid or fluid property for every corner point of the cell. Then, in one strategy we denote a grid cell as fluid if all eight of its nodes are fluid. This is illustrated for 2D cells in Figure 2.3(b) (fluid cell is hatched). Another strategy assigns for the whole cell the value 'fluid' if at least one of its corners is in the fluid part of the domain (Figure 2.3(c)). In the sequel, we will refer to these three strategies as 'basic', 'inner' and 'outer' respectively. The 'inner' strategy has the tendency to produce flow domains that are slightly smaller than the 'basic' approach while the 'outer' strategy is likely to yield slightly larger flow domains. In the next section we will validate these three masking function strategies for Poiseuille flow in a straight cylindrical pipe, showing the sensitivity of predictions to details of the geometry definition. The possible application of the 'inner' and 'outer' masking strategies was presented in [61], where 'inner' and 'outer' solutions were considered as numerically bounding the 'basic' solution and some of its important flow characteristics.

The masking strategies define the masking function in the middle of the grid cell, i.e., in H_p points of a staggered grid. Given H_p, we can extract H_u, H_v and H_w for the staggered grid. We assign the value of the masking function at a cell face as the maximum of the H_p values of the neighboring grid cells. In Figure 2.4 we illustrate for 2D grid cells the mechanism of extracting staggered masking values at the grid faces. Thus, $H_u(i,j) = \max(H_p(i,j), H_p(i+1,j))$ and $H_v(i,j-1) = \max(H_p(i,j), H_p(i,j-1))$.

To obtain a masking function according to one of the above strategies for a smoothly curved cylindrical tube we use the smallest distance approach to specify for every point in the computational domain its 'type', i.e., solid or fluid. In fact, we determine the minimum distance to the centerline of the curved vessel and then check the condition whether this distance is smaller or greater than the radius of the desired cylindrical tube. We apply the smallest distance approach to the centers of the cells in the 'basic' strategy and to all eight nodes of the 3D cell in the 'inner' and 'outer' strategies.

We consider the centerline of the tube in parametric form, as $(x(s), y(s), z(s))$ where $0 \leq s \leq 1$. For every point (X, Y, Z) in the computational domain we may determine whether or not the minimal distance to the centerline is smaller than the radius of the desired cylindrical tube. If so, then the point is in the fluid domain, otherwise it is in the solid domain. Specifically, we consider the distance vector

$$\mathbf{d} = \Big(X - x(s), Y - y(s), Z - z(s)\Big) \tag{2.18}$$

and obtain the square of the Euclidean distance as the inner product

$$D \equiv \mathbf{d} \cdot \mathbf{d} = |\mathbf{d}|^2 \tag{2.19}$$

For every (X, Y, Z), D is a function of the parameter s only. We require the global minimum of the function D, which implies at least the first order condition

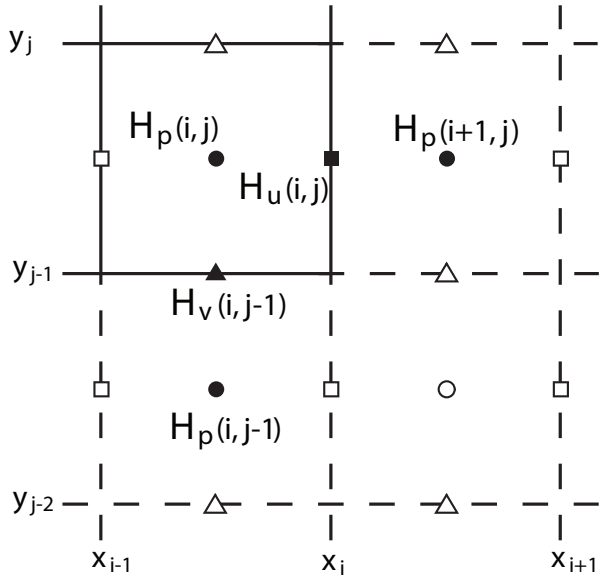

Fig. 2.4 The process of defining masking function in the staggered locations (squares, triangles), based on the values in the middle of the cell (circles). We choose the maximum value of two H_p values of neighboring cells sharing a common face and assign this value to the staggered masking function H_u or H_v. This reflects the choice that if a solid and a fluid cell come together in a face then the face is solid as well.

$$D' = 2\mathbf{d} \cdot \mathbf{d}' = 0 \tag{2.20}$$

where the prime indicates differentiation with respect to s. This optimality condition specifies that in the optima the distance vector $\mathbf{d}$ is perpendicular to the tangential vector $\mathbf{d}'$ at the centerline, which has an obvious geometric interpretation. The equation for an extremum is

$$\Big(X - x(s)\Big)x'(s) + \Big(Y - y(s)\Big)y'(s) + \Big(Z - z(s)\Big)z'(s) = 0 \tag{2.21}$$

which can be solved numerically to obtain local (and global) extrema for $0 \leq s \leq 1$. In the sequel we consider planar curves as centerline. In that case $y' = 0$ and $x(s) = L_x s$ so that

$$-L_x^2 s + \Big(Z - z(s)\Big)z'(s) = -XL_x \tag{2.22}$$

As a particular case we take $y(s) = L_y/2$ and choose the centerline to be sinusoidal

$$z(s) = L_z/2 + C\sin(2\pi(s - 1/4)) \tag{2.23}$$

where C is called the 'curve-parameter', for simplicity.

In order to specify the 'type', i.e., solid or fluid, of a given point (X,Y,Z) we need first to determine the parameter-value s at which the global minimum of (2.21) is attained. Numerically, this can be implemented in two stages: first, we coarsely sample the square distance function (2.19) in 2^k steps to obtain a 'candidate' interval and second, we refine this interval to obtain the global minimum using simple bisection. After some experimentation we found that coarse sampling at $k = 6$ is suitable for mildly curved vessels. Once the optimal s^* is determined for a given (X,Y,Z), we can compute the smallest distance d at s^*. If this smallest distance $d \leq R$ then (X,Y,Z) is of type 'fluid', and it is of type 'solid' otherwise.

In this chapter we consider two basic geometries motivated by medical application: curved vessels and model aneurysms. Three dimensional shapes are illustrated in Figure 2.5. The curved vessel is a cylindrical tube, with a sinusoidal centerline (Figure 2.5(a)) with curve-parameter $C = 2$ in (2.23). The model aneurysm (Figure 2.5(b)) is the 'extension' of this curved vessel by merging it with a sphere, with radius $R_{sphere} = 3R_{vessel}$ (Figure 2.5(b)).

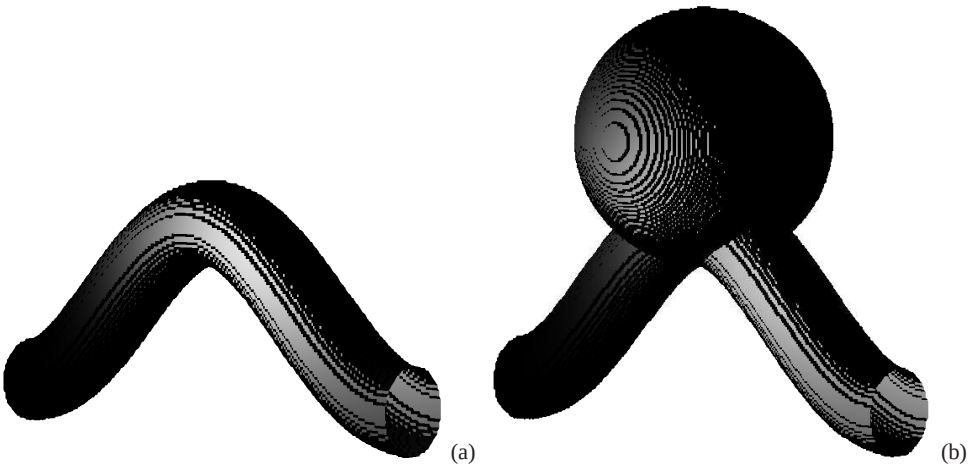

Fig. 2.5 Basic geometries in 3D. The curved vessel (a) is a cylindrical tube with a sinusoidal centerline, while the model aneurysm is composed of a curved vessel and a sphere attached to it (b).

2.3 Validation of the IB method

In this section we analyze the capabilities of the IB method in capturing steady flow in non-aligned geometries and show the results of computations for a number of basic geometrical shapes such as a straight cylindrical vessel and smoothly curved cylindrical vessels. In the first subsection we focus on Poiseuille flow in a straight vessel and provide an assessment of the accuracy of the IB method. In this illustration and in all other flows the initial condition

is taken as $(u,v,w) = (1,0,0)$, presenting a strict test for the IB method as the velocity in the solid has to adapt fully to the no-slip condition. The total IB method is shown to have first order convergence. Subsequently, we propose a qualitative view of the flow inside curved vessels, showing the flexibility of the IB approach in predicting flow in more complex flow domains, and quantify the level of convergence by monitoring the pressure drop over the vessel at a range of resolutions.

2.3.1 Flow in straight vessels

A fully developed, incompressible, laminar flow through a straight circular tube of constant cross section is known as Poiseuille flow [4]. The exact analytical solution for this type of flow can be written as $(u,v,w) = (u,0,0)$, where $u(r) = 1-r^2$ in terms of the radial coordinate r. This corresponds to a volumetric flow rate $Q = \pi/2$.

The IB method is validated by comparing the numerical results with the analytical solution for cylindrical pipe flow. We consider flow at $Re = 250$ and assume that the x-domain is from $-L/2$ to $L/2$ with center of the tube at $x = 0$, and likewise for the y and z-domain ranging from $-3R/2$ to $3R/2$ with center at $y = 0$ and $z = 0$. Since we adopt a non-dimensional formulation, the validation of the numerical method with reference to laminar Poiseuille flow can be executed at any value of Re as long as the parabolic velocity profile is stable. Identical results can be obtained when validation is done at lower Reynolds numbers. To test the application of the method at physiologically relevant conditions, we set $Re = 250$; at this flow condition a longer simulation time is required compared to, e.g., $Re = 1$, to reach the final steady state that we want to test against the analytical solution. This provides as additional result a test of the time-stepping method under realistic conditions.

Numerically, we define the flow to have reached the steady state once the pressure drop over the computational domain needed to maintain the desired flow rate has converged to within 10^{-11} at $Re = 1$ and within 10^{-5} at $Re = 250$. This steady state was reached already at $t \approx 2.5$ for the lower Reynolds number while at $Re = 250$ the indicated steady state is obtained only after $t \approx 5$. During the simulations we verified that the flow is independent of the axial coordinate, as required by the analytical solution.

We investigate numerical velocity profiles for a number of grid resolutions. We use $4 \times N \times N$ grid cells in the x, y and z directions respectively, where $N = 8,16,...,256$. As was already mentioned in Subsection 2.2.3 we may create masking functions in three different ways. In order to investigate the accuracy and robustness of the IB method we validate each of these masking strategies. Figure 2.6 illustrates velocity profiles for all three masking strategies. The solid line denotes the analytical solution, all dashed lines are approaching this solution from above or below, depending on whether the numerical representation of the circular cross section is slightly smaller or slightly larger than the actual cross-section,

respectively. Combination of the 'inner' and 'outer' masking strategies provides a practical manner to arrive at lower and upper bounding solutions between which the analytical solution is contained. This was exploited and presented in [61]. The visual convergence check will next be quantified and the order of accuracy of the IB method inferred.

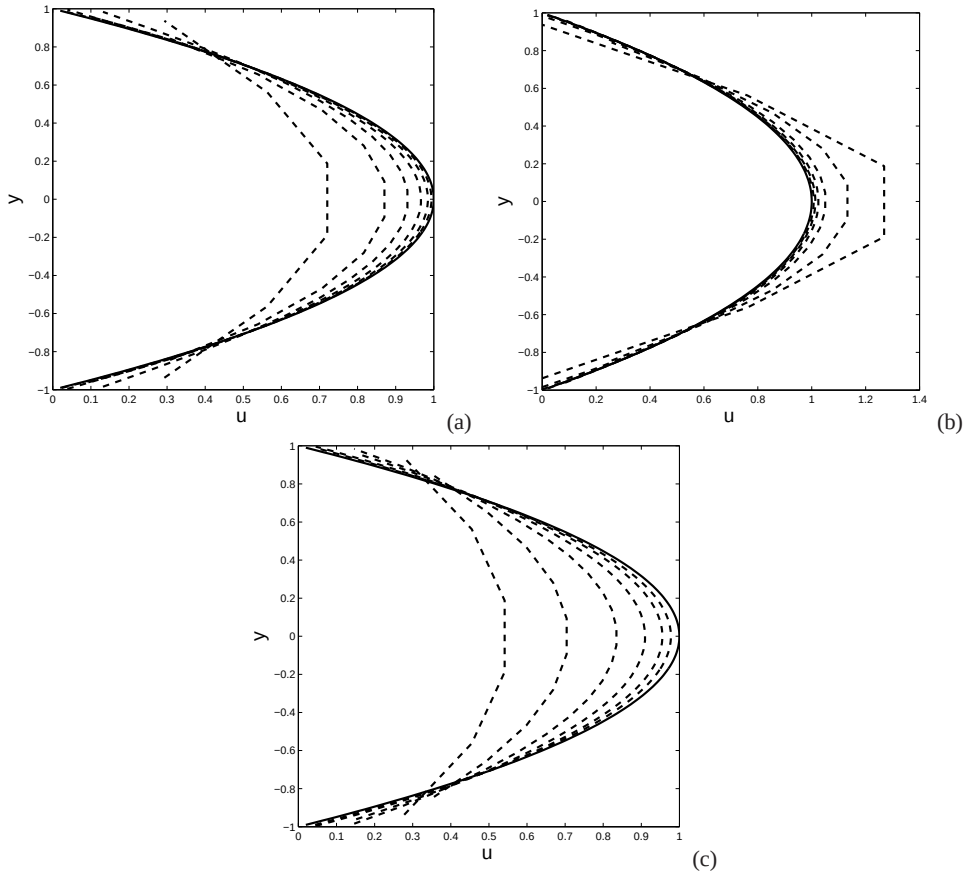

Fig. 2.6 Velocity profiles for three different masking function strategies ('basic' (a), 'inner' (b) and 'outer' (c)). The total flow domain ranges from $-3/2 \leq y \leq 3/2$, $-3/2 \leq z \leq 3/2$, of which the profile at $z = 0$ and $|y| \leq 1$ is shown. Profiles are obtained at grid resolutions $4 \times N \times N$ in (x,y,z) with $N = 8, 16, \ldots, 256$. Solutions at increasing resolutions are identified by the sequence of dashed lines which converge to the solid line representing the analytical solution for Poiseuille flow.

There are several ways to define the difference between analytical and numerical solutions. For estimating the convergence of the velocities we compare numerical results with the analytical solution directly in the grid points and compute the discrete L_2-norm along a line at $z = 0$ and $x = 0$, i.e., along a vertical line in the middle of the domain. The difference between the analytical and a numerical solution appears as

$$\delta_u = \sqrt{\frac{1}{N_y}\sum_j (u_{N_x/2,j,N_z/2} - U_{ex,j})^2}, \tag{2.24}$$

where $u_{N_x/2,j,N_z/2} = u(N_x/2, j, N_z/2)$ and $U_{ex,j} = (1-y_j)^2$ for grid points $|y_j| \leq 1$. We also analyze the convergence of the pressure differences over the computational domain, by computing the absolute value of the difference between the numerical and the analytical pressure differences. The reduction of the error for velocity and pressure difference is presented in Figure 2.7 for all the masking strategies. Solid lines show slopes at -1 and -2 as reference. The marked lines are for the three masking strategies. As we can observe, for all masking strategies the numerical method converges to first order. This basically reflects the non-alignment of the cylinder wall with the Cartesian grid, leading to inaccuracies in the solid-fluid interface definition. It appears in this case that the 'inner' masking strategy is most accurately representing Poiseuille flow closely followed by the 'basic' strategy. For further computations we will use the 'basic' masking function based on the pressure-points (Figure 2.3(a)), as this is most straightforward.

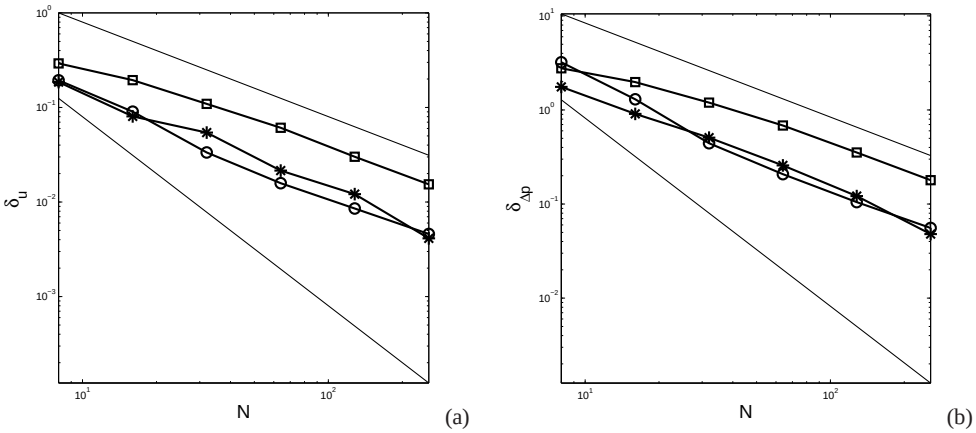

Fig. 2.7 Convergence of the numerical solution for streamwise velocity (a) and pressure difference (b) for Poiseuille flow. The difference for the velocities is measured in terms of the discrete L_2-norm δ_u, while for the pressure difference we consider the absolute difference between analytical and numerical solutions. Solid lines without markers denote slopes -1 and -2 respectively. The line marked with circles ($\circ$) corresponds to the 'inner' strategy, the line with stars ($*$) is for the 'basic' strategy, the line with squares ($\square$) is for the 'outer' strategy for generating the masking function.

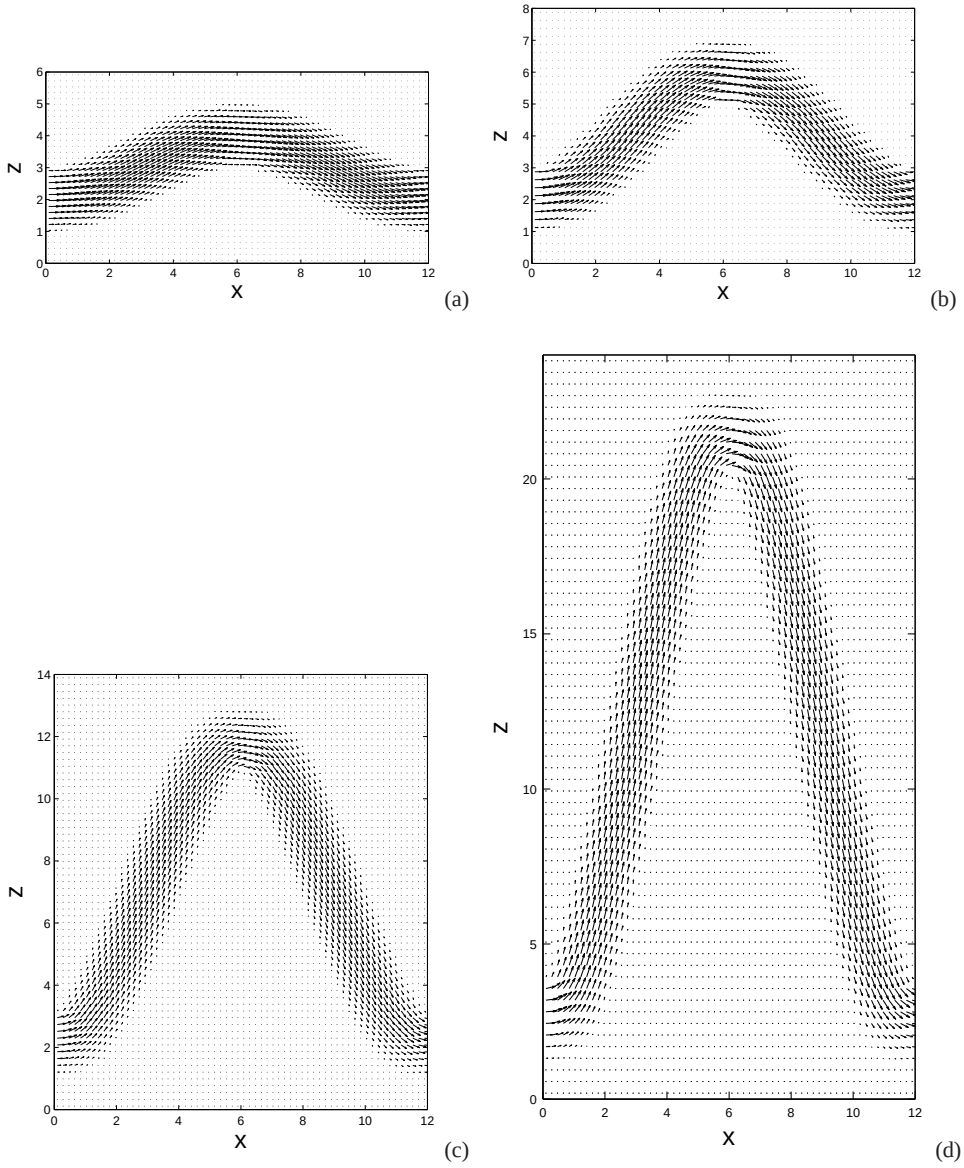

Fig. 2.8 Velocity vector fields at $Re = 1$ in middle cross-sections of sinusoidally curved cylindrical vessels at increasing values of the curve-parameter in (2.23): $C = 1$ (a), $C = 2$ (b), $C = 5$ (c) and $C = 10$ (d). Simulations employed a resolution of $64 \times 16 \times 32$ for (a),(b) and $64 \times 32 \times 64$ for (c),(d).

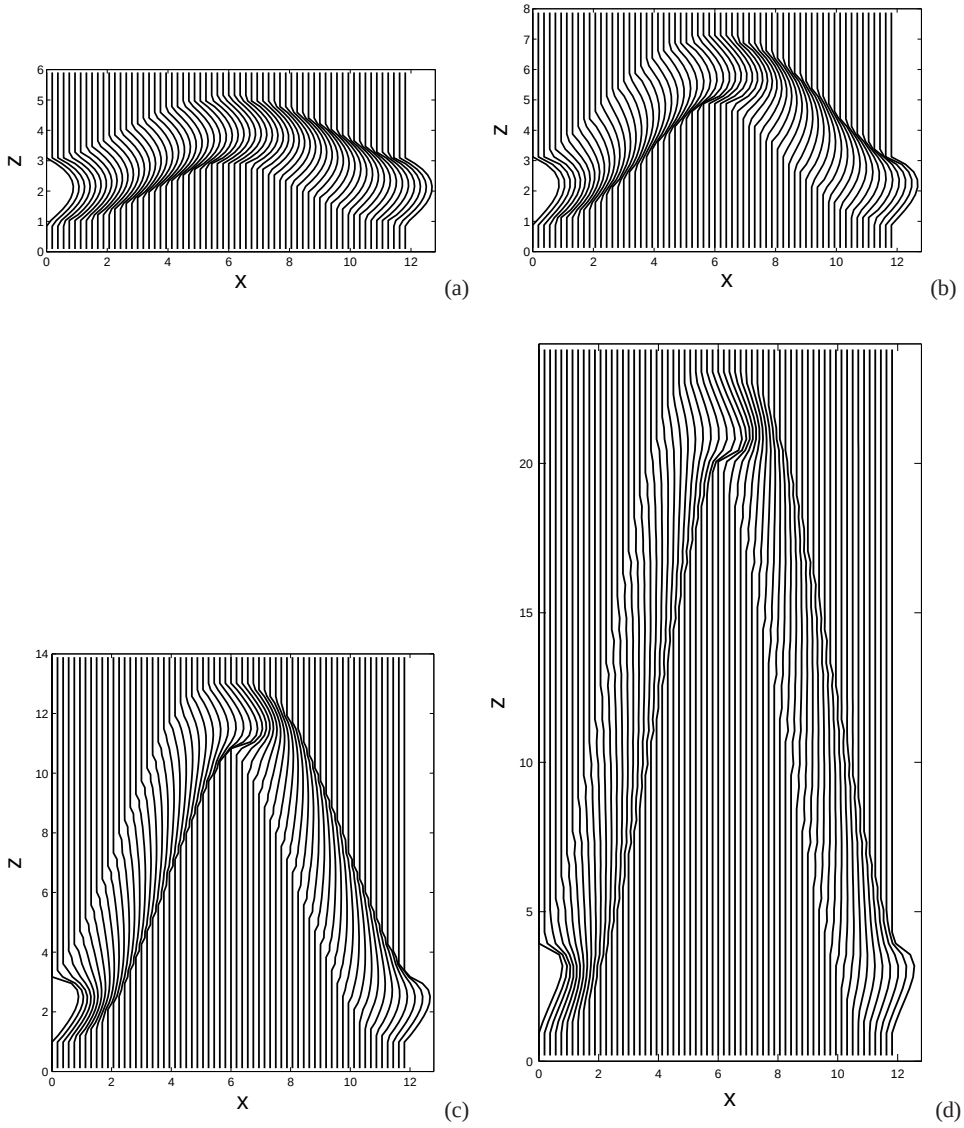

Fig. 2.9 Profiles of the streamwise velocity component u at $Re = 1$. Parameters as in Figure 2.8.

2.3.2 Flow in curved vessels

In the previous subsection we assessed the numerical method for a basic case of flow in a straight cylindrical tube. The validation shows first order convergence for laminar Poiseuille flow. In this subsection we show the flexibility of the IB method to capture flow in curved vessels even at fairly modest resolutions. The steady velocity field that develops at $Re = 1$

is shown in Figure 2.8 for curved vessels with curve-parameters $C = 1$, $C = 2$, $C = 5$ and $C = 10$ in (2.23). Simulations show that the laminar flow closely follows the shape of the vessel. Near the vessel wall we recognize the coarseness of the 'staircase' representation. This effect is seen to be only very local and can be reduced by increasing the resolution.

The velocity profiles along the curved tubes depend on the actual shape of the vessel. The profiles follow the contours of the vessel and at certain locations along the centerline the local profiles differ considerably from the simple Poiseuille profile that was considered earlier. This is shown in Figure 2.9. Already at relatively coarse grids the numerical solution appears to capture the flow quite reliably.

The convergence of the IB method for curved vessels and model aneurysms can be further quantified. We consider the pressure difference over the flow domain in the x-direction that is required to maintain the imposed volumetric flow rate. In Figure 2.10 we display the development of this pressure difference for two flows, i.e., at $Re = 1$ (Figure 2.10(a)) and $Re = 100$ (Figure 2.10(b)) for a curved vessel at curve-parameter $C = 2$. We observe a clear convergence in the pressure evolution by comparing results obtained upon doubling the resolution several times. At $Re = 1$ and $Re = 100$ we quite closely recover first order convergence. In fact, we consider the convergence ratio $q = ((\Delta p)_{2N} - (\Delta p)_N)/((\Delta p)_{4N} - (\Delta p)_{2N})$ for the three finest grids with number of grid points N, $2N$ and $4N$. At $Re = 1$ we find at $t = 0.1$; $q = 2.2$ and at $Re = 100$ and $t = 5$; $q = 1.8$. Both are quite close to the value of 2 that would imply first order convergence. The flow at both Reynolds numbers approaches a steady state.

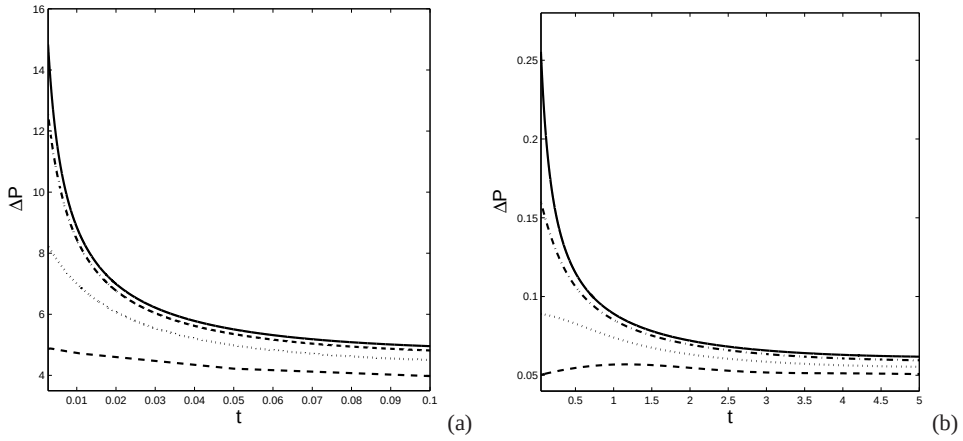

Fig. 2.10 Convergence of the IB method for flow inside a curved cylindrical vessel, at curve-parameter $C = 2$ in terms of the evolution of the pressure difference over the streamwise extent as a function of time. Simulations are done at $Re = 1$ (a), $Re = 100$ (b) at several grid resolutions: $32 \times 8 \times 16$ (dash), $64 \times 16 \times 32$ (dot), $128 \times 32 \times 64$ (dash-dot) and $256 \times 64 \times 128$ (solid). With increasing resolution the numerically obtained solution is seen to converge to a grid independent result.

2.3.3 Flow in a model aneurysm

In this subsection we present the velocity vector field and pressure differences for the flow inside the model aneurysm. The simulations are performed at Reynolds numbers $Re = 100$ and $Re = 250$. The velocity field distributions inside the model aneurysm are presented in Figure 2.11. Previously, we showed the flow in a curved vessel, which is laminar and steady at both Reynolds numbers. The addition of an aneurysm cavity renders the flow slightly unsteady for an extended period at $Re = 100$. Some vortical flow structures are seen inside the aneurysm. We observe quite similar flow patterns albeit with more pronounced vortices inside the flow field at $Re = 250$.

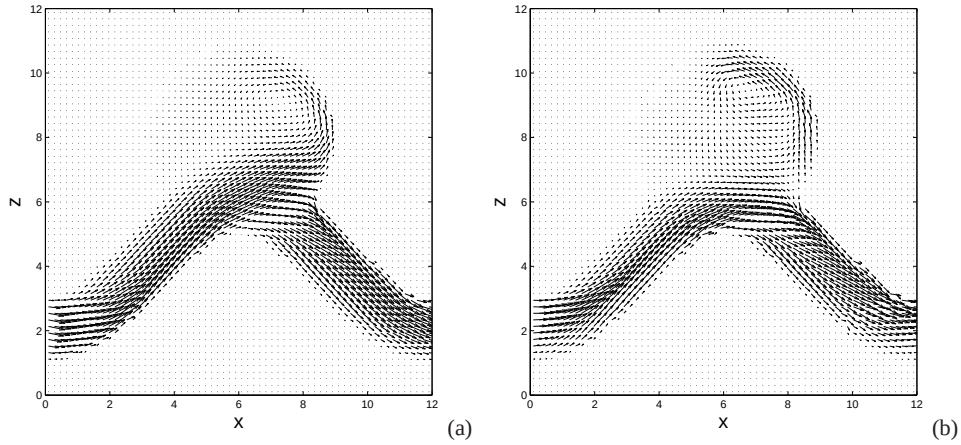

Fig. 2.11 Snapshot of the developing flow inside a model aneurysm at $Re = 100$ (a) and $Re = 250$ (b). The flow is visualized in a cross section through the geometry, by plotting the in-plane velocity vectors at a characteristic time. Results are shown for grid resolution $64 \times 32 \times 64$.

In Figure 2.12 we consider the pressure drop required to maintain the flows at $Re = 100$ (Figure 2.12(a)) and $Re = 250$ (Figure 2.12(b)) through the model aneurysm. At $Re = 250$ the result appears to indicate first signs of sustained unsteadiness while the solutions at $Re = 100$ becomes steady after a long time. For this case only three refinements were included in view of computational time. With increasing grid resolution the computed flow converges for both flows, roughly expressing the first order convergence shown previously for Poiseuille flow. The convergence rate q was also computed for both Reynolds numbers and it takes values $q = 1.86$ at $Re = 100$ and $q = 3.05$ at $Re = 250$ at $t = 50$.

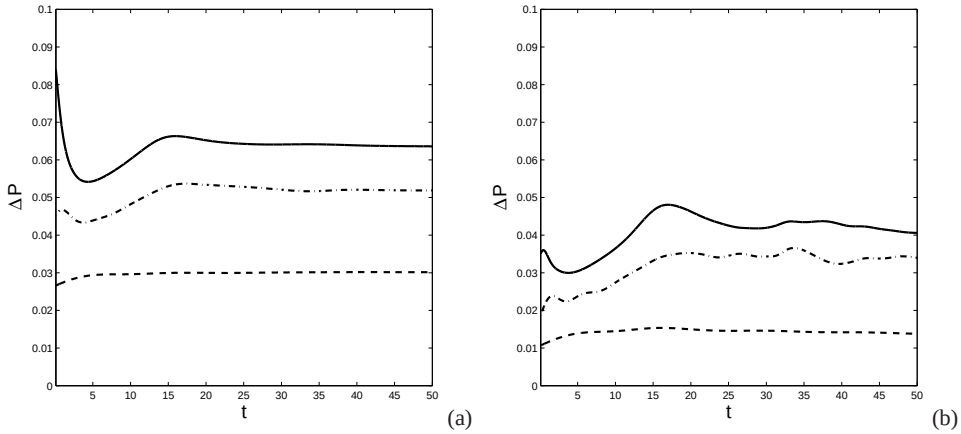

Fig. 2.12 Convergence of the IB method for flow inside a model aneurysm in terms of the evolution of the pressure difference over the streamwise extent as a function of time. Simulations are done at $Re = 100$ (a) and $Re = 250$ (b) at several grid resolutions: $16 \times 8 \times 16$ (dash), $32 \times 16 \times 32$ (dash-dot) and $64 \times 32 \times 64$ (solid).

2.4 Shear stress in curved vessel and model aneurysm

In this section we focus on the shear stress which develops inside the flow domain and at the vessel walls as a result of the blood flow inside. We first illustrate the IB approach for the shear stress associated with Poiseuille flow in a straight cylindrical pipe. This extends the validation study shown in the previous section by establishing the accuracy with which also the gradient of the velocity can be obtained numerically. Subsequently, we apply our method to compute shear stress in a curved 'sinusoidal' vessel and in the model aneurysm.

2.4.1 Validation of the IB computed shear stress

The main challenge for any IB method is to capture the flow near solid-fluid interfaces. In this region the highest velocity gradients may occur, leading to correspondingly highest levels of numerical error. During the initiating stages of an aneurysm, local high pressure and shear stresses may contribute to the growth, while in developed stages low shear stress levels may contribute to degenerative changes [84, 9]. This makes the shear a quantity of relevance for understanding the often slow growth of an aneurysm [13], as well as a key component in mechanisms involved in sometimes much more rapid aneurysm development [21].

We define the shear stress in terms of the gradient of the velocity as follows. The rate-of-strain tensor S is given by

$$S = \frac{1}{2}(\nabla \mathbf{u} + \nabla \mathbf{u}^T) \tag{2.25}$$

The shear stress τ is a measure for the gradient of the velocity and we formulate it in terms of the components of S as follows:

$$\tau \equiv \frac{1}{Re}\sqrt{2S:S} \tag{2.26}$$

The normal stresses are contained on the diagonal elements of the tensor S and the tangential (shear) stresses are defined by the off-diagonal elements of S [75]. As point of reference for our numerical approach, we compute analytically the shear stress that results from (2.26) for the classical cases of a channel flow and a pipe flow. We obtain from (2.26)

$$\tau = \frac{1}{Re}\left|\frac{\partial u}{\partial y}\right| \tag{2.27}$$

for channel flow (in Cartesian coordinates) and for pipe flow in cylindrical coordinates [106].

In Section 2.3 we discussed laminar Poiseuille flow showing parabolic velocity profiles. Here, we extend the validation to shear stress, and expect linear profiles for τ. Within the velocity field $(u,v,w) = (1-r^2,0,0)$ we find $S:S = 2r^2$ and hence obtain

$$\tau = \frac{2}{Re}|r| \tag{2.28}$$

We validate the shear stresses for steady flow at $Re = 250$ and compare numerical solutions for the three masking strategies with the analytical result in (2.28).

Profiles of the shear stress distribution inside the cylindrical tube are collected in Figure 2.13. The solid line is the analytical result for the cylindrical tube. With increasing grid resolution the numerical solution is seen to converge to the analytical shear stress. To assess the order of convergence we computed the difference in L_2 norm (see Figure 2.14). We observe that the convergence of the shear stress is similar to that of the velocity predictions. For the 'outer' strategy the convergence appears somewhat slower than for the 'inner' and 'basic' methods. The resolution beyond which first order convergence is quite established appears to be higher than was required for the velocity predictions (Figure 2.7(a)).

The first order convergence of the shear stress, i.e., the derivative of the velocity, on the basis of a numerical solution for the velocity that itself converges to first order may appear somewhat surprising. However, an argument why such first-order convergence for the derivative should arise can briefly be sketched as follows. We use a 1D setting for convenience and denote the approximation of the exact solution U in the point x_j by u_j. Assuming first-order convergence implies

$$u_j = U(x_j) + a_j h + \ldots \tag{2.29}$$

where a_j denotes the coefficient for the first order error term and h denotes the grid spacing. Using a simple discretization δ_x for the first derivative, this implies

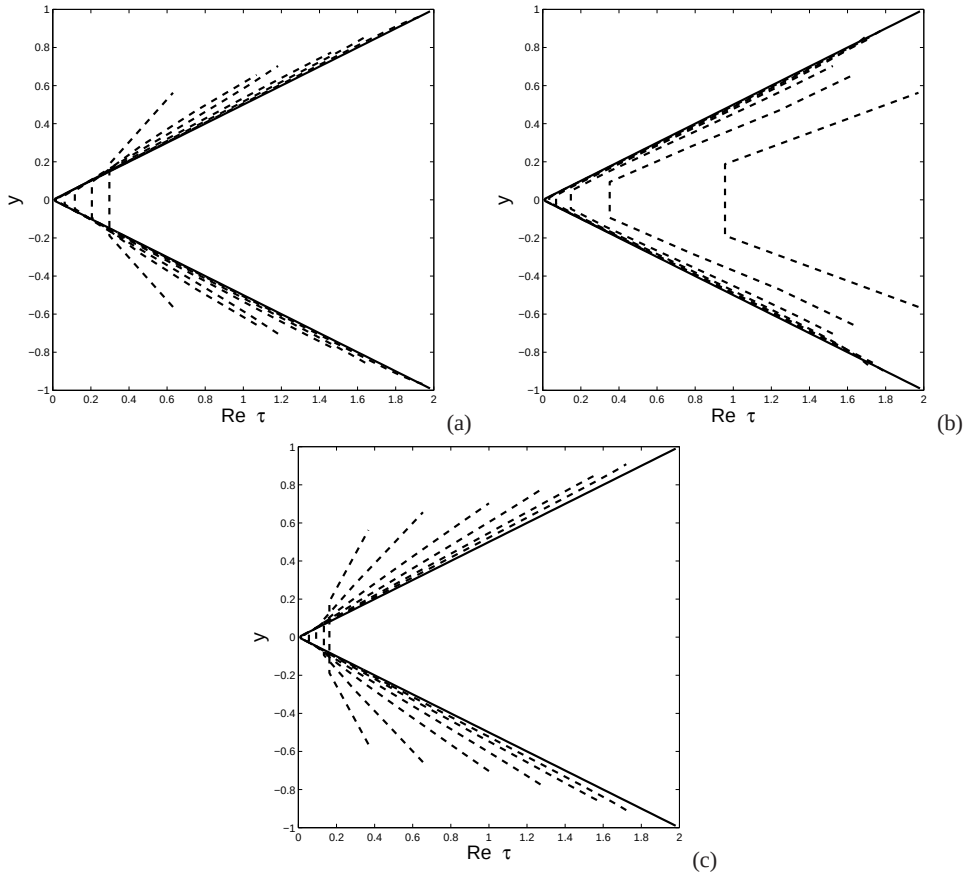

Fig. 2.13 Shear stress profiles for Poiseuille flow in a cylindrical tube for 'basic' (a), 'inner' (b) and 'outer' (c) masking strategies. Numerical solutions (dashed lines) converge to the exact solution (solid line) with increasing grid resolution. Shear stress profiles are obtained for a number of different grid resolutions $4 \times N \times N$ with $N = 8, 16, ..., 256$. Simulations are done for laminar flow at $Re = 250$.

$$\delta_x u_j \equiv \frac{1}{h}(u_{j+1} - u_j) = \left\{\frac{1}{h}(U(x_{j+1}) - U(x_j))\right\} + (a_{j+1} - a_j) + ... \\ = \left\{U'(x_j) + O(h)\right\} + (a_{j+1} - a_j) + ... \tag{2.30}$$

The term between brackets in (2.30) contains the exact derivative $U'(x_j)$ and a first order correction $O(h)$ associated with the use of the simple finite differencing δ_x to approximate the derivative. In addition, a term $a_{j+1} - a_j$ appears from the error term in the approximation of the solution. This term seems to imply 'zero-order', i.e., no convergence of the numerical derivative. However, if the error term is differentiable, i.e., if we assume $a_{j+1} = a_j + a'_j h + ...$ we obtain first-order convergence of the derivative, also if the accuracy with which the solution itself is approximated is of first order. For the Poiseuille case, the (slow) first order

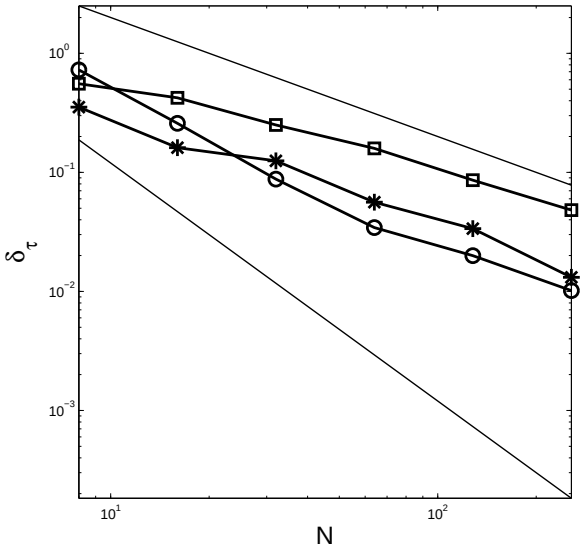

Fig. 2.14 Convergence of shear stress for Poiseuille flow measured in terms of the discrete L_2 norm δ_τ. Solid lines without markers denote slopes -1 and -2 respectively. The line marked with circles ($\circ$) corresponds to the 'inner' strategy, the line with stars ($*$) is for the 'basic' strategy, the line with squares ($\square$) is for the 'outer' strategy for generating the masking function.

convergence as illustrated in Figure 2.14 appears to underpin the differentiability of the error term.

2.4.2 Analysis of the shear stress distribution inside curved vessel and model aneurysm

In this subsection we consider shear stresses in a curved vessel and a model aneurysm. We present the distribution of the shear stress first in two-dimensional cross sections of both geometries and later focus on 1D shear stress profiles.

In Figure 2.15 the distribution of the shear stress is shown as a contour plot of a two-dimensional cross section along the middle plane inside both geometries. We normalize the shear stress field by its maximum value to emphasize the main patterns. High shear stress values are represented as dark areas. We observe that inside the aneurysm cavity a detached jet forms, which impinges on the wall to create a region of locally intensified shear stress. The shear stress τ is also quite large near 'extremities' of the curved cylindrical tube that is connected to the sphere. At the higher Reynolds number $Re = 250$ the results are qualitatively

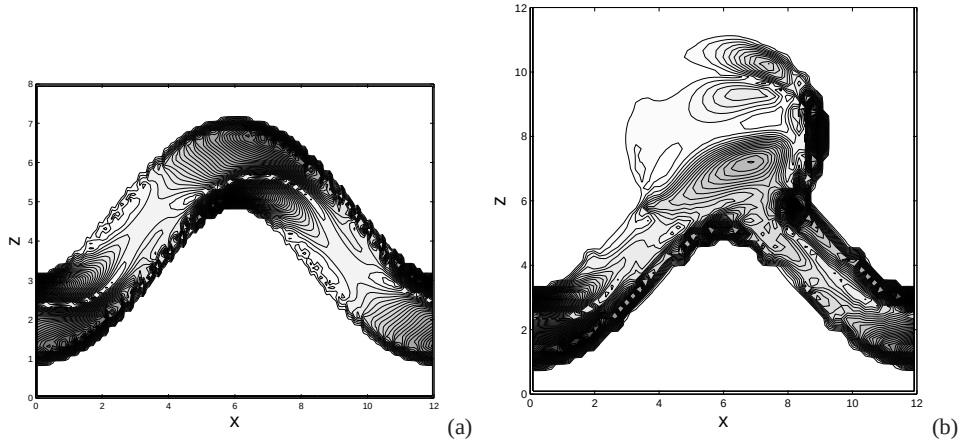

Fig. 2.15 Cross-sectional slices of the normalized shear-stress distribution inside a curved vessel (a) and a model aneurysm (b). The shear stress at $Re = 100$ is shown. High shear stress values are found near the walls of the vessel and near the rims of the attached spherical cavity (dark areas). The spatial resolution that was adopted is $128 \times 32 \times 64$ for the curved vessel (a) and $64 \times 32 \times 64$ for the model aneurysm (b).

similar to the ones at $Re = 100$. In case of the spherical aneurysm we observe a significant separated vortex which dominates the stress distribution on the cavity wall (Figure 2.15(b)).

To consider the accuracy with which τ is predicted in more details, we perform a grid-refinement study and present 1D shear stress profiles. In Figure 2.16 a characteristic stress profile is presented as function of z taken at $(x,y) = (L_x/2, L_y/2)$ at various resolutions. We plot the quantity $(Re\ \tau)$ in order to compare the convergence of the shear stress quite independently of flow conditions.

For each model geometry at both Reynolds numbers $Re = 100$ and $Re = 250$ we notice better capturing of the shear stress profile with increasing grid resolution. Due to the computational time the shear profiles for the model aneurysm are collected at lower resolution (along x-axis) than for the curved vessel. Inside both geometries we observe a complex spatial dependence with peaks near the walls. The value $(Re\ \tau)$ stays approximately the same when the Reynolds number changes in the steady flow regime. This means that with increasing Reynolds number, the shear stress τ decreases, as was also seen for Poiseuille flow in (2.28). We also notice that in the curved vessel the maximum value of the shear stress is about twice as high compared to the model aneurysm. This suggests that having an aneurysm leads to a decrease in the local shear stresses inside the vessel; relocating local maxima partially into the aneurysm body. This was also observed by [84] who reported average wall-shear stress levels about a factor of two lower in the aneurysm than in the nearby vessel region. Although convergence is not complete with our current method, at the resolutions studied, we obtain a reliable impression of τ throughout the domain. Further refinement of the grid was not practical at the adopted Reynolds numbers with the current single CPU implementation of the

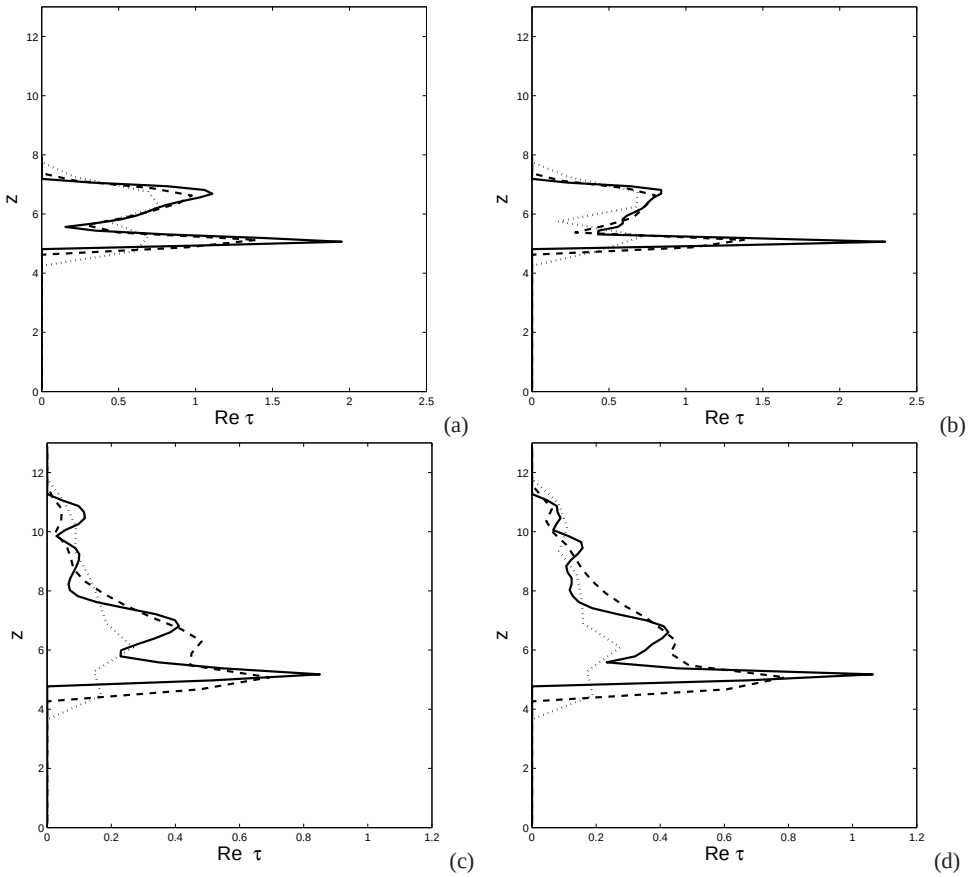

Fig. 2.16 Shear stress profiles in a curved vessel (a,b) and a model aneurysm (c,d). At $Re = 100$ (a,c) and $Re = 250$ (b,d) we show the shear stress profile at different grid resolutions: curved vessel grid resolutions: $32 \times 8 \times 16$ (dot), $64 \times 16 \times 32$ (dash) and $128 \times 32 \times 64$ (solid), model aneurysm grid resolutions: $16 \times 8 \times 16$ (dot), $32 \times 16 \times 32$ (dash) and $64 \times 32 \times 64$ (solid). For the curved vessel (model aneurysm) we use as domain $[L_x, L_y, L_z] = [12, 4, 8]([12, 8, 13])$.

simulation software. In order to simulate long enough until satisfactorily reaching the steady state at $Re = 250$, we face computing times on the order of 100 hours on a modern CPU for a single geometry. Since we employ explicit time-stepping, an increase in resolution by a factor of 2 in each direction, would increase the computing time by a factor of about 16, making the endeavor unfeasible. Current efforts are in the direction of parallel implementation of the flow solver. Linking to existing literature, we can further underpin the reliability of the predictions. The work reported by [89] showed that IB methods are capable of capturing shear stresses throughout the domain with an accuracy that is comparable to that of conventional body-fitted finite-volume discretization. This puts the results in Figure 2.16 into perspective. We expect first order convergence to be maintained also in case of smoothly curved ves-

sels and the model aneurysms, although a strict underpinning with numerical results was not provided in view of the limitations in the spatial resolution that could be employed.

2.5 Concluding remarks

In this chapter we presented a basic immersed boundary (IB) method and its application to the simulation of blood flow in models for cerebral aneurysms. We first described the medical condition and possible ways of diagnostics and treatment of aneurysms. This motivates ways in which mathematical modeling might be applied for surgical support. We introduced a computational model, based on the incompressible Navier-Stokes equations, in which an additional forcing term determines the complex geometry. The masking function assigns to every grid cell the property 'fluid' or 'solid'. Based on the property in the center of a cell, or associated with the corner points, we arrive at three slightly different strategies, called 'basic', 'inner' and 'outer', to define complex-shaped fluid domains. On a 3D Cartesian grid, for any non-aligned geometry we obtain a staircase representation of the fluid-solid boundaries.

The IB method as developed here offers the potential of a more direct computational chain from the raw, somewhat coarse biomedical imagery of cerebral vasculature to a CFD analysis of the flow and shear stresses. In conventional body-fitted methods a time-consuming process of segmentation, smoothing and grid generation has to be incorporated in order to prepare the rough data for such a computational analysis. The IB approach could be less user-intensive and offer the opportunity to develop an automated analysis of the hemodynamics in diseased areas.

A detailed validation analysis of the IB method was provided for Poiseuille flow in a tube with a circular cross section, showing first order global convergence of the numerical solution as well as of its gradients. In particular, we showed the influence of the masking function strategies on the level of accuracy of the numerical flow solution. Based on the validation analysis we choose the 'basic' masking strategy for further simulations.

We applied our method to different geometries, motivated by medical conditions. We included a curved vessels and a model aneurysm. The curved vessel is a cylindrical tube with a sinusoidal centerline, while the model aneurysm is simplified to a sphere merged with the curved vessel. For these geometries we computed velocity fields to understand the behavior of the flow. For different Reynolds numbers we presented a grid refinement study for some flow characteristics and showed convergence of the method.

We also presented shear stresses, as these are often associated with possible rupture of aneurysms. The shear stress distribution in curved vessels and model aneurysms was discussed on different levels: general, 2D cross-section and 1D profiles to quantify the results. We observed the locations of higher shear stresses near the walls as well as near the region where the neck of the aneurysm is connected to the vessel. We noticed that the presence of

an aneurysm causes the shear stress levels to be reduced, compared to the situation without spherical cavity. This is in line with findings reported by [84], who reported a reduction by a factor of two in the average shear stress in the aneurysm, compared to the flow in the connecting vessels. Moreover, we noticed that the peak values of the shear stress are relocated into the aneurysm cavity.

Now, that we established the basic method and its performance, the next step toward a realistic application of computational modeling for flow in aneurysms is to consider actual patient-specific geometries. How to reconstruct the vasculature of patients from medical data and predict flow in complex domains is the topic of the next chapter.

Chapter 3
Flow in cerebral aneurysms derived from 3D rotational angiography

Abstract

In this chapter we present an immersed boundary (IB) method for the simulation of steady blood flow inside a realistic cerebral aneurysm. We reconstruct a segment of the cerebrovascular system that contains an aneurysm, using medical images obtained with three-dimensional rotational angiography (3DRA). The main focus is on evaluating the sensitivity of flow predictions to the various steps of the vascular reconstruction process. Starting from the raw medical data, we analyze the fluid-mechanical consequences of the steps needed to generate the IB masking function for our simulations. We illustrate the IB method by applying it to a realistic aneurysm and investigate the role of (i) numerical resolution of the geometry, (ii) the selection of the specific vascular segment used in the simulations, and (iii) the influence of the smoothness of the periodic vessel extension to complete the computational model. Due to an unavoidable degree of uncertainty in the medical images, the geometry of the vessels and the aneurysm can be reconstructed only approximately. We also incorporate these slight uncertainties in the masking function by introducing inner and outer 'bounding' geometries and analyze the sensitivity of the flow predictions to these variations in the masking function. The numerical solutions computed in the inner and outer bounding geometries provide practical upper and lower bounds for basic flow properties thus quantifying the reliability of the numerical solution, subject to uncertainties in the geometry of the flow domain.

3.1 Introduction

In the diagnostics and treatment of cerebral aneurysms medical imagery plays an important role [57]. Surgeons and neuroradiologists currently make decisions about possible treatment of an aneurysm relying in their judgement on size, shape and location of the aneurysm alone. With computational modeling we propose to support the medical decision process by predict-

ing the numerical flow inside cerebral aneurysms. Numerical methods, which are commonly used for simulation of blood flow in cerebral aneurysms, are mainly based on complex body-fitted meshing for a detailed representation of the geometry of cerebral vessels and aneurysms [17]. However, generating such meshes is a complicated process, during which additional artificial elements arise, e.g., smoothing and simplification of the original image to obtain a 'workable' shape of the vessel [24]. We present an alternative method for reproducing complex geometries – an Immersed Boundary (IB) method, which allows direct transformation of the gray scale voxels from the medical imagery into the geometry of the local vasculature. In the IB approach this complex shape is placed on a Cartesian computational grid. In this chapter we illustrate step by step the reconstruction of the aneurysm geometry from the medical imaging data, obtained using 3D Rotational Angiography (3DRA) and assess the sensitivity of the flow predictions to these steps. We compute steady flow through a realistic cerebral vessel structure under physiologically realistic conditions. The sensitivity analysis will include grid refinement, selection of the particular segment of the vessel structure that is used in the flow analysis and effects of smoothness of the connecting vessel in the definition of a periodic simulation model.

There are several different medical imaging techniques to visualize human cardiovascular and cerebrovascular systems. Depending on the location in the human body and physical sizes of the organs and structures which are being investigated, one or the other imaging procedure is chosen. We focus on cerebral aneurysms, which are commonly located in the Circle of Willis – a central formation in the blood supply to the brain. Complex structure and tiny sizes of these brain aneurysms require detailed scanning possibilities in order to detect even the smallest changes in the geometries. For cerebral aneurysms the most commonly used techniques are 3D computed tomographic angiography (CTA), rotational digital subtraction angiography (DSA) and three-dimensional rotational angiography (3DRA). The voxel size varies from one imaging technique to another. Typically reported values are of the order $0.16\ mm - 0.535\ mm$ [8, 17, 24, 72, 74, 84, 86]. In addition uncertainty is increased because of slight movement of the patient and external noise influencing the recording of the images. A comparison study between CTA and DSA techniques is presented in [72], where DSA is found to be more accurate than CTA for reproducing the shape of a comparably large aneurysm and its relationship to the parent artery. In [95] it is shown that detection of much smaller aneurysms (even with a diameter less than 3 *mm*) is best performed on the basis of 3DRA. From a statistical point of view, in the clinical comparison study described in [96] 78% of the smaller aneurysms were missed using DSA compared to scans employing 3DRA. Another study reported in [11] shows the benefits of 2D DSA over 3DRA in terms of the capability to evaluate the dome-to-neck ratio of intracranial aneurysms, which is an important factor influencing current decisions about endovascular treatment. This hints at a degree of complementarity in the clinical use of DSA and 3DRA. Recently, the differences between CTA and 3DRA techniques were analyzed by comparing CFD computed flow and wall shear

stresses in selected aneurysm geometries reconstructed from each of these techniques [26]. It appeared that the general flow patterns and complexity of the flow were captured with comparable reliability, however the geometry reconstructed from 3DRA data contained more vessels of smaller diameter, which could not be detected with CTA.

In this chapter we describe the process of reconstruction of the aneurysm geometry from raw medical data obtained using 3DRA. We first consider segmentation and simplification processes and then discuss additional steps turning the geometry into the masking function required by the IB method that we adopt for the simulation of the blood flow. The numerical method that we employ in this chapter for illustration of the overall approach operates for convenience on periodic computational domains. The initial aneurysm data should be pre-processed such that a mapping onto the periodic setting is achieved. This requires a few steps. In particular, a segment of the local vessel geometry should be selected, by cutting it from the original data. Subsequently, the selected segment needs to be extended to fit the periodic boundary conditions, by including a smooth connecting tube between outflow and inflow. The aneurysm region of interest should be placed properly separated from the periodic boundaries [12, 17], thereby leading to an accurate model for the flow, without the need to introduce further approximations through actual inflow and outflow conditions [17, 24]. The only external information that is required is the volumetric flow-rate, which can be determined clinically on the basis of transcranial Doppler measurements [78], thus closing the definition of the computational model. The total geometry might be furthermore rotated in order to possibly reduce the numerical effort in case the rotated geometry fits in a smaller domain than the non-rotated original. Rotation could also be beneficial by enhancing the general alignment of the geometry with the underlying Cartesian grid, possibly leading to improved accuracy. In this chapter we will concentrate on two geometry definition ‘tools’: cutting and connecting. We will investigate the effects of applying these tools on the prediction of the total flow, much in the same vein as the comparative CFD study in [26].

Under physiological flow conditions we quantify the size of the original vasculature around the aneurysm that needs to be retained in the computational domain in order to find reliable predictions in the vicinity of the bulge. We focus on three geometries: two ‘long’ geometries (with the recorded vessel cut quite far away from the aneurysm bulge) with different connecting vessels to obtain a periodic flow model, i.e., a smooth connector between outflow and inflow, based on cubic spline interpolation and a straight connector, and a ‘short’ geometry (with recorded vessels cut considerably closer to the aneurysm bulge) supplied with a smooth connector. In this case study the aneurysm bulge has a length of about 2-3 vessel radii. The ‘short’ geometry retains in total a segment of the vasculature of about 6 radii, while the ‘long’ geometries contain about 10.5 radii of the real vessel shape around the aneurysm. We observe no significant differences in the flow in and near the aneurysm bulge when comparing these geometries. In fact, comparing the flow in the ‘long’ geometry with smooth connector to the flow in the ‘long’ geometry with straight connector, shows relative

differences in L_2-norm of less than 10^{-5}. Smooth and straight connectors influence the resulting flow only to some extent (relative differences about 1%) in the actual connecting parts, but this effect is found to remain well localized and separated from the bulge area itself. Flow in the short geometry corresponds to that in the long geometry in the aneurysm bulge up to 10^{-4} relative deviation in L_2 norm and differs only in the connector parts of the vessel. In total, a comparison of these three cases hints at the need to retain a length of the original vasculature of about 3-5 times the length of the aneurysm bulge to obtain flow predictions near the aneurysm that are virtually independent from 'manufactured' details of the flow domain further up- and downstream. This degree of insensitivity to geometry preparation is beneficial for enhancing the reliability of flow predictions.

The capability to simulate the main flow structures in a realistic aneurysm can also be applied to understand the effect of coiling of patients from a fluid-mechanical point of view. The aim of the coiling procedure is to change the pattern of the flow such that the stream of blood is (largely) prevented from entering the weakened area of the vessel. This is approached by filling the bulge of the aneurysm with a slender coil. More recently, this goal is also pursued using flow diverting stents [90]. Since coiling is an operation with some risk to the patient one would like to predict the minimal amount of coiling that would be needed to achieve the required qualitative change in the flow. We illustrate the changes in the flow pattern inside and near a realistic aneurysm bulge that arise when partially filling it with a coil and observe the disappearance of the separated vortical flow pattern with increasing fraction of coiled volume in the bulge.

From medical images the geometry of brain vessels and aneurysms can be reconstructed only with a certain accuracy [72, 95]. We may define a 'basic' geometry on the basis of the segmented raw data. For this basic geometry we compute flow and forces. It is essential to know how reliable these predictions actually are. In order to quantify uncertainties in the predictions due to uncertainties in the precise vessel volume we propose to apply the method of practical bounding solutions [61]. Next to the basic geometry we consider also slightly smaller and slightly larger geometries in the sense of general cross-sectional area, and establish the sensitivity of a range of flow properties to these uncertainties in the problem definition. It appears that flow properties such as velocity profiles, pressure drops over parts of the vessel structure and shear stresses, as computed in 'inner' and 'outer' bounding geometries are also bounding the corresponding properties obtained in the basic geometry from below and above. This is helpful to quantify the sensitivity to small changes in the geometry.

The organization of this chapter is as follows. In Section 3.2 we present the numerical model for the simulation of blood flow inside cerebral vessels and describe the process of constructing the masking function from the raw medical data. We also introduce cutting and connecting as elementary operations to define the masking function. In Section 3.3 we define the reference aneurysm geometry and discuss properties of the blood flow, by comparing results at different spatial resolutions. Sensitivity of flow predictions to elementary operations

on the masking function is presented in Section 3.4. The method of bounding geometries and the corresponding quantification of the numerical results to uncertainties in the precise geometry definition are described in Section 3.5. Concluding remarks are in Section 3.6.

3.2 Computational model for blood flow in cerebral aneurysms

In this section we present the computational model for simulating blood flow inside cerebral aneurysms. We first introduce an immersed boundary method to represent complex vessels and aneurysm geometries. Then, in Subsection 3.2.2, we describe the process of the reconstruction of a realistic aneurysm geometry from raw medical data obtained using 3D rotational angiography. Subsequently, in Subsection 3.2.3 we introduce additional procedures that can be used for the construction of the masking function as used in the IB method.

3.2.1 Navier-Stokes equations and immersed boundary method

There is a number of different approaches to model flow of blood in the human brain. A comprehensive overview is given in [76]. One such approach is to represent blood as an incompressible Newtonian fluid with a constant viscosity [14]. We consider vessels of the Circle of Willis with diameters of $2-4$ *mm* [39], while the typical size of the structures in blood is $6-17$ μm. In fact, blood cells are mainly red blood cells and white blood cells, whose diameters are found to be $6-8$ μm and $12-17$ μm respectively [88, 105]. Based on the differences in scale of about 3 orders of magnitude, we approximate blood in cerebral vessels as a Newtonian fluid. Comparative studies were presented in [15, 24, 28, 38], where non-Newtonian corrections were found to be not the major limitation for the overall accuracy of the computational model.

The incompressible Navier-Stokes equations, completed with a no-slip boundary condition on the vessel walls are given by:

$$\frac{\partial \mathbf{u}}{\partial t} + \mathbf{u}\cdot\nabla\mathbf{u} = -\nabla P + \frac{1}{Re}\nabla^2\mathbf{u} + \mathbf{f} \tag{3.1}$$

$$\nabla\cdot\mathbf{u} = 0 \tag{3.2}$$

where $\mathbf{u}$ is the velocity of the fluid in the domain Ω_f and it is understood that $\mathbf{u} = \mathbf{0}$ on the vessel walls at $\partial\Omega_f$ which are taken as rigid in this study (extensions to slightly moving vessel walls were investigated in [69]). In addition, P is the pressure and $Re = U_r L_r/\nu_r$ is the Reynolds number, in terms of a reference velocity U_r, a reference length scale L_r and the kinematic viscosity ν_r. We take as length scale the size R of the vessel connecting to an aneurysm cavity. The reference velocity is taken as $U_r = Q_r/A_r$ in terms of the volumetric

flow-rate Q_r and the cross-sectional area of the non-diseased part of the vessel A_r close to the aneurysm bulge.

The velocity inside the tissue regions and at the wall should vanish in view of the adopted no-slip condition and the rigidity of the interface. The forcing term $\mathbf{f}$ in the volume penalization IB method represents this impenetrability of the solid [62] and is given by

$$\mathbf{f} = -\frac{1}{\varepsilon} H(\mathbf{x})\mathbf{u}(\mathbf{x},t) \tag{3.3}$$

The control parameter $\varepsilon = 10^{-10}$ as proposed in [54] and $H(\mathbf{x})$ is the so-called 'masking function': if $\mathbf{x}$ belongs to a fluid part Ω_f the masking function $H(\mathbf{x}) = 0$ and it is 1 otherwise. Correspondingly, around a fluid location the Navier-Stokes system is employed. The forcing inside the solid domain dominates all other fluxes in the Navier-Stokes equations in case the velocity would be large compared to ε. As a result, inclusion of the forcing term renders the velocity negligible in the solid part of the domain if we choose ε sufficiently small. In the region near the vessel walls the velocity field is forced to negligible values within a very thin strip of the solid-fluid interface. The vessel wall itself is represented by a 'staircase' geometry. In fact, a grid cell is allowed to be either 'solid' or 'fluid'. Refinements involving smooth reconstruction of the vessel walls are not incorporated in this study, primarily because the raw medical imagery does not allow a robust, more sharply localized geometry definition without a strong element of potential 'user-influence'. The spatial localization of the fluid-solid interface, after segmentation, is hence given by the mesh-size of the Cartesian grid that is adopted.

The Navier-Stokes equations are treated with a finite-volume discretization that preserves the skew-symmetry of the nonlinear convective fluxes and the positive-definite dissipative nature of the viscous fluxes [100]. A second order accurate method for the fluxes is employed, implemented on a staggered grid. The contribution of the forcing term $\mathbf{f}$ is integrated implicitly in time, which overcomes stability problems that would arise with explicit methods as $\varepsilon \ll 1$. The total computational domain is endowed with periodic boundary conditions.

There are many ways of generating a masking function. For some model geometries the masking function can be specified analytically as a combination of simpler geometrical figures, as was shown in the previous chapter, where flow in a cylindrical tube, curved vessel and curved vessel with a spherical cavity on it were discussed. In case of realistic aneurysm geometries the masking function is extracted from the medical images, obtained during diagnostic procedures. We create a computational domain which contains the scanned volume. For every grid cell (voxel) we determine whether it belongs to the brain tissue (solid) or to the blood vessel (fluid). Applying this to all locations in the Cartesian grid, we can characterize a point as 'solid' or 'fluid'. This can be done, e.g., for the center of the cell as well as for its 8 corners. To define the value of the masking function in that particular cell, we translate the information contained in these 1+8 numbers into a single decision about fluid (value '0') or solid (value '1'). In this way, 9 slightly different masking functions can be created. For

example, we can call the cell ‘solid’ already if only one or two of its corner points are solid. This will ‘favor’ the decision for ‘solid’ over ‘fluid’ in the resulting definition of the masking function. Another example could be that a cell gets the value ‘1’ only if all 8 of its corner points are solid. In that case there will be fewer solid cells and more fluid cells. Thus, the amount of solid corner points between 1 and 8 leads to 8 possible geometries. The 9th option is based on the center of the cell, when we define the masking function of the whole cell by its value in the center. We will refer to the latter as the basic geometry, while the 8 other geometries we call bounding geometries, as they actually bound the volume of the basic geometry from the ‘inside’ or the ‘outside’. All in all, these 9 possibilities will differ only slightly in the resulting masking function - the solid-fluid interface will be defined within one grid cell variation, i.e., ideally an uncertainty of one voxel. The main question is how sensitive predictions are to these small differences.

3.2.2 Segmentation of 3D rotational angiography data

3DRA is a modern imaging technique, which allows to visualize vessel structures in the human brain [17, 95]. This method of imaging is a cone-beam computed tomography imaging modality present on Philips rotational angiography systems (Integris BN 3000 Neuro; Philips Medical Systems, Best, the Netherlands). During diagnostics or while coiling a brain aneurysm, the position of the catheter is often guided by X-rays, mounted, e.g., on a C-arm system. In 3DRA the C-arm is rotated around the patient while iodinated contrast agent is being injected. This technique allows to obtain acquisitions over 180 degrees. The projection images are then transformed back to a 3D volume using a cone-beam algorithm based on a modified filtered back projection [104]. The average number of images per investigation of a patient is about 100, with a frame rate of 12.5 frames per second during a total acquisition time around 8 seconds [95].

The vessel geometry that is used to illustrate the simulation methodology in this chapter is from a 3DRA scan of the Circle of Willis in a patient suffering from a brain aneurysm (St. Elisabeth hospital, Tilburg, The Netherlands). A sample of the raw data is shown in Figure 3.1, displaying cross-sections through the recorded volume, with vessel structures highlighted in white. The 3D volume data is first segmented to obtain the vessel geometry and it is simplified later to allow flow simulations. We discuss the main steps next.

Gray scale images of every 2D slice of the scanned volume represent areas of contrast fluid and soft tissue in the brain. Every pixel has a gray shade and contains intensity information - a value in the range between 0 (black) and 1 (white). Depending on the input parameters for the scanning procedure and expectations of the output, one can visually recognize vessels with contrast fluid and different types of soft tissue around them. For cerebral aneurysms the main interest is in those pixels which are ‘colored’ by contrast-fluid values, as they represent

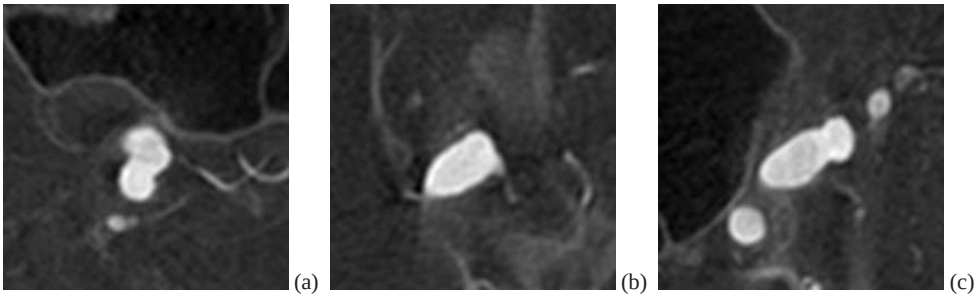

Fig. 3.1 Cross sections through raw medical data obtained from 3DRA, provided by W.J. van Rooij and M. Sluzewski (St. Elizabeth Hospital, Tilburg, The Netherlands). The chosen geometry is shown in cuts in three mutually perpendicular planes in (a), (b) and (c). The lighter colored regions correspond to fluid filled vessels while the darker regions identify the 'solid' impenetrable domains. The real size of these images is 3.10528 *cm* on the side of each square. The scan resolution is 256 points per direction leading to a uniform voxel size of 0.1213 *mm*.

the blood flow and hence the shape of the vessel. For the 3D reconstruction of the vessel geometry the decision for every voxel, whether it has contrast fluid or represents tissue, has to be made. For this purpose a thresholding procedure is adopted, in which a threshold value defines the 'border' intensity for tissue and hence also for the contrast fluid. A value 0.7 was used as a threshold value, which implies that all voxels with an intensity value less than 0.7 will be interpreted as tissue (black) and otherwise the voxel will become fluid (white). In this way we obtain a binary set of data which represents the shape of blood vessels.

The output thresholded image may contain 'holes' arising from projection errors of possibly recorded noise, or limited spatial resolution. For reconstructing the vessel shapes this would mean that inside the blood vessel non-realistic areas of tissue would appear or inversely small non connected parts of blood vessels would erroneously appear located in the tissue. These problems can be solved by simplifying the geometry, following standard techniques in digital image processing [30].

In Figure 3.2 we illustrate all reconstruction steps for the vessel system. The initial gray scale image is introduced in Figure 3.2(a). After thresholding it changes into black and white (Figure 3.2(b)), with some 'holes' (or extra noise) inside the vessel. Then, by filling the holes we arrive at Figure 3.2(c), which is already a binary image with an exact vessel geometry. For simulation of the flow inside cerebral aneurysms we restrict ourselves to the main vessel containing the aneurysm, and do not include the small branch vessels. Corrections due to inclusion of secondary side branches were recently considered by [77]. Allowing the single inflow/single outflow approximation, the geometry is further simplified. We erode the image (Figure 3.2(d)) and label all the connected objects [33] (Figure 3.2(e)). We keep only the largest object from Figure 2(e), which corresponds to the main vessel structure (Figure 3.2(f)) and apply dilation for reconstructing the original shape of the main vessel structure (Fig-

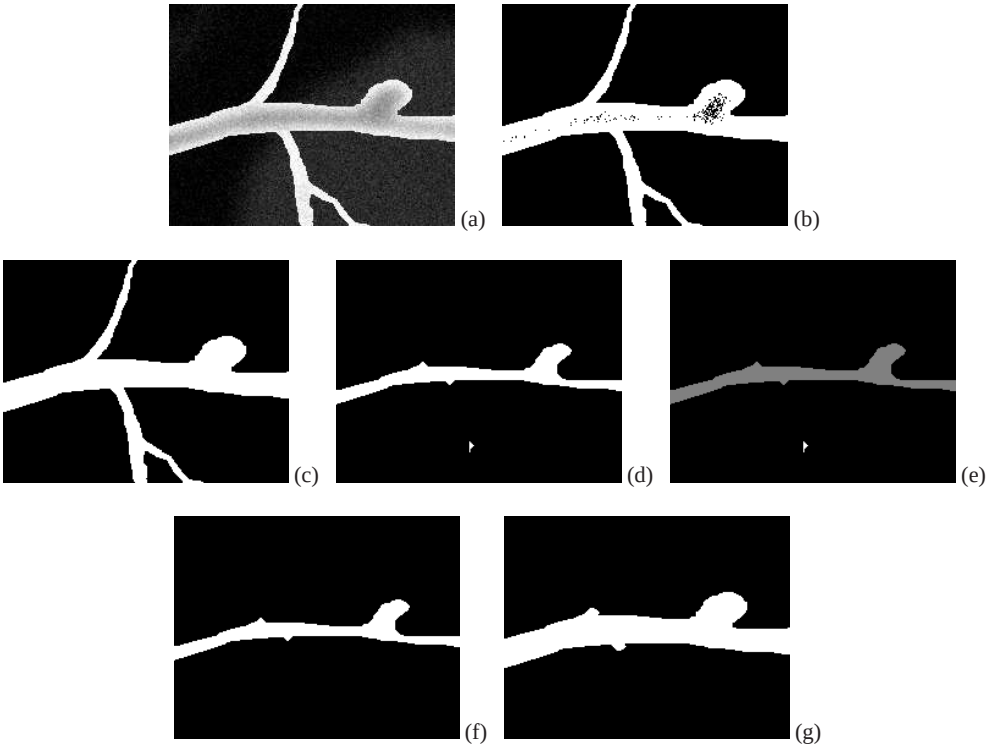

Fig. 3.2 Two-dimensional schematic illustration of vessel definition from raw data: initial image (a), after thresholding (b), with filled holes (c), eroded image (d) from which small side branches are deleted, labeling of the connected regions (e), selection of the largest object (f), dilated final image (g) containing the main vessel and the selected aneurysm bulge, free of side branches.

ure 3.2(g)). In morphological image-processing 'erosion' and 'dilation' are two more or less complementary operations. While erosion of the image removes features which are smaller than a chosen reference scale (referred to as the 'structuring element' [30]) from the image, dilation of the image allows to 'expand' the volume again returning to the original size, but without adding small-scale details. More details and mathematical description of the steps in this reconstruction process can be found in [30]. The application of this series of steps leads to the complete geometry as shown in Figure 3.3(a). This shows the complex vessel structure with the main cerebral vessel, which contains an aneurysm, and several small branch vessels up- and downstream of the aneurysm. Removal of the side branches and reconstruction of the main vasculature leads to Figure 3.3(b), which forms the starting point for further systematic numerical analysis.

The choice of the threshold value introduces some uncertainty in defining the exact geometry [10]. Moreover, the choice of parameters during the simplification process [30] also introduces some potential 'user-related' variability in the geometry definition. In this chapter

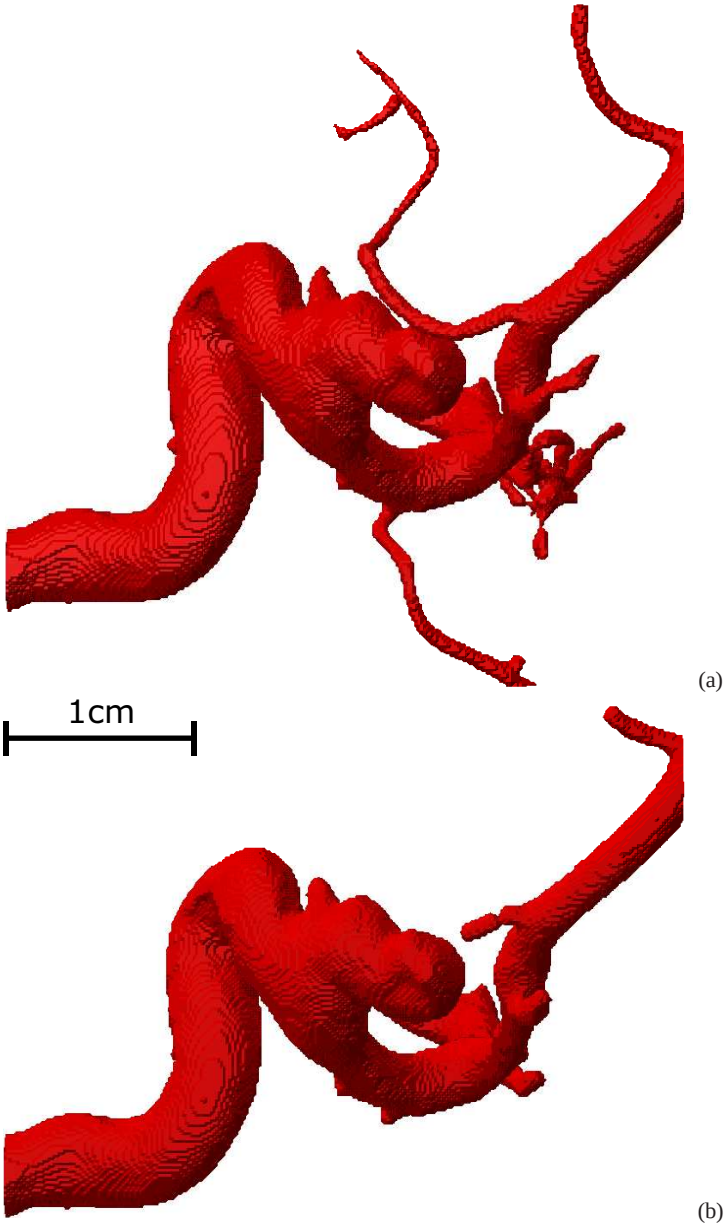

Fig. 3.3 The segmented geometry (a) and the simplified geometry without side branches (b). The physical length scale is shown to give a rough indication of the actual size of the chosen vascular segment. The aneurysm bulge is about 1 cm in length, while the vessel diameters are varying approximately from 3 to 5 mm.

we do not look into the differences in geometry generated during segmentation and simplification processes. Instead we consider bounding geometries, which illustrate the whole range of possible slightly larger and smaller geometries within an uncertainty of the order of a voxel grid cell in the computational model. In this way we will analyze the effect of the reconstructed geometry on the computed flow. This approach can readily be extended to also address effects from segmentation and simplification - however, this is beyond the scope of the present chapter.

3.2.3 Elementary operations on the masking function

After the segmentation and simplification processes the geometry obtained is presented in Figure 3.3(b). This geometry can be used to finalize the definition of the masking function. Important remaining steps are (a) the selection of the appropriate segment for which the fluid-mechanical analysis will be conducted and (b) the incorporation of this flow problem in the periodic setting. In order to optimize the definition of the masking function we require the ability to respectively perform 'cutting' and 'periodic re-connection' of the masking function. We address these basic operations next.

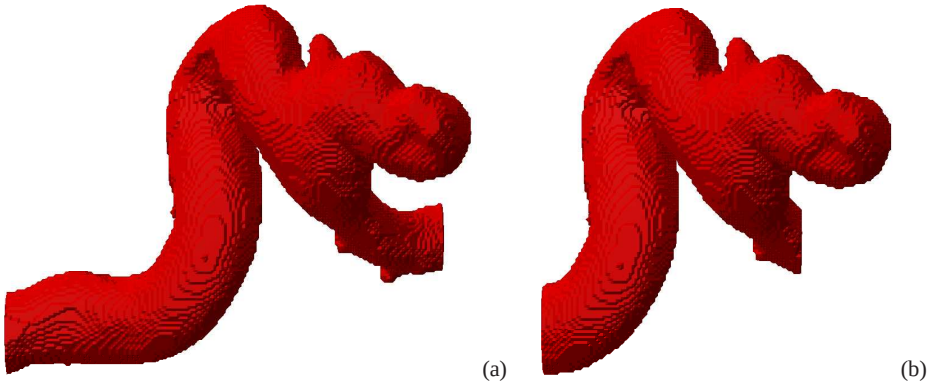

Fig. 3.4 Masking function of the realistic aneurysm geometry: the first option is shown in (a), cut farthest from the aneurysm bulge and the second option is in (b), cut closer to the aneurysm.

Cutting. We start from the geometry, illustrated in Figure 3.3(b) and as first basic operation introduce 'cutting'. This is done simply by cutting the vessel in a plane at constant x. We make sure that only the connecting vessel is affected and not the main bulge. In Figure 3.4(a) we cut the vessels from both sides of the aneurysm bulge. In order to define the reference geometry we cut away as far as possible from the bulge, all the way to the bifurcation of the vessels downstream of the aneurysm (Figure 3.4(a)) consistent with the single inflow, single

outflow restriction that was selected. This choice of location at which to cut the geometry is quite arbitrary - hence, to assess the influence of the selection of the particular segment of the vessel on the flow predictions we will also cut the geometry more tightly, i.e., from both sides closer to the aneurysm. The second cut geometry is plotted in Figure 3.4(b). We will refer to these geometries later as the 'long' and the 'short' geometry respectively.

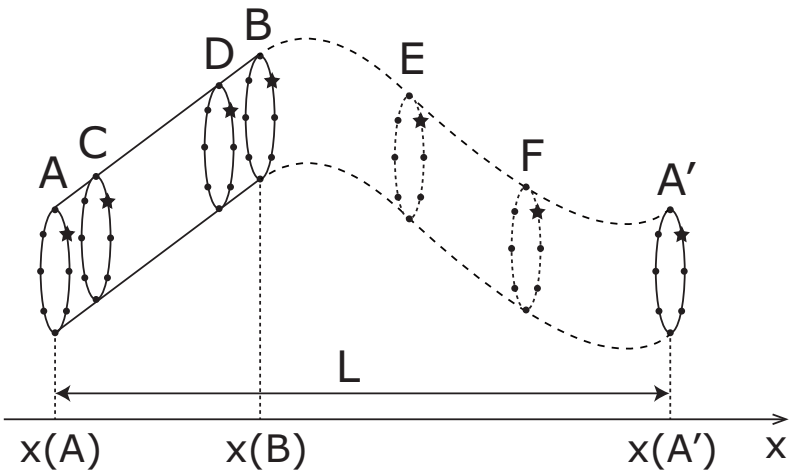

Fig. 3.5 Schematic illustration of the periodic extension of a cylindrical tube segment AB to period L. The original tube section AB is shown with solid lines, the smooth connector that is added is shown dashed. On each cross section a number of nodes is added at the location of the vessel wall - the nodes in each cross section are labeled clockwise. To define numerical directional derivatives the cross-sections nearest A and B are indicated as well, C and D respectively. To create a periodic extension consistent with period L, the cross-section A is translated over L to form A' and a spline (linear or cubic) is drawn between 'corresponding' points on B and A', where 'corresponding' refers to the same label of a node in clockwise direction in a cross-section. One corresponding point is marked by an asterisk on every cross-section. Sample intermediate cross-sections are indicated by E and F.

Connecting. After cutting, the geometry needs to be prepared for the periodic flow model. We periodically 'connect' the ends of the cut geometry by adding a section of continuous connecting vessel. A schematic illustration for a cylindrical tube is given in Figure 3.5. We start from the recorded cut vessel ends A and B and consider cross-sectional contours in the yz plane. On every contour representing the vessel we introduce a large number of ordered nodes M, typically several hundred. These nodes are placed on the contour separated by a small angle $\alpha = 360/M$ in degrees. We call nodes at the same angle 'corresponding' nodes. The geometry is translated over one streamwise period of length L, such that the inflow contour A is translated into A'. The challenge is to generate 'intermediate' connecting cross sections of a numerical vessel that links the outflow B to the translated inflow A'. For this we adopt two options, i.e., linear or cubic spline interpolation between each pair of corresponding nodes.

Interpolation based on a cubic spline requires the nodes on the outflow B and translated inflow cross-sections A', the length of the connecting part $x(A') - x(B)$ and the tangent vectors at the outflow/inflow nodes, specifying the orientation of the cut vessel ends in 3D space. Typically we add a piece of interpolated vessel of the same length as was taken away during the cutting operation. In the numerical setting it implies that if k grid cells in x-direction were cut away during the cutting step, then exactly k newly generated slices (yz planes) will be added to the cut geometry. In this way we keep the initial physical sizes of the 3D brain segment of the same size.

The cubic Hermite polynomial s is defined as

$$s(\xi) = (2\xi^3 - 3\xi^2 + 1)s_0 + (\xi^3 - 2\xi^2 + \xi)m_0 + (-2\xi^3 + 3\xi^2)s_1 + (\xi^3 - \xi^2)m_1$$

where $\xi \in [0,1]$, s_0 is the start point at $\xi = 0$ and s_1 its corresponding end point at $\xi = 1$, m_0 and m_1 are start and end tangents respectively. We consider two adjacent slices from each end of the original vessel C and D to define the required tangents in each of the inflow/outflow nodes. Specifically, to compute tangent vectors $m_j = [m_{xj}, m_{yj}, m_{zj}]$ at all points j on contour A, we define

$$m_{xj} = (x(C)_j - x(A)_j)/(x(C)_j - x(A)_j) = 1 \tag{3.4}$$

$$m_{yj} = (y(C)_j - y(A)_j)/(x(C)_j - x(A)_j) \tag{3.5}$$

$$m_{zj} = (z(C)_j - z(A)_j)/(x(C)_j - x(A)_j) \tag{3.6}$$

This is the basis for the interpolation. We determine the cubic Hermite polynomial associated with every set of corresponding points on the contours B and A and generate k interpolated points in between. In this way we obtain new contours containing M points, which allow to connect outflow B with the translated inflow A'. In Figure 3.5 in the interpolated part of the tube between outflow B and translated inflow A' we also illustrate intermediate interpolated contours E and F. For linear interpolation we operate only with points on contours B and A' and connect corresponding points on them by a straight line, which leads to a straight tube as connector.

Applying the connecting operation to the aneurysm geometry we obtain a continuously differentiable tube in case of cubic spline interpolation and a straight continuous tube for linear interpolation. In Figure 3.6 we show an example of the interpolated connector between the outflow and the translated inflow for a particular pair of corresponding points on the B, A' contours for cubic spline interpolation (Figure 3.6(a)) and linear interpolation (Figure 3.6(b)). The 3D masking functions for both cases are presented in Figure 3.7. We illustrate two long geometries with different connectors and a short geometry with smooth connector.

In Section 3.4 we will analyze the effect of the discussed ‘tools’ of cutting and connecting by simulating steady flow in the obtained geometries and analyzing flow properties. In the

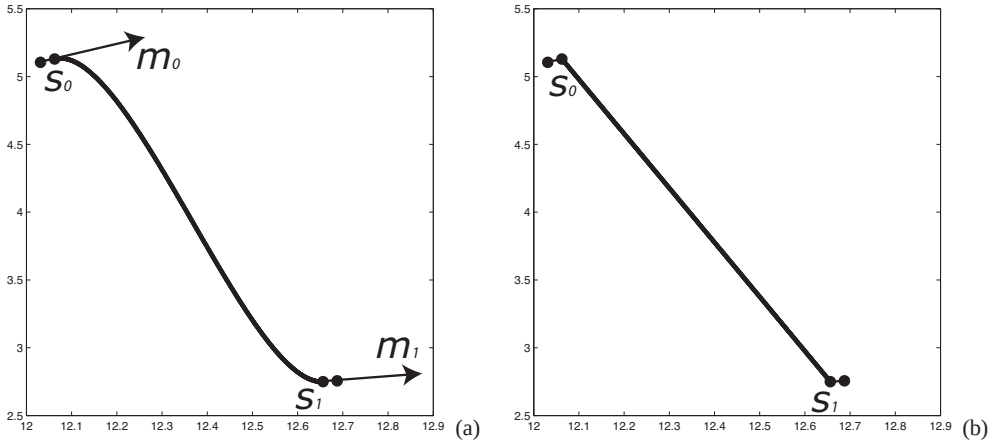

Fig. 3.6 Example of interpolated vessel between ends of the cut cerebral vessel. For cubic spline interpolation (a) vectors m_0 and m_1 indicate the direction of the tangent and hence the local orientation of the vessel in space. In (b) we show linear interpolation between the two end points. Nodes with markers indicate original nodes on the first, second, last but one and last slices of cut-vessel (two from each side).

next Section we first turn attention to the actual flow that develops in the selected reference geometry at realistic flow conditions.

3.3 Flow in a realistic aneurysm

In this section we present numerical results for the flow inside the realistic aneurysm geometry that was introduced in Subsection 3.2.2. We set up the reference case for our numerical simulations and discuss the physiological conditions that characterize the flow, in Subsection 3.3.1. Afterwards we perform simulations for a steady flow and present the numerical solution (velocity and pressure) and its derivatives (in terms of the shear stress) in Subsection 3.3.2. Subsequently, we consider the general convergence of the predictions in terms of the pressure drop, velocity and shear stress in Subsection 3.3.4.

3.3.1 Motivation and definition of the reference case

As reference case we choose the long geometry (Figure 3.4(a)). The ends of this segment are connected by a cubic spline interpolation. The 3D masking function of the reference geometry is shown in Figure 3.7(a). Before simulations can be done to understand the flow in the aneurysm bulge, some further preparations are required to identify the relevant range of

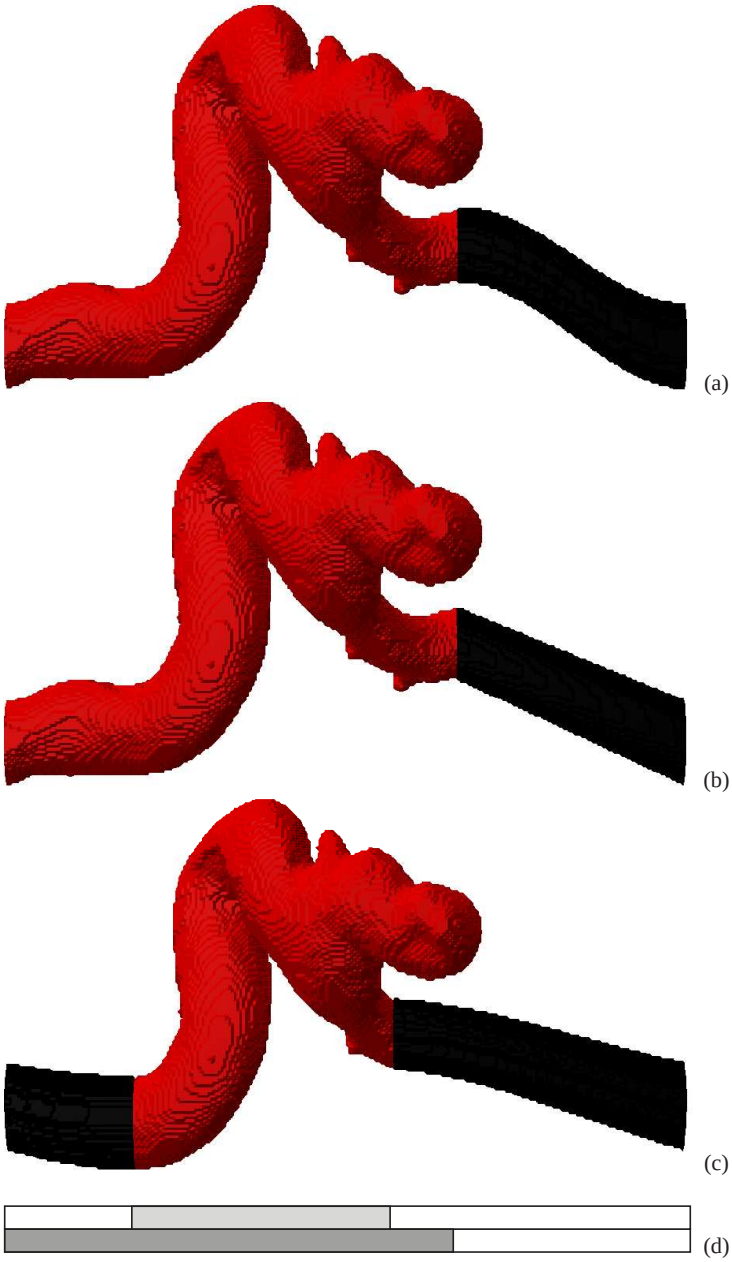

Fig. 3.7 Masking functions for connected geometries. The selected geometry is plotted in red, while the connectors are shown in black. Reference geometry (long with a smooth connector) is presented in (a), the long geometry with linear connector is in (b), the short geometry with a smooth connector is in (c). A schematic indicator of the different 'original' (gray) and 'interpolated' (white) segments is plotted in (d), where light grey shows the borders of the short geometry and dark grey represents the x-range of the original part in the long geometry. We will use this indicator in the sequel, which allows to interpret the simulation results more easily.

physiological conditions for blood flow inside the aneurysm. Subsequently, we will visualize the solution in a number of qualitative ways to appreciate the complexity of the flow structures that develop.

In order to specify the computational model we need to choose reference scales for length and velocity, and specify the kinematic viscosity. These quantities allow to compute the Reynolds number *Re*, which is the only parameter that is required for the dimensionless formulation. From literature one may find a range of values characteristic of these reference scales, which implies some degree of freedom in setting the precise values that are physiologically relevant. We motivate our choices next to provide a point of reference.

The raw data of the 3DRA scan of the aneurysm consists of a grid of 256^3 voxels. The voxel width is 0.1213 *mm*. This implies that the total physical length of the domain is 3.10528 *cm*. As reference length we take a characteristic scale representative of the average radius of the cerebral vessel in this part of the Circle of Willis. We extract $R^* = 1.94$ *mm* from the 3DRA data. This value is quite similar to [24] who adopt 2.5 *mm*, and also consistent with [39], who suggests a scale of 2.1 ± 0.4 *mm*. Hence, in the non-dimensional setting we work in a domain of total 'length' of $31.0528/1.94 \approx 16$. The computational domain, enclosing the aneurysm geometry is in fact a rectangular block of size $16 \times 8 \times 16$ in the non-dimensional formulation. This size of the total computational domain is sufficient to enclose the vessel geometry after segmentation and simplification - in the *z* direction a factor of two could be saved because of the particular orientation of the initially provided geometry.

Next to the length-scale, also the viscosity and the velocity scales need to be set. From literature we infer that the mass density ρ^* is in the range $1025 \leq \rho^* \leq 1125$ kg/m^3, while the dynamic viscosity of blood is reported to be $3 \cdot 10^{-3} \leq \mu^* \leq 4 \cdot 10^{-3}$ *Pa s*. Specifically, choosing typical values for the mass density of blood $\rho^* = 1060$ kg/m^3 and the dynamic viscosity of blood $\mu^* = 3.2 \cdot 10^{-3}$ *Pa s* implies a kinematic viscosity $\nu^* = \mu^*/\rho^* = 3.01 \cdot 10^{-6}$ m^2/s. Finally, the reference flow-rate as proposed by [34] and [67] is 245 ± 65 ml/min, showing an uncertainty of about 25%. This range of values was obtained on the basis of either 3D MR angiograms or Doppler measurements. The corresponding range for the velocity scale can be extracted from this as $U^* = Q^*/(\pi(R^*)^2) = 0.345 \pm 0.09$ m/s. This is consistent with the range 0.34 ± 0.087 m/s as obtained by [78] on the basis of Doppler measurements. Combining these numbers yields a typical Reynolds number range of $175 \lesssim Re \lesssim 300$. For convenience, we adopt $Re = 250$ in the sequel, which, in terms of the chosen reference length-scale and kinematic viscosity, corresponds to a velocity scale of $U_r^* = 0.388$ m/s, well within the quoted range found in literature. We will simulate steady blood flow at $Re = 250$. This requires simulating an initial condition long enough until a steady state is approximated with high accuracy. We simulate until the time at which the total pressure drop across the domain, needed to maintain the imposed flow rate shows a relative variation of less than 10^{-3}. This was found to be adequate for predicting the steady conditions properly - we also considered

as stopping criterion a 10 times lower tolerance and observed only negligible differences in the solution.

3.3.2 Qualitative impression of flow and forces inside the aneurysm

In order to visualize the flow and forces that develop in the aneurysm geometry, a number of options is available. We will start by choosing a more qualitative set of methods, i.e., three-dimensional and two-dimensional views of the velocity and shear stress. Here, we show results obtained at a resolution of $128 \times 64 \times 128$. A quantitative approach, showing the effect of grid refinement will follow in the next subsection.

Numerically computed velocity streamlines for a steady flow at $Re = 250$ are presented in Figure 3.8(a). By properly selecting the initial condition for the streamline at the inflow on the left-hand side of the domain, we can achieve both streamlines that pass through the section with the aneurysm, without actually entering the aneurysm bulge, as well as streamlines that display the rather complex vortical pattern that appears within the aneurysm. The geometry is colored with the value of the local pressure. A smooth transition from a higher pressure on the left to a lower pressure on the right can be observed, driving the imposed volumetric flow rate inside the geometry.

To get an alternative impression of the velocity field, in Figure 3.8(b) we present the velocity vector field in a few cross-sections along the aneurysm geometry. The cross-sections are taken in *yz* planes. The flow in more or less cylindrical tube sections of the local vessel system shows similarity to a parabolic profile, reminiscent of Hagen-Poiseuille flow. We notice that near the aneurysm bulge the dominant flow still follows what used to be the non-diseased tract. However, also near the 'neck' and within the aneurysm there is considerable dynamics, showing regions of forward and backward flow, as illustrated in the velocity vectors. In the middle cross-section at $x = 0$ this is nicely illustrated with flow entering as well as exiting the aneurysm in a complex vortical sweep; the flow comes back from the aneurysm after having circulated in it. The flow structure inside the aneurysm also leads to higher residence time of red blood cells, and correspondingly a reduced quality of circulation that might even induce the formation of small cloths. The flow structure in the aneurysm bulge is also correlated with regions of lower levels of wall-shear stress, as the flow-intensity in the aneurysm is rather low leading to gradual degeneration of endothelial cells [21].

A closer impression of the flow inside the aneurysm can be obtained by considering contour plots of velocity components. In Figure 3.9 we show a particular contour of the streamwise velocity component at $x = 0$, which is through the actual aneurysm, i.e., a section through the middle in Figure 3.8(b). We show a cross-section in the *yz*-plane at a number of spatial resolutions. The grid refinement shows a clear qualitative convergence toward the grid-independent solution. The resolution $32 \times 16 \times 32$ is insufficient to capture the full com-

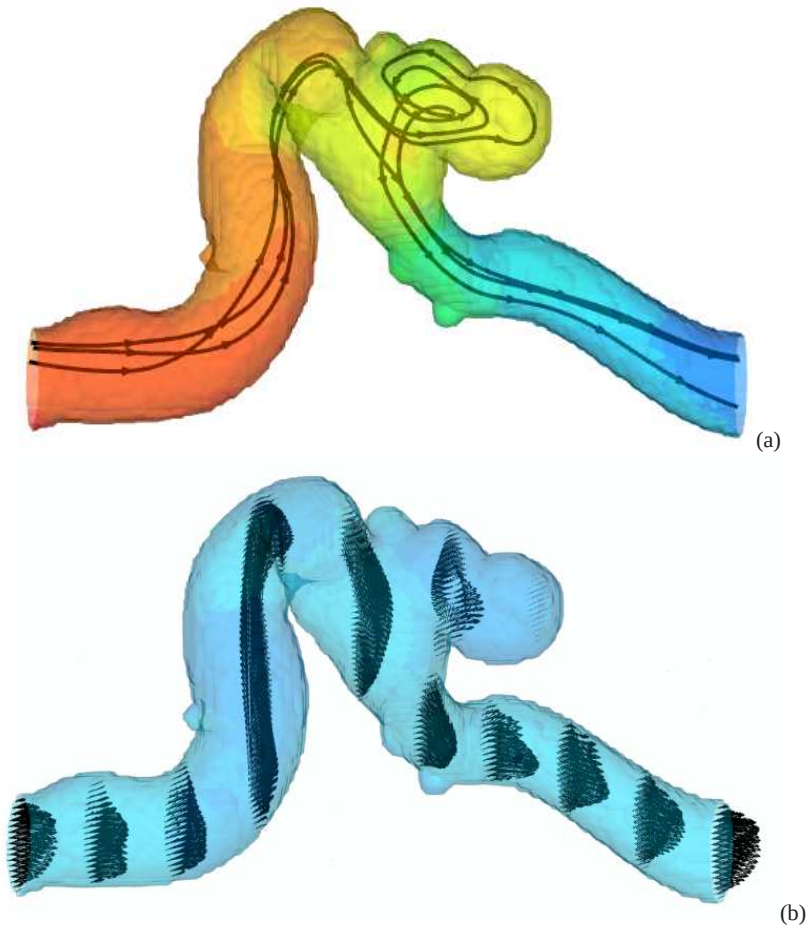

Fig. 3.8 Three characteristic velocity streamlines (a) inside the aneurysm geometry. The geometry is colored with the pressure field which shows a smooth transition from a high pressure (red) to a low pressure (blue). In (b) we show the velocity vector field in a few cross-sections. The cross-sections are at several x locations in yz planes, largely perpendicular to the flow direction. Grid resolution is $128 \times 64 \times 128$.

plexity of the flow. However, the main features are already captured properly at a resolution of $64 \times 32 \times 64$, while high accuracy results can only be expected by further increase of the resolution. We notice both dark and light colors in this contour plot, corresponding to positive and negative streamwise velocities. These show a region of recirculating flow in the aneurysm, next to the main through-flow represented by the dark region in the lower left corner of each contour plot. We also investigated the dependence of the flow prediction on spatial resolution at other streamwise locations and found similar qualitative convergence. A more precise assessment of the level of convergence is considered momentarily.

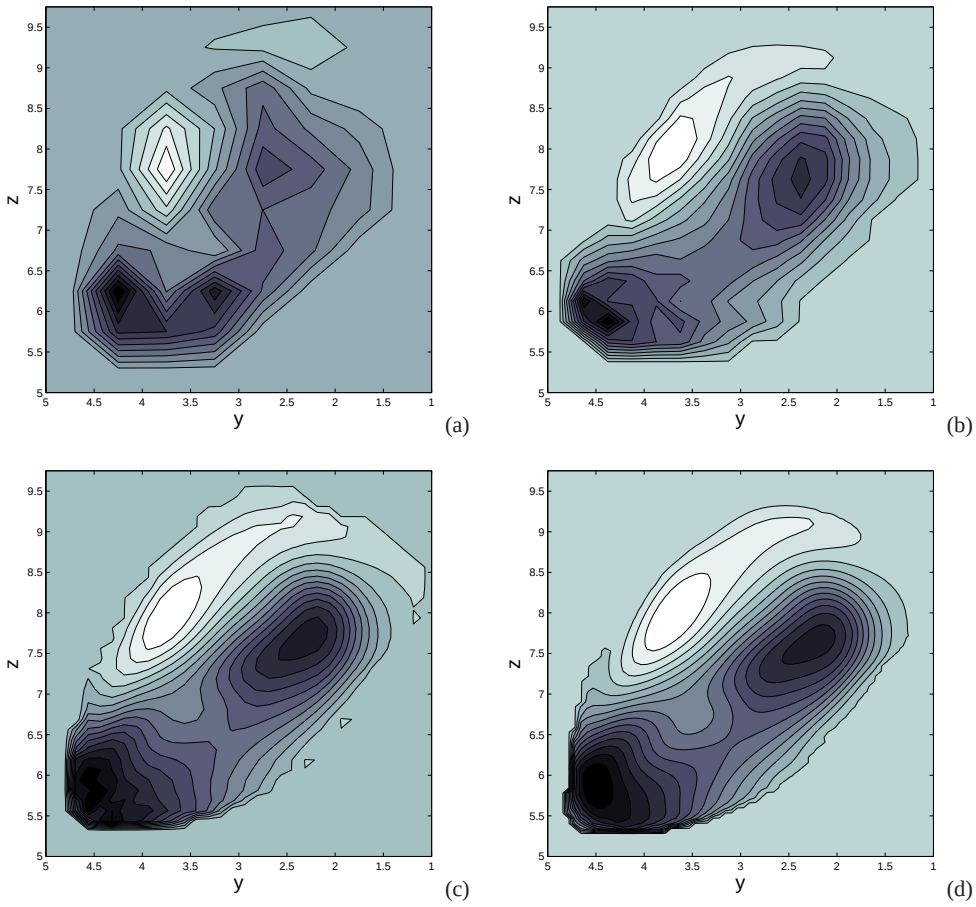

Fig. 3.9 Contour plot of the streamwise u-velocity in a yz cross-section in the middle of the geometry at $x = 0$. Dark regions correspond to high positive velocities, while the lightest contours are related to regions of negative velocity; we adopt the same color-coding for all figures. The flow structures show a vortex inside the aneurysm. We present the velocity contours in the same plane for different grid resolutions: $32 \times 16 \times 32$ (a), $64 \times 32 \times 64$ (b), $128 \times 64 \times 128$ (c) and $256 \times 128 \times 256$ (d).

Regions of relatively high and relatively low shear stress are considered important markers for the risk of aneurysm growth. These can be obtained from the simulations as well, by post-processing the velocity field. The shear stress τ is defined in non-dimensional form as

$$\tau = \frac{1}{Re}\sqrt{2S_{ij}S_{ij}} \tag{3.7}$$

where $S_{ij} = (\partial_i u_j + \partial_j u_i)/2$ denotes the rate of strain tensor. A global impression of the wall shear stress distribution is given in Figure 3.10. Regions of high shear stress are concentrated near relatively sharp bends in the vessel and near the 'neck' of the aneurysm, where the bulge connects to the previously unaffected vessel. Inside the aneurysm the shear stress is rather

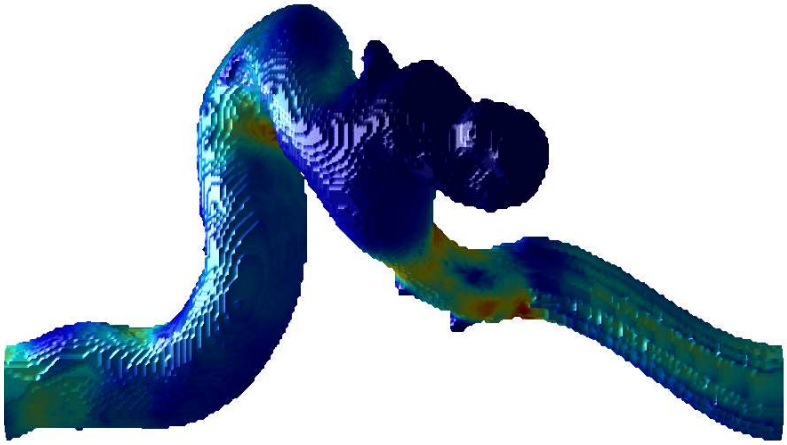

Fig. 3.10 Distribution of the wall shear stress, computed at $Re = 250$ at a grid resolution $128 \times 64 \times 128$.

low, consistent with the rather low velocities that are observed inside the aneurysm bulge. Such a region of low (wall) shear stress is reported to be connected to aneurysm growth, associated with a slow degeneration of endothelial cells at the vessel walls. Further research in this direction is highly needed to clarify the precise mechanisms and to quantify possible growth-paths of the aneurysm.

A more precise impression of the shear stress distribution can be obtained in terms of contour plots. In Figure 3.11 we show the steady state shear stress distribution in a *yz*-plane through the middle of the aneurysm at $x = 0$. We observe a qualitative convergence of the shear stress; the degree of convergence seems to be slightly less compared to the velocity field as shown in Figure 3.9. For the shear stress we need to approximate the derivative of the velocity, which is more demanding on the spatial resolution, especially close to the aneurysm wall. The aneurysm region shows one focal point of somewhat higher shear stress near the right boundary, while elsewhere in the bulge the level of the shear stress is seen to be rather low. In addition, quite high shear stress levels are observed in the lower left corner of each contour plot, corresponding to the main flow through what remains of the original vessel structure prior to the development of the aneurysm.

3.3.3 Flow in partially filled cerebral aneurysms

With the IB method it is possible to generate various modified geometries in a relatively fast way, starting from the reference geometry. This allows to investigate consequences for the flow structure due to changes in the local vessel shape. Next to flow predictions in the initially reconstructed vascular geometry we can also simulate flow in ‘nearby’ geometries

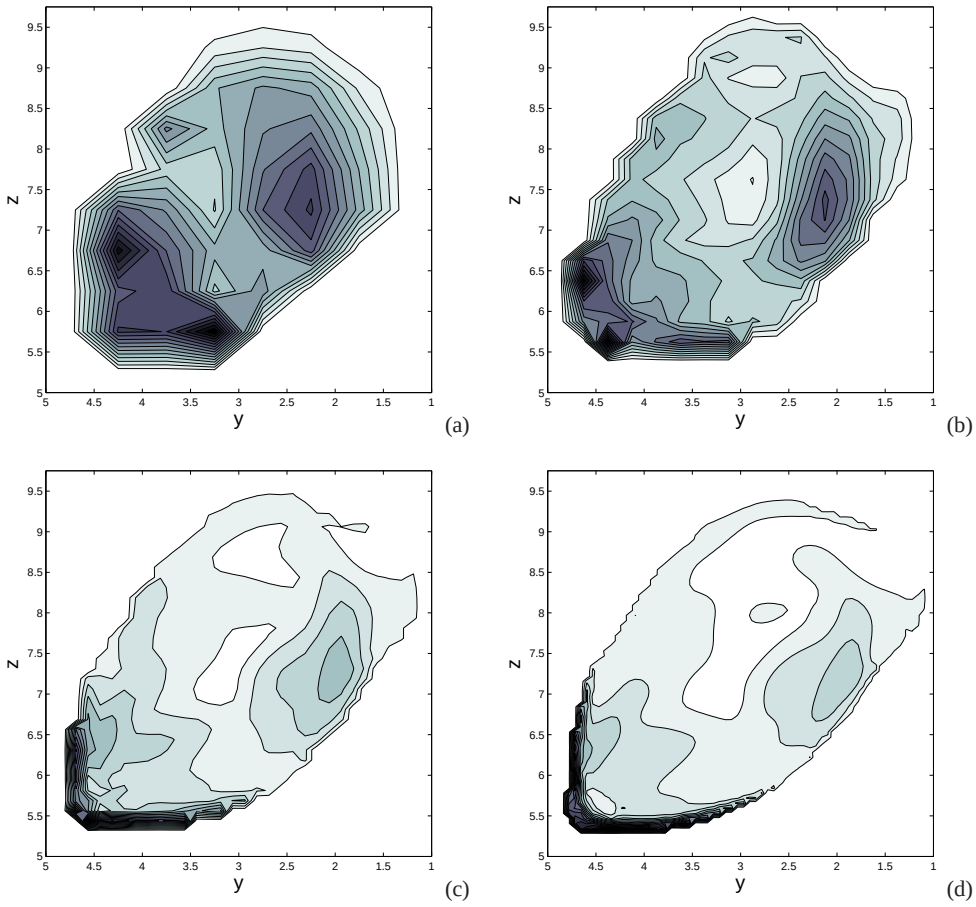

Fig. 3.11 Contour plot of shear stress τ in a yz cross-section in the middle of the geometry $x = 0$. Dark regions correspond to high levels of shear stress, while the lightest contours are related to low shear regions. We present the distribution of stress contours in the same plane for different grid resolutions: $32 \times 16 \times 32$ (a), $64 \times 32 \times 64$ (b), $128 \times 64 \times 128$ (c) and $256 \times 128 \times 256$.

representing aneurysms that are 'virtually filled' with a slender coil. Such simulations can help to understand how much coil is necessary to qualitatively change the flow structure in the affected region, aimed at reducing the flow into the aneurysm bulge to make the situation less risky. To illustrate the approach, we generated three virtual geometries which correspond to partially or fully filled aneurysms. In these geometries we compute the blood flow and observe changes in the vortical flow patterns when increasing the amount of coil in the bulge.

In Figure 3.12 we illustrate four masking functions which show possible stages during a coiling procedure. We start with the reference geometry in Figure 3.12(a) and 'coil' the aneurysm bulge in two steps (Figure 3.12(b,c)). The fully filled aneurysm is shown in Figure 3.12(d). Analyzing flow patterns we plot the velocity contours in the middle cross-section

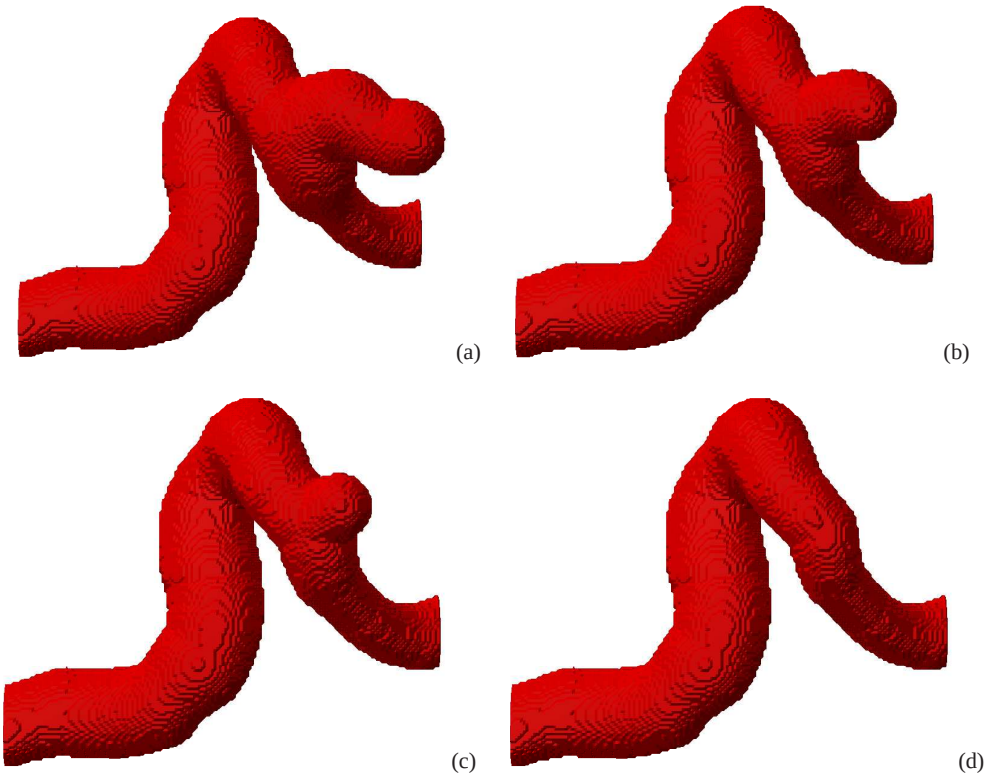

Fig. 3.12 Masking functions for partially filled aneurysms. Starting from the reference geometry (a) we can virtually fill the aneurysm with a coil and obtain the reduced shapes in (b) and (c). The fully coiled aneurysm is shown in (d).

of the aneurysm, similarly to the location chosen in Figure 3.9. We observe qualitative differences in the flow patterns when comparing the reference case and the slightly coiled geometry (Figure 3.13(a,b)) with the further coiled and the fully coiled aneurysm (Figure 3.13(c,d)). These simulations show the disappearance of the large vortical structure seen in the first two geometries - the backward flow is almost completely removed provided the amount of coil is adequate, as seen in the last two geometries. These differences in flow pattern can be relevant for decisions about the (minimal) amount of coil needed to achieve the required flow deflection.

In order to quantify more precisely the level of convergence, in the next subsection we consider the actual local solution obtained at increased spatial resolutions. For this purpose, we concentrate on the reference geometry alone as this is characteristic also for partially filled aneurysms.

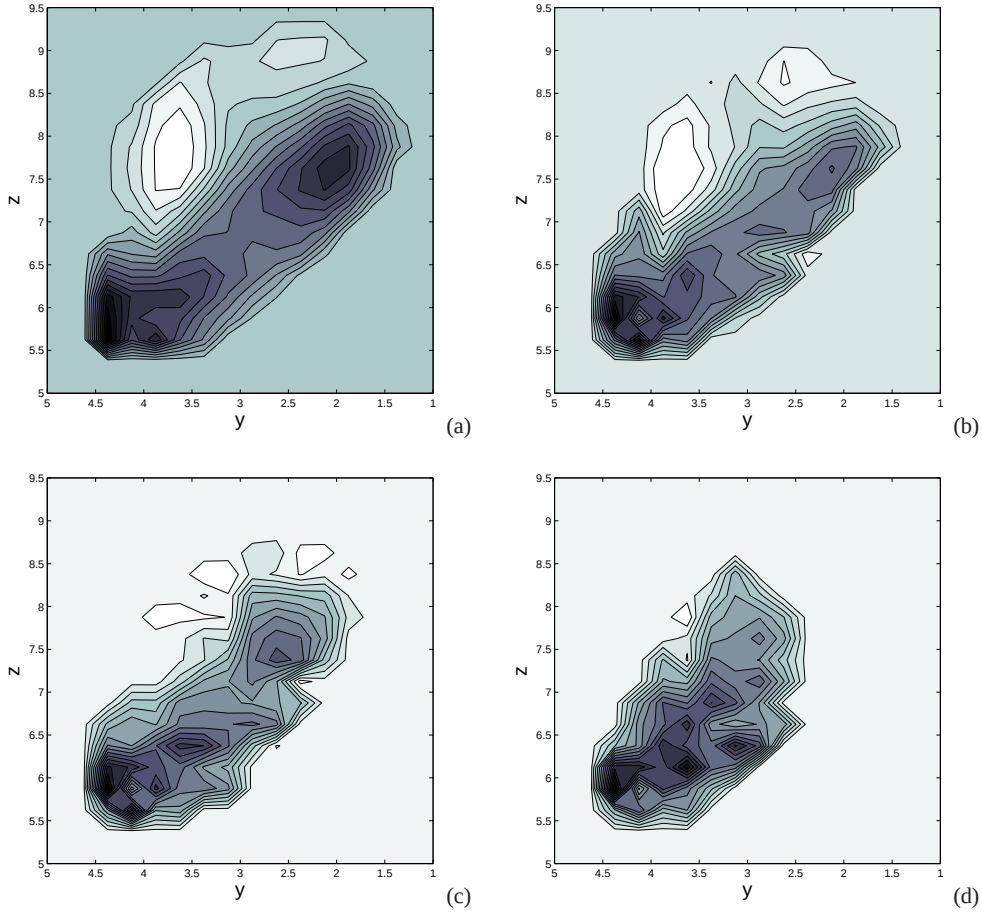

Fig. 3.13 Contour plot of the streamwise velocity in a *yz* cross-section in the middle of the geometry in partially filled aneurysms. Dark regions correspond to high positive velocities, while the lightest (white) contours are related to regions of negative velocity; we adopt the same color-coding for all figures. The flow structures show a large vortex in the reference geometry of the aneurysm (a) and in the slightly coiled aneurysm (b), while with increasing coiled volume the vortical pattern reduces considerably (c) and disappears in the fully coiled case (d) approximately restoring the original non-diseased geometry. We present the velocity contours in the same plane at grid resolution $64 \times 32 \times 64$.

3.3.4 Reliability of IB predictions: a grid refinement study

First order convergence of the volume-penalization IB method was established on the basis of laminar Poiseuille flow in a straight cylindrical tube in [61]. This confirms results obtained for the plane channel flow in case the no-slip condition is imposed within a grid cell of the solid wall [58]. The method was also tested for smoothly curved vessels with a constant circular cross-section in the previous chapter.

In this subsection we concentrate on a more quantitative analysis of the reliability of the numerical flow prediction. We consider the convergence of the driving pressure drop as well as profiles of velocity and shear stress at different grid resolutions: $256 \times 128 \times 256$, $128 \times 64 \times 128$, $64 \times 32 \times 64$ and $32 \times 16 \times 32$.

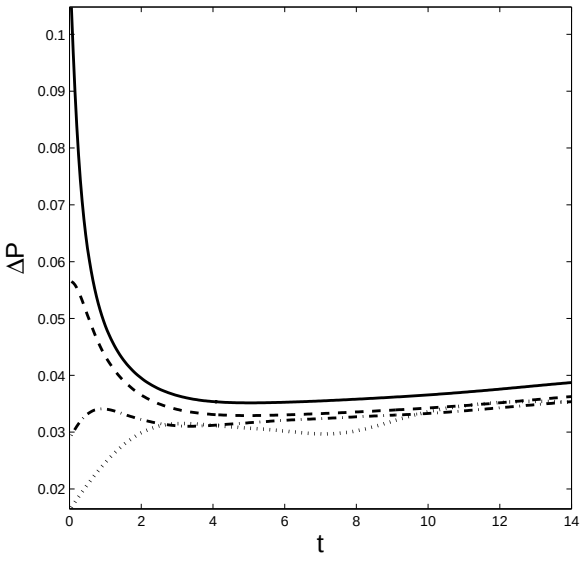

Fig. 3.14 Convergence of the pressure drop across the whole flow domain, computed at different grid resolutions: $32 \times 16 \times 32$ (dot), $64 \times 32 \times 64$ (dash-dot), $128 \times 64 \times 128$ (dash) and $256 \times 128 \times 256$ (solid).

In order to maintain a constant mass flow rate through the aneurysm, a pressure drop ΔP needs to be supplied. In Figure 3.14 we show the evolution of the forcing pressure drop at different spatial resolutions. The initial solution from which each simulation starts uses $u = 1$ and $v = w = p = 0$. Hence, we deliberately set the streamwise velocity equal to unity everywhere, i.e., also inside the solid part of the domain. This presents a strict test for the robustness of the method, in which the solution has to adapt and reduce completely to zero within the solid and a realistic flow in the fluid part needs to build up. There is considerable difference between the solution at different spatial resolutions in the initial stage due to the strong acceleration of the flow to rectify the non-physical aspects of the initial condition. As the flow settles into the steady state we notice a convergence in time of the pressure drop levels. Since the non-dimensional size of the domain is 16 and the velocity is maximally around 0.7, a typical flow-through time, i.e., the time needed to pass from one side of the domain to the other, can be expected to be in the range of 20 or more. To reach a fully steady state, a simulation covering several flow-through times is needed. In Figure 3.14 we notice close agreement for ΔP at different spatial resolutions already after about half a flow-through time.

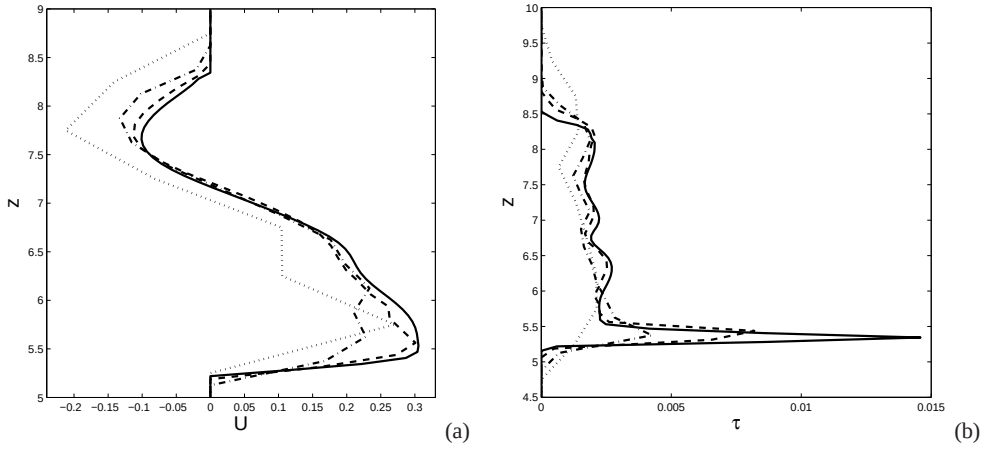

Fig. 3.15 Streamwise velocity (a) and shear stress (b) profiles as a function of z, in the middle of the domain at $x = 0$ and $y = 4$. The profiles were computed at $t = 14$ using different grid resolutions: $32 \times 16 \times 32$ (dot), $64 \times 32 \times 64$ (dash-dot), $128 \times 64 \times 128$ (dash) and $256 \times 128 \times 256$ (solid).

To further assess the reliability of the solution we turn to profiles of velocity and shear stress in a characteristic region in Figure 3.15. This provides a more quantitative measure for the convergence of the numerical solution. We observe that at the coarsest resolution of $32 \times 16 \times 32$ we cannot capture more than the main flow pattern of recirculating flow. In fact, there are only 6 grid cells per vessel cross-section at this resolution. For grid resolution $64 \times 32 \times 64$ already 13 cells are fluid and further increasing of the grid resolution gives 25 and about 50 points per cross-section of the vessel. These latter three values correspond to resolutions used in [58] at which asymptotic first-order convergence was observed for Poiseuille flow. Thus, increasing the resolution allows a much closer correspondence between the different velocity predictions. This is also seen in the profiles for the shear stress. The general agreement is quite close, as long as we do not include the coarsest resolution. Convergence of the sharp stress peak near the lower wall in this particular profile is seen to be most challenging to our IB method. We also investigated convergence by considering profiles in a various other locations and observed similarly close agreement of the numerical solution. This establishes that a first quantitatively acceptable solution can be obtained using a grid of $64 \times 32 \times 64$, while higher accuracy requires further refinement.

In the next section we will discuss how sensitive the numerical results are to the different choices regarding the selection of the vessel segment for the flow simulation ('cutting') and the extension to a periodic flow model ('connecting').

3.4 Sensitivity of flow predictions to elementary operations on masking function

We described the process of constructing a basic model for the simulation of flow in the reference aneurysm geometry, starting from the simplified data presented in Figure 3.3(b). The chosen reference geometry was illustrated in Figure 3.7(a). In this section we analyze the effect of cutting and connecting for this geometry by considering the sensitivity of predictions in the alternative geometries in Figure 3.7(b) and (c) relative to the reference geometry in Figure 3.7(a). In a few questions we can describe the sensitivity analysis as follows. What would be the influence on the flow predictions if we cut the initial geometry at a different location? How important is the smoothness of the connector needed to obtain a periodic flow model? Answers to these questions are obtained by computing the flow explicitly and comparing the results for velocity profiles and pressure difference.

We simulate steady flow at $Re = 250$. Based on the convergence analysis in Subsection 3.3.4 for the reference geometry, we consider only one grid resolution $128 \times 64 \times 128$ for the sensitivity analysis. We first present the results for the pressure difference to obtain a general impression about the global convergence. Subsequently, we will illustrate velocity profiles and assess the relative differences between flow computed in the reference geometry and the flow computed in the other geometries.

In Figure 3.16(a) the pressure difference as a function of time is plotted. For flow computed in the 'short' geometry, the pressure difference is lowest, as it is easier to flow through it relative to the long geometries in view of the straightness of the connector. Comparing the two long geometries we observe that the type of connector is shown to be quite irrelevant. Further, in Figure 3.16(b) we analyze the averaged pressure per cross-section along the aneurysm geometries at time $t = 20$. We plot the domain such that the center part of the geometry containing the aneurysm bulge is located around $x = 0$. The aneurysm indicator is included at the bottom of the figure to show the parts of the original geometry and the interpolated connector(s) in every case. In the part of the geometry containing the aneurysm all simulations give virtually identical results, with some deviations near the regions where the original geometry is connected to a numerically interpolated segment. Further, we observe the very small differences when comparing different types of connectors for the long geometry. At physiologically relevant flow conditions it appears that manipulating the geometry by cutting at different locations and connection in different ways, has small effects which in addition remain spatially well localized.

To evaluate consequences of the differences in the definition of the flow domain on the flow profiles we show the streamwise velocity component at several locations along the x axis for all geometries (Figure 3.17). At every x location we choose the y coordinate such that the velocity profile as function of the vertical coordinate z is taken through the 'middle' of the cross-section. One dimensional profiles of the velocity components can be obtained

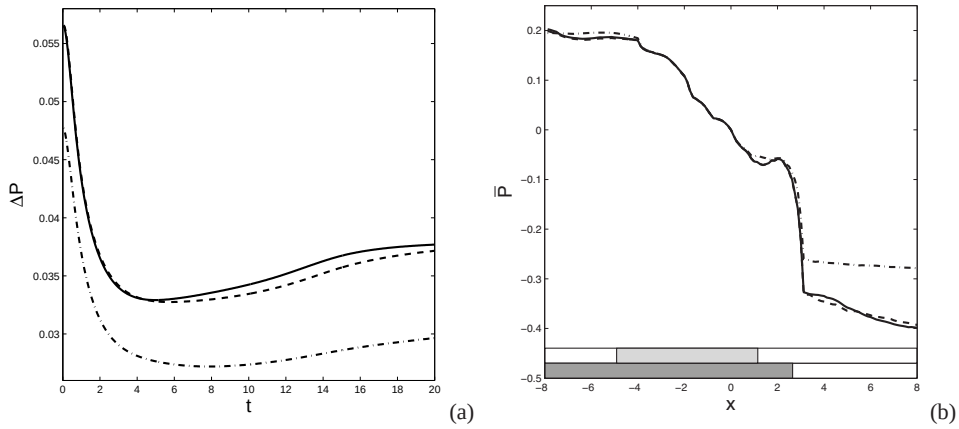

Fig. 3.16 Pressure difference across the aneurysm geometries (a) is shown as a function of time for the reference geometry (solid), long geometry with linear connector (dash) and short geometry with smooth connector (dash-dot). The general level of the pressure difference for the short geometry is lower, corresponding to an easier flow through the smooth, rather straight connector, compared to flow through the curved original vessel segment. The pressure $\overline{P}$ averaged over y and z is shown as function of x in (b) at $t = 20$. Included is the schematic indicator introduced in Figure 3.7 to view original vessel tract (gray) and connector vessel (white) for the long (dark gray) and short (light gray) geometries. Simulations are at $Re = 250$ for grid resolution $128 \times 64 \times 128$.

along this particular *xy* locus. The aneurysm indicator is included as well, allowing to better interpret differences and similarities. We observe close correspondence in the middle part of the computational domain, which contains the aneurysm bulge. For the long geometries the differences in the connector, 'downstream' of the bulge, also induce small differences in the velocity profile 'upstream' of the bulge, in view of the periodic boundary conditions. The connector of the short geometry is located slightly higher than the connectors for the long geometries, which is clearly seen from the velocity profiles. Comparing the velocity in the short geometry with that in the longer ones, we observe virtually identical velocity profiles in almost the entire part of the computational domain that is shared among these geometries, consisting of the original vasculature. Near the edges of the retained segment of the vessel, i.e, near the two cut locations $x \approx -5$ and $x \approx 1$ we observe that differences in the velocity disappear or build-up, respectively, over about one non-dimensional unit downstream of that location.

Differences and similarities in the streamwise velocity solutions can be observed more closely by 'zooming'. In Figure 3.18 profiles are presented at 16 locations. Numbers in the top right corner of every sub-plot show the x coordinate at which the profile was taken. We appear to have only one profile at $x = -2, -1, 0$, which means that all profiles are virtually identical. At $x = -3, 1$ the differences are visible but still small, while at other x values the profiles differ more, as they are computed in physically different geometries. The 'reliable'

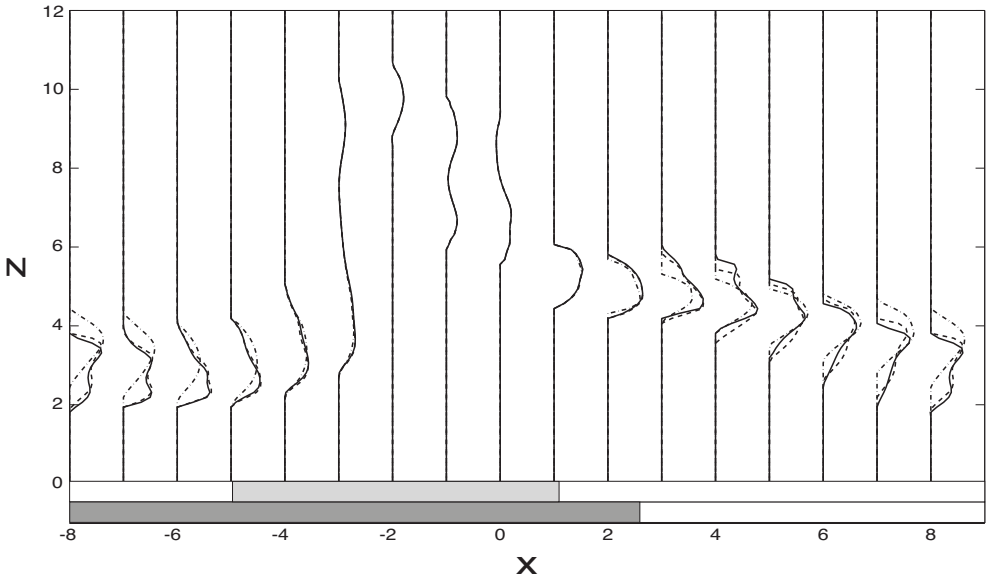

Fig. 3.17 Streamwise velocity profiles at several locations along the aneurysm geometry, shown as function of z and taken at a y location indicating the middle of the vessel at the chosen x location for all three geometries: reference geometry (Figure 3.7(a); solid), long geometry with linear connector (Figure 3.7(b); dash) and short original geometry (Figure 3.7(c); dot). Simulations are at $Re = 250$ for grid resolution $128 \times 64 \times 128$.

segment $[-3, 1]$ corresponds to the overlapping 'original' segment of the vessel among the three geometries, minus a part of about unit length near the inflow of this section with the bulge, as mentioned also above.

Finally, we analyze the sensitivity in a quantitative way by computing the relative difference δ between streamwise velocity profiles in the L_2 norm, normalized by the maximal streamwise velocity in the entire domain. The results for this relative deviation computed at the same 16 locations at which velocity profiles were presented, are shown in Figure 3.19. In the middle of the computational domain the differences in flow predictions obtained in the reference and the alternative geometries are very small, while outside the original part of the vessel somewhat higher levels of deviation are present. Turning to the comparison for the short cut geometry, we notice maximal deviations on the order of 20 % in regions where the quite different connectors are concerned, which rapidly reaches levels as low as 10^{-4} in the relevant bulge region. The comparison of the long cut geometries is more favorable. The maximal deviations reach about 10 % toward the end of the domain. These deviations reduce to about 2 % in the segment upstream of the most striking bulge formation and reduce to levels as low as 10^{-5} in the actual bulge.

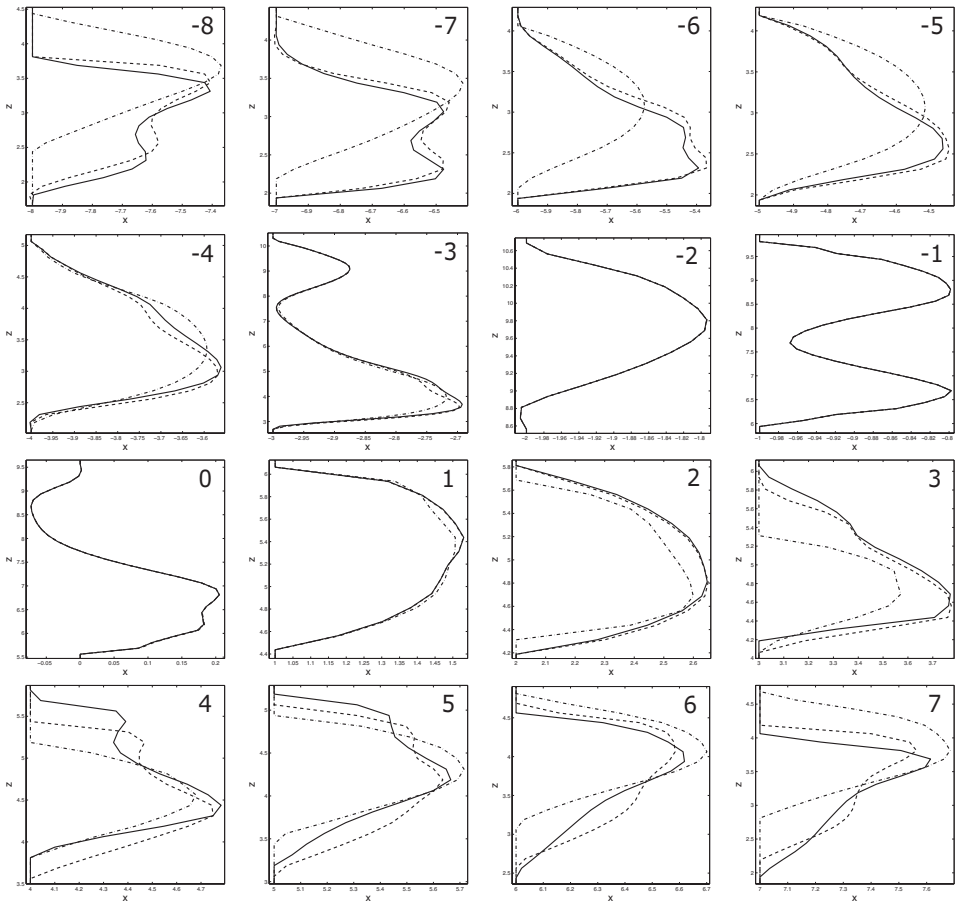

Fig. 3.18 Streamwise velocity profiles at 16 (x,y) locations along the aneurysm geometries for the reference (solid), the long geometry with linear connector (dash) and the short geometry (dash-dot). The number in the top right corner of every figure corresponds to the x location at which the profile was taken. Simulations are at $Re = 250$ for grid resolution $128 \times 64 \times 128$.

3.5 Sensitivity of flow predictions in bounding geometries

In this section we discuss bounding geometries, which are used to quantify the sensitivity of predictions for key flow properties to the quality of medical imagery and spatial resolution, particularly the cross-sectional sizes. We first describe the construction of bounding masking functions at different grid resolutions. These are masking functions that correspond to slightly larger or slightly smaller fluid domains, thereby mimicking the uncertainty in the precise domain definition due to the available accuracy in the raw medical imagery stemming from the voxel size and/or slight motions of the tissue-vessel interface during recording. Subsequently, we will use these bounding geometries to assess the reliability of the numerical solution by

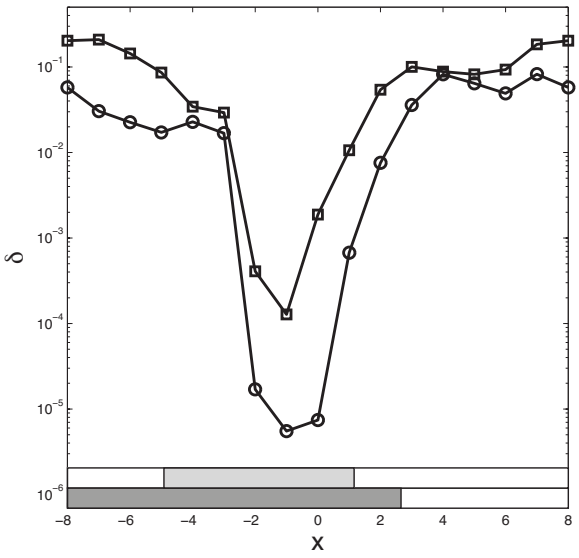

Fig. 3.19 The relative differences between streamwise velocity profiles comparing the reference geometry with the long geometry with linear connector (solid ○) and the reference geometry with the short geometry (solid □).

showing velocity profiles and the pressure difference across the geometry. Throughout, we illustrate our findings with simulations of flow in the reference geometry.

3.5.1 Grid coarsening and bounding geometries

In Subsection 3.2.1 a brief introduction into bounding geometries was given. Here we will discuss in some detail how the masking function associated with bounding geometries can be extracted, while coarsening the grid.

Analyzing the convergence of the IB method (Subsection 3.3.4) we computed flow at different grid resolutions and considered only basic geometries. In this subsection we will also consider bounding geometries, which can be generated on every level of grid coarsening. Thus, from $256 \times 128 \times 256$ we generate bounding geometries on $128 \times 64 \times 128$, $64 \times 32 \times 64$ and $32 \times 16 \times 32$. From these geometries we not only extract convergence but also practical bounding properties for pressure drop, velocities and stresses.

When coarsening the grid by a factor of 2 in every direction, the grid cells of the coarser grid contain 8 grid cells from the finer resolution. This implies also that the center of the coarser grid cell is at the intersection of corner points of 8 finer grid cells which allows some freedom in the way in which the masking function should be coarsened. The ‘basic’ strategy

assigns to the whole cell a value to the masking function which is determined by the property ‘solid’ or ‘fluid’ in the center of the grid cell. However, when coarsening the grid the value of the masking function in the center of the coarsened cell is not uniquely defined. We choose to obtain it from the average value taken from the 8 neighboring cells of the finer grid that are contained in one cell of the coarser grid. We compute the average value of the masking function and obtain a value between 0 and 1. Then we apply a simple rule: if the average value is equal to or more than a threshold value of 0.5 we call the coarser cell solid and give it the value ‘1’, otherwise the cell is fluid and the corresponding coarsened masking function is set to ‘0’ at the location. In this way we generate the so-called coarsened ‘basic’ geometry. Repeating this construction for each coarsening by a factor of two, yields a set of coarsened masking functions associated with the basic geometry.

We can readily extend this ‘basic’ construction and define masking functions for slightly larger or slightly smaller geometries, We may apply the ‘basic’ coarsening rule also to the 8 corner points of a cell in the coarsened grid. These corner points are also at the center of 8 fine-grid cells and we may determine the average masking function and find whether the average is equal to or more than 0.5. Having defined for each coarse grid cell the value of the masking function in its 8 corner points we may apply the method sketched in Subsection 3.2.1 and arrive at eight bounding geometries.

We may assess the influence of redefining the masking function in terms of the number of fluid cells for every geometry. This is collected in Table 3.1. Bounding geometries are numbered #1-#8 corresponding to the number of solid corner points needed to define the grid cell ‘solid’, which is the criterion for bounding strategies as discussed in Subsection 3.2.1. In particular, #1 contains the largest number of solid cells and #8 the largest number of fluid cells. We find that the basic geometry contains more fluid cells than geometries #1-#4 and less than geometries #5-#8.

Grid resolution	#1	#2	#3	#4	basic	#5	#6	#7	#8
$128 \times 64 \times 128$	42134	44277	46828	49052	50844	52068	54533	57346	60058
$64 \times 32 \times 64$	4060	4513	5050	5564	6052	6317	6915	7646	8343
$32 \times 16 \times 32$	262	331	428	523	670	709	861	1038	1232

Table 3.1 Number of fluid grid cells in the generated geometries at a resolution of $128 \times 64 \times 128$, $64 \times 32 \times 64$ and $32 \times 16 \times 32$ with, respectively, 1048576, 131072 and 16384 grid cells. We include 8 bounding and 1 basic geometry at three grid resolutions where #*i* denotes the masking function obtained with the rule that a grid cell is solid in case *i* of its corner points are solid.

Bounding geometries were already presented in [61], where numerical solutions in a cylindrical tube were compared to the analytical Poiseuille profile. In that case only three geometries were considered: ‘basic’, ‘inner’ (#2) and ‘outer’ (#6). The basic solution was found to

be bounded by the parabolic profiles obtained from the 'inner' and 'outer' geometries at all grid resolutions. With increasing grid resolution all profiles converge to the exact solution.

For the realistic aneurysm geometry we are interested in the bounding solutions, as they give a quantification of the sensitivity of predictions, based on uncertainties in the initial geometry. By using bounding geometries we may assess a range of numerical predictions instead of only one. We present the numerical solutions in the next subsection.

3.5.2 Numerical bounding solutions

To illustrate bounding geometries we compute the flow at $Re = 250$ in all 9 geometries at grid resolutions $128 \times 64 \times 128$ and $64 \times 32 \times 64$. We look into a streamwise velocity profile in the middle of the aneurysm to obtain a local measure of sensitivity and also include the evolution of the pressure differences for every geometry to consider a global characteristic. In Figure 3.20 the solution for the basic geometry is plotted as a solid line, while the 8 other solutions corresponding to bounding geometries are shown dashed and dash-dotted according to whether we consider a slightly smaller ('inner') or slightly larger ('outer') volume for the flow domain, respectively. We observe that the pressure difference of the basic solution is bounded by the other solutions from above and below. At both grid resolutions, the pressure drop of the outer solutions (dash-dot), obtained by bounding the volume of the flow domain from above, are shown to be closer to each other than the inner solutions (dash), obtained by bounding the volume of the flow domain from below. The pressure drop for the inner solutions shows more sensitivity to geometry variation than for the outer solutions, which might be related to the relatively small number of grid points per vessel opening ($6-10$ for the coarser resolution in Figure 3.20(a) and $12-20$ in Figure 3.20(c)). If the variation in the bounding geometry relative to the basic geometry is too large then the usefulness of the bounding solutions is rather limited. Hence, for coarse grids only geometries that are sufficiently close to the basic geometry should be included in a sensitivity analysis. The velocity profiles show a similar behavior: for the $128 \times 64 \times 128$ grid in Figure 3.20(d) the 'bounding band' is relatively narrow, closely following the basic solution, while for the $64 \times 32 \times 64$ grid some of the inner solutions are at marginal spatial resolution, leading to physically wrong solutions. For very small (inner) geometries, the sensitivity to the choice of masking function is high if only a few grid cells are available to cover each velocity profile. Grey bands of bounding solutions for the pressure difference show the most narrow bounding, associated with strategy #4 and #5 in Table 3.1. For the velocity profiles the variation in the numerical solution due to variations in the flow domain also indicate the degree of sensitivity. However, for the velocity there is no uniform 'lower' or 'upper' profile that would bound everywhere the basic solution; in some parts of the domain the velocity based on a certain perturbed masking function may

be slightly larger than that obtained with the basic masking function, while it is slightly lower elsewhere to maintain the same overall flow rate.

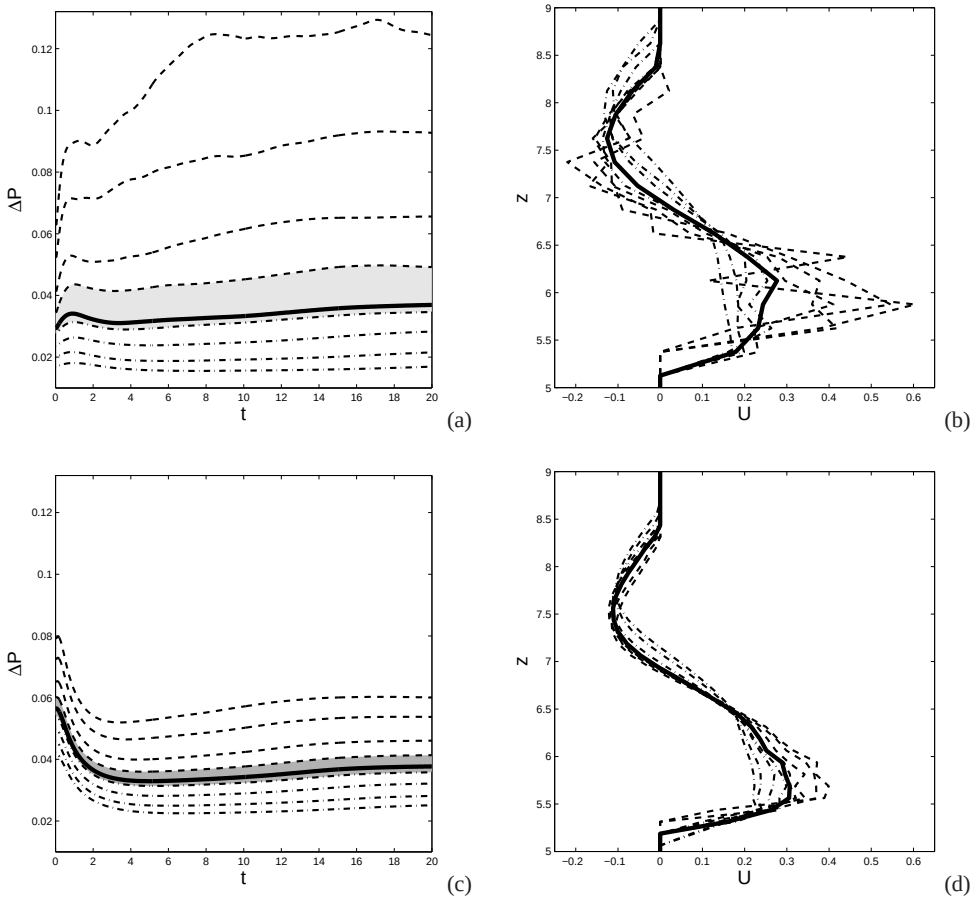

Fig. 3.20 Pressure difference (a,c) and streamwise velocity profiles in the middle of the aneurysm (b,d), computed at grid resolutions $128 \times 64 \times 128$ (c,d) and $64 \times 32 \times 64$ (a,b) in basic (solid) and bounding geometries for inner geometries approximating the volume of the fluid domain from below (dash) and outer geometries approximating the volume of the fluid domain from above (dash-dot). Two grey bands in (a) and (c) show the variability in the pressure difference associated with minimal variation in the bounding fluid domain.

The bounding solutions can be used for another practical purpose, i.e., we may predict reliable bounds on flow properties at much reduced computational time. While coarsening the grid resolution, every coarser domain contains 8 times fewer grid cells. For our numerical method this implies that flow will be computed about 16 times faster, taking into account an increase in the time-step with which the solution is computed. Thus, instead of simulating the flow in the basic geometry at higher grid resolution, we can work with two bounding ge-

ometries at a lower grid resolution. We analyze this approach for 'couples' of grid resolution $256 \times 128 \times 256$ and $128 \times 64 \times 128$, which will be 8 times faster taking into account that we would like to compute two bounding solutions. Another 'couple' of grid resolutions is $256 \times 128 \times 256$ and $64 \times 32 \times 64$, which would imply a reduction of computational time by a factor of 128.

In Figure 3.21 we illustrate the pressure difference computed for the basic geometry at grid resolution $256 \times 128 \times 256$ (solid) bounded by inner and outer solutions for strategies #4 and #5 (see Table 3.1) computed at resolution $128 \times 64 \times 128$ (dash lines; dark gray band) and at resolution $64 \times 32 \times 64$ (dash-dot lines; light grey band). In Figure 3.21(a) we observe no bounding up to time $\approx t = 3-4$, caused by the initial conditions ($u = 1$ and $v = w = 0$) which does not correspond to the physical flow and needs some time to adapt. After $t = 4$ we illustrate the bounding solutions in more detail in Figure 3.21(b). Coarsening the grid by a factor of 2 in each direction allows to compute the band of possible solutions with a relative variability of $10-12\%$, when coarsening by factor 4 in each direction the variability increases to about 30%. Depending on the required level of accuracy, one can choose one of the following options: expensive computations for the basic solution at high resolution, faster computation of a tight bounding band with relative variability $10-12\%$ at $2^4/2 = 8$ times reduced computing time, or very fast computed wider bands with relative variability about 30% and a reduction in computing time by a factor of $4^4/2 = 128$. Clinical practice needs to be incorporated to guide sensible choices for a bounding strategy.

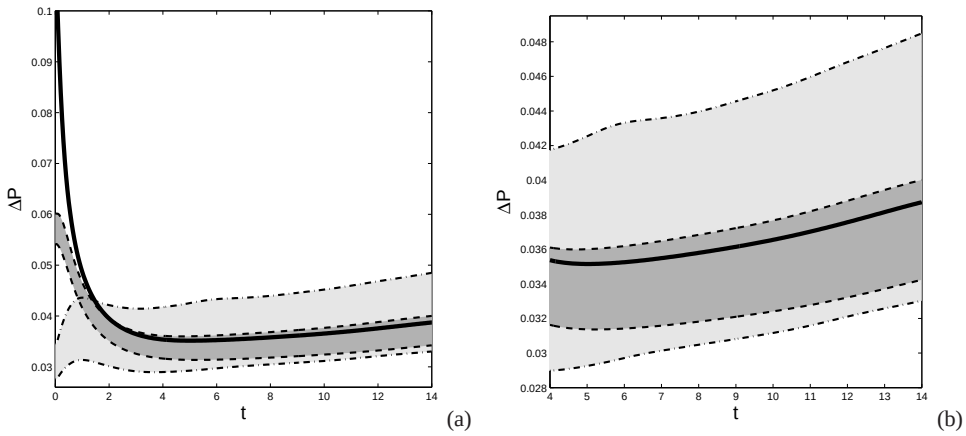

Fig. 3.21 Pressure difference for the basic geometry (a) at grid resolution $256 \times 128 \times 256$ (solid) with the bounding solutions #4 (highest ΔP) and #5 (lowest ΔP) at lower grid resolutions: $128 \times 64 \times 128$ (dash) and $64 \times 32 \times 64$ (dash-dot). In a zoomed-in plot shown in (b) the width of each bounding band can be easier assessed.

3.6 Concluding remarks

We presented a computational model for simulation of blood flow inside cerebral aneurysms that may form in the Circle of Willis. The medical interest is in understanding the flow and forces that emerge in aneurysms and their relation to stabilizing or inversely to possible rupture of cerebral aneurysms. We illustrated the modeling process starting from medical imagery of a realistic cerebral aneurysm, which was used as a case study in this chapter. We concentrated on steady flow simulations and analyzed the sensitivity of the predicted blood flow inside the aneurysm to the various modeling steps. We also showed convergence of the numerical solution and illustrated the method of bounding geometries.

Taking data from literature we identified physiologically relevant flow conditions and their general uncertainty. Data concerning sizes of vessels, kinematic viscosity of blood and flow speeds in the region of the Circle of Willis are patient-specific and can not be obtained with very high accuracy. This leaves considerable uncertainty as to the precise flow conditions. For healthy conditions, the computed range of values for Reynolds number, which is the crucial parameter for incompressible flow, is $175 \leq Re \leq 300$. This range suggests laminar flow. However, in case of diseased vessels or if the blood properties are not standard, Re can be much smaller or much higher, which will lead to noticeable changes in flow patterns to which we will return in the next Chapter.

Settling for $Re = 250$ as characteristic point of reference, we analyzed a particular, realistic cerebral aneurysm in detail. First, we considered the main flow features and the reliability of predictions for steady flow at fixed volumetric flow rate. This is not a realistic flow condition, as in reality interest is with pulsatile flow, but it does allow to investigate the sensitivity of the predicted solution on things such as spatial resolution. We visualized both qualitatively and quantitatively the steady flow in the aneurysm, as well as the shear stress field that emerges. It was shown that the main flow follows a path that is close to what used to be the original vessel before the formation of the aneurysm. Next to this ‘main’ flow, a complex circulation was shown to develop inside the aneurysm bulge. We also illustrated the influence of partial filling of the aneurysm bulge on the flow pattern that develops inside. This type of simulations can support coiling procedures in taking a decision about the amount of coil that is required to change the flow sufficiently to remove the problem for the patient. By considering contour plots and also profiles of velocity and shear stress at different spatial resolutions, the degree of convergence of the numerical simulation was discussed. The current IB method is first order accurate. Developments in which sub-grid forcing is included [79] can be used to increase the formal order of accuracy to two - this appears a relevant extension of the IB approach and will be considered in more detail in the near future, allowing to cut down on the computational cost and/or increase the accuracy of flow predictions.

The influence of the modeling steps on the predicted flow inside the aneurysm was analyzed and compared for three different geometries. It was shown that inside the aneurysm

bulge flow stays virtually the same in all geometries, while small differences occur in the connecting parts. This test allows to conclude that under physiologically realistic conditions the precise selection of the vessel segment and the formulation of a flow model with periodic boundary conditions do not have a strong influence on the computed flow characteristics. Moreover, the influence was found to remain very localized so that 'downstream' effects remain small. Thus, if the connecting part of the vessel is far enough from the aneurysm bulge, there is no appreciable effect on the flow patterns inside the aneurysm bulge. Bounding solutions were presented and shown to be a practical tool for fast assessment of the general flow patterns. This method can be used to provide the to be expected range of possible solutions due to uncertainties in the geometry definition before considering to compute the precise flow at high resolution.

In this chapter we focussed on steady flow. To arrive at a first complete simulation model it is essential to incorporate the pulsatile effect of blood flow and investigate the dynamical consequences of this time-dependent forcing. This is the subject of the next chapter

Chapter 4
Transition of pulsatile flow in cerebral aneurysms

Abstract

In this chapter we adopt a volume penalizing immersed boundary method for the simulation of pulsatile blood flow inside cerebral aneurysms. We show that the flow undergoes a transition from an orderly state at low physiological Reynolds numbers, in which the pulsatile forcing is closely followed in time, to a complex response with strongly increased high-frequency components at higher physiological Reynolds numbers, i.e., at higher flow rates and larger aneurysm sizes. The flow is computed by solving the Navier-Stokes equations for incompressible flow. Geometric complexity of aneurysms in the cerebrovascular system is captured by defining the fluid and solid domains using a so-called binary 'masking function', which is a key element in the immersed boundary method. The pulsatile variation of the flow rate is represented in terms of measured cross-sectionally averaged velocities in the vicinity of the aneurysm, obtained by noninvasive Transcranial Doppler sonography. Transition of the flow is found to arise in qualitatively the same way at all locations near the aneurysm bulge quite independent of the solution component that is monitored. The numerical reliability of the predicted transition is quantified on the basis of practical upper and lower bounding solutions, expressing the sensitivity of the flow to uncertainties in the aneurysm geometry. We compute the spectrum of the response of the flow at various locations and flow conditions and quantify the transition in streamwise velocity. The significant increase of small-scale, high-frequency structures at higher Reynolds numbers may have potential for clinical screening application in the future.

4.1 Introduction

Prediction of blood flow inside cerebral aneurysms is a field of intensive research, aimed at supporting medical decisions about possible treatment strategies [48, 103]. The cerebrovas-

cular system has a complex geometrical structure, which varies from one person to another. Also the properties of the blood flow, such as flow rate, viscosity and the actual profile of the heart beat are patient-specific characteristics. These days medical imaging techniques such as 3D rotational angiography (3DRA) can be used for diagnostic purposes, to visualize the vascular structure of the human brain. Likewise, the actual pulsatile volumetric flow rate can be measured in a non-invasive way using a Transcranial Doppler (TCD) Sonography technique, which allows to record the time-dependent cross-sectionally averaged velocity in a chosen cerebral artery near the aneurysm. Combining these two sources of medical data - geometry and pulsatile wave - we can develop new computational fluid dynamics (CFD) methods to actually compute the detailed blood flow on a patient-specific basis and ultimately try to understand hemodynamic aspects of slow aneurysm growth and developing risk of rupture.

In this chapter we continue the development of a computational model for the flow of blood by adding the element of pulsatile forcing. The model is based on a finite volume discretization of the Navier-Stokes equations, while the geometry is represented using an immersed boundary (IB) method. The pulsatile wave is imposed as a forcing to the flow rate in the computational domain. With this new complete model it is possible to observe and analyze the detailed flow. By changing the flow conditions within the physiologically realistic range, we observe a striking transition from relatively smooth and regular flow that closely follows the pulsatile forcing profile to highly complex erratic time-dependence that appears much less connected to the regular forcing. To illustrate this transition we simulate the blood flow under different Reynolds numbers. This yields dynamic behavior ranging from smooth flow that closely follows the pulsatile forcing profile at the lower Reynolds range to very complex flow at the higher Reynolds range that appears much less connected to the regular forcing and displays significantly more contributions from high frequencies. These might be an indication of an increased size of the aneurysm, or more vigorous flow. The strong transition that we observed was also reported earlier in clinical settings [23, 49], and may be of medical use in rapid first monitoring of patients. In this chapter we will illustrate this transition process for one particular patient's aneurysm geometry. We also considered other typical cerebral aneurysm geometries for which a similar transition was found in the same Reynolds range.

Numerous studies involving computational modeling of cerebral aneurysms have been developed over the past decade [5, 9, 16, 24, 87]. The development process of numerical methods for simulation of blood flow typically goes through a number of stages: investigation of model geometries, computation of model flow, inclusion of realistic geometries and simulation of full-scale realistic flow yielding patient-specific results. Modeling steps are necessary to validate the method in order to be able to apply it reliably to the realistic setting. For simulating pulsatile flow one may start with validation based on periodic sinusoidal forcing of the flow rate or other simplified forcing profiles [36, 92, 98]. Once the temporal accuracy is assessed one may continue by imposing recorded volumetric flow rates per heart beat as inflow

to the system [3, 56, 91]. The development of the IB method used in this chapter for capturing flow in cerebral aneurysms also went through these stages [59, 60]. We validated our method for Poiseuille type of flow and applied it to model geometries in Chapter 2. Subsequently, we arrived at a patient-specific aneurysm geometry for which steady flow was investigated in Chapter 3. In this chapter we complete the development of a first sequence of modeling steps by incorporating realistic pulsatile flow in realistic cerebral aneurysm geometries. We investigate the dynamic response of the flow in the aneurysm neighborhood and aneurysm bulge, for a range of physiologically relevant conditions.

We simulate pulsatile flow for different flow regimes, which are specified by the Reynolds number. It is well known that for small Reynolds number, flow is laminar and smooth, and with the increase of the Reynolds number flow may undergo transition to become unsteady with several smaller scale vortices. Further increase in the Reynolds number often leads to turbulent flow [27]. A typical Reynolds number based on the radius of a cerebral vessel in the Circle of Willis is around 250. Due to uncertainty in various parameters a physiologically relevant range $Re = 100 - 400$ can be defended [23, 24, 82]. Under steady boundary conditions, this range corresponds to smooth laminar flow. However, under unsteady boundary conditions, at the higher end of the Reynolds range rapid variations of the solution in time, sometimes wrongly referred to as 'turbulent' effects [4, 23] were observed. In such flow conditions, diseased vessels support flows with rapid fluctuations, which could be detected via non-invasive techniques. These so-called brain 'bruits' can be recorded and the spectrum of frequencies can give some characterization of the shape and size of the aneurysm, as well as of the dominant flow regime [45, 49].

Simulating flow on the basis of an IB method allows to go from medical imagery to quantitative flow predictions. We compute pulsatile flow inside and near a cerebral aneurysm and show that already at physiologically relevant flow conditions complex dynamics occurs. Quantitatively the level of shear stresses that is found numerically corresponds to values known from medical practice, thereby providing additional validation for the computations. With changing flow condition through increasing Reynolds number we observe transition in all sorts of quantities such as velocity components, numerical pressure and shear stresses at various locations inside the vessels and aneurysm bulge. While analyzing the spectrum of the resulting numerical solution, the complex and more intense dynamics of higher Reynolds flows can be clearly observed.

The organization of this chapter is as follows. In Section 4.2 we present the computational model for pulsatile blood flow simulations inside cerebral vessels. We first introduce the numerical method and aneurysm geometry, obtained from medical data. Then, we describe the pulsatile wave, measured in an artery of the Circle of Willis and discuss the range of realistic parameters for cerebral blood flow. Subsequently, we illustrate the solution computed in the selected geometry under reference pulsatile flow conditions at $Re = 250$. In Section 4.3 we present results computed at different flow regimes and illustrate the transition arising in

all quantities and at various locations inside the vessel and the aneurysm. We discuss the robustness of the transition phenomenon subject to uncertainties in the geometry definition by computing upper and lower bounding solutions. Finally, we perform a Fourier analysis of the pulsatile flow computed in different flow regimes. Concluding remarks are in Section 4.4.

4.2 Computational model of cerebral pulsatile blood flow

In this section we present the computational model for simulating blood flow inside cerebral vessels and aneurysms. We first discuss the Navier-Stokes equations and introduce the IB method, which allows to capture flow in complex domains. We illustrate this for a realistic aneurysm geometry, reconstructed from medical data in Subsection 4.2.1. Later, in Subsection 4.2.2, we concentrate on physiological aspects of cerebral blood flow and specify the pulsatile forcing, extracted from TCD measurements. We also motivate the choice of flow parameters that characterize physiological conditions as used in the simulations. In Subsection 4.2.3 we present the computed velocities at different locations along the aneurysm geometry and also analyze flow at different stages of pulsatile heart beat.

4.2.1 Immersed Boundary method and aneurysm geometry

Modeling of blood flow in a human body can be performed in different ways depending on the particular flow regime that is relevant to the medical problem. A broad overview of models of the cardiovascular system is presented in [76]. Blood flow can be considered on the macroscopic scale - the level of fluid patterns, as well as on much smaller microscopic scales - blood cells and their bio-chemical transport processes. A first decision that is required when developing a model is whether or not to approximate blood as a Newtonian or a non-Newtonian fluid [6, 14, 24, 28, 38]. For cerebral flows taking into account physiological flow conditions and sizes of arteries the non-Newtonian corrections were found to be quite small [15, 28, 38, 71]. Flow patterns were found to be qualitatively the same, while local values of velocities and pressures were found to differ by less than 20%.

In our numerical model blood is treated as an incompressible Newtonian fluid, for which the Navier-Stokes equations in 3D provide the conservation of mass and momentum. The total physical domain Ω, consists of a fluid part Ω_f that corresponds to the vessels containing the blood, and a solid part Ω_s that contains the soft tissue material. The no-slip condition is applied at the interface between fluid and solid parts in Ω. In non-dimensional form the governing equations are given by:

$$\frac{\partial \mathbf{u}}{\partial t} + \mathbf{u} \cdot \nabla \mathbf{u} = -\nabla P + \frac{1}{Re} \nabla^2 \mathbf{u} + \mathbf{f} \tag{4.1}$$

$$\nabla \cdot \mathbf{u} = 0 \tag{4.2}$$

where $\mathbf{u}$ is the velocity of the fluid, P is the pressure, Re is the Reynolds number: $Re = U_r L_r / \nu_r$, based on the reference velocity U_r, reference length scale L_r and reference kinematic viscosity ν_r . Finally, $\mathbf{f}$ is a forcing term that is used to represent the impenetrability of complex shaped solid vessel walls. For the forcing term we select a direct volume penalization in which

$$\mathbf{f} = -\frac{1}{\varepsilon} H \mathbf{u} \tag{4.3}$$

where $\varepsilon \ll 1$ is a forcing parameter. The forcing is defined in terms of the masking function H, given by $H(\mathbf{x}) = 0$ if $\mathbf{x} \in \Omega_f$ and $H(\mathbf{x}) = 1$ if $\mathbf{x} \in \Omega_s$. In this form the forcing term $\mathbf{f}$ allows to approximate the no-slip condition at the complex interface boundaries.

We solve the Navier-Stokes equations by employing symmetry-preserving finite volume discretization, closely following [100]. Details about the numerical schemes and time stepping which we use, are in Chapter 2. Complex aneurysm geometries are represented by the masking function H, which is a key element of our IB method as it defines fluid and solid parts of the computational domain. In fact, for those regions, where $H = 0$ the Navier-Stokes system is solved. In the regions where $H = 1$ the forcing term provides control over the velocity in the tissue basically representing no-flow in the tissue. We adopt periodic conditions for the total computational domain Ω, which implies proper connection of the 'corresponding' fluid parts of the domain effectively linking the outflow to the inflow of the geometry through the introduction of a smooth segment of vessel that takes care of the flow feedback, much in the same vein as the fringe region introduced in [85]. At places on the outer boundary of Ω where $H = 1$, the velocity is near zero throughout - in that case adopting periodic conditions has no actual consequences. At locations where $H = 0$ on the outer boundary of Ω, care must be taken to connect properly to a 'corresponding' fluid part of the domain, thereby completing the periodic flow model - an analysis of sensitivity of flow predictions on geometry reconstruction and domain definition was provided in Chapter 3.

In practice generating the masking function is a relatively fast and simple process, that requires a few steps to be performed. We start with the medical images obtained from the 3DRA procedure recording the local vessel structure and the possible brain aneurysm. This medical data-set consists of a very large number of parallel 2D slices, separated only a few micro-meters apart. The gray scale information contained in these 2D slices needs to be segmented in order to define the shape of the vessels. By choosing a threshold value the set of images can be converted into binary values from which the 3D geometry of the vessels and aneurysms can be reconstructed. This process was described in Chapter 3 for the aneurysm reconstructed from 3DRA data.

To satisfy periodic conditions, additional operations were performed on the segmented geometry. These involve isolating the relevant vessel segment by digitally cutting away parts

of the vessel and then connecting the ends of the vessel with a numerical 'connector' which restores periodicity of the computational flow model. We used two types of connectors: linear and cubic spline connectors to connect ends of the cut vessel. The effects of these additional steps in the geometry reconstruction on the flow inside the geometry were discussed in Chapter 3. It was observed that the relevant flow in the vicinity of the aneurysm bulge can be accurately simulated in the periodic flow model - the influence of 'cutting' and 're-connecting' was found to be small, provided a sufficiently large part of the original domain is retained near the bulge. We observed under normal physiological conditions that possible artificial effects of cutting and reconnecting vessels remain limited to a length of about one radius of the vessel. The smoothness of the connector was found to have less influence on the flow in and near the bulge. Since the medical imagery does not allow precise definition of vessel shapes due to the limited spatial resolution of the imagery and possible movements during recording of the data, we included bounding geometries, which are based on defining systematically 'nearby' masking functions. The main characteristics of the predicted flow appeared to be also bounded by flow properties in the bounding geometries, which was presented for steady flow simulations in Chapter 3.

In this chapter we work with a geometry, reconstructed from 3DRA data as shown in Figure 4.1(a). The part of the original geometry that is retained in the computational model is plotted in red, while the smooth connector based on cubic spline interpolation is shown in black. The initial medical data of the 3DRA scan consists of 256^3 voxels, with voxel width 0.1213 *mm*. This leads to a total physical length of the domain of 3.10528 *cm*. For numerical simulations it is convenient to work in the non-dimensional setting, for which all values for length, velocity, time etc. are scaled by reference parameters. The system after scaling remains a pure analogy of the physical system, and translations back and forward are always possible. In case of vessels and aneurysms, the radius of the vessel is a suitable reference length [24, 82]. We extract $R = 1.94$ *mm* from the 3DRA data, which brings us to a domain of length $31.0528/1.94 \sim 16$ in the non-dimensional formulation. Moreover, for the particular geometry we noticed that after segmentation and additional steps of cutting and connecting, the vessels filled only half of the volume in the y direction. This allows to remove the 3D tissue-cells in half of the domain as there is no flow in this part of the computational model. Thus, we arrive at a computational domain of length $L_x \times L_y \times L_z = 16 \times 8 \times 16$ and use grid resolution up to $n_x \times n_y \times n_z = 256 \times 128 \times 256$ to represent the geometry.

For simulations of steady flow in Chapter 3 we considered also coarsened grids of resolutions $128 \times 64 \times 128$, $64 \times 32 \times 64$ and $32 \times 16 \times 32$. We analyzed the convergence of the solution and could conclude that starting from a resolution of $64 \times 32 \times 64$ reliable results could be obtained. Under these resolution conditions a cross-section through a vessel is typically covered by about 15-20 grid cells in each coordinate direction. For Poiseuille flow it was found that under these resolution conditions the L_2-norm of the error in the velocity is maximally about 10 % - this level of accuracy is considered reasonable for our purposes - higher

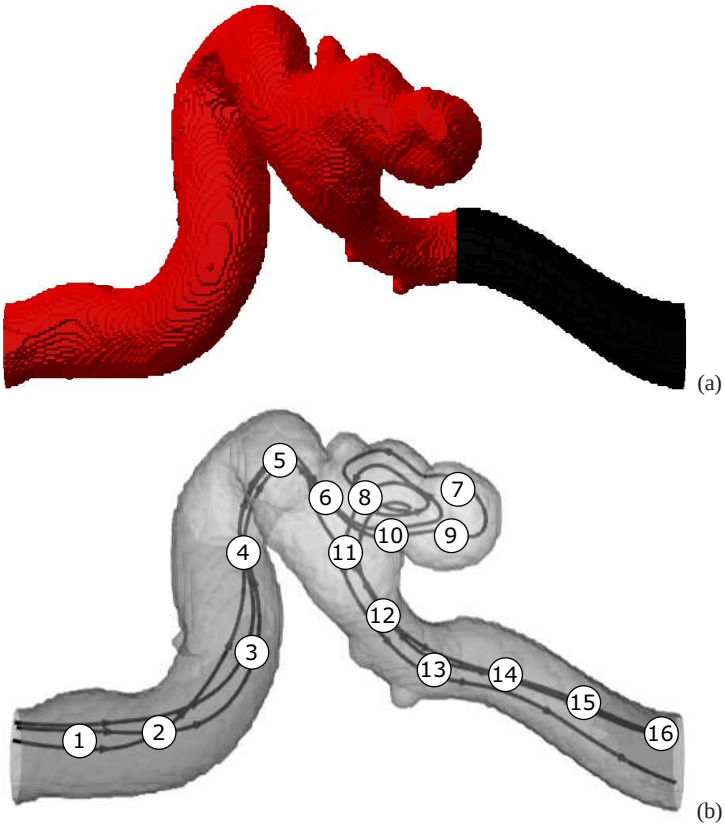

Fig. 4.1 3D masking function for aneurysm geometry (a) and typical streamlines with indication of the monitoring points of interest (b). The cut part of the geometry is plotted in red, while the connecting vessel is shown in black. Grid resolution is $256 \times 128 \times 256$. Streamlines in (b) illustrate simulations of steady flow at $Re = 250$.

accuracy requires a larger computational effort. During coarsening of the grid, bounding geometries can be systematically generated. These can be used to obtain the range of variability of the solution due to uncertainty in the precise flow domain, thereby further quantifying the quality of the predicted flow. In this chapter we will simulate pulsatile flow at a grid resolution $64 \times 32 \times 64$. Typical velocity streamlines following the main vessel and coming into the aneurysm bulge are shown in Figure 4.1(b). We also display schematically the approximate locations of several points of interest at which we will analyze the flow in more detail and investigate the transition. These points were chosen quite uniformly throughout the aneurysm geometry to analyze the flow dynamics in the vessel before, after and inside the aneurysm bulge.

4.2.2 Flow conditions and pulsatile forcing

To complete the computational model we need to define flow conditions which are realistic for blood flow in cerebral vessels and aneurysms and specify the pulsatile cycle in the flow-rate which is used to force the flow. The only parameter which is responsible for specifying the flow regime in (4.1) is the Reynolds number $Re = U_r L_r/\nu_r$, where U_r, L_r and ν_r are reference velocity, length and viscosity correspondingly. The range of Reynolds numbers characteristic of blood flow in the Circle of Willis, corresponds to laminar flow. To quantify this, we estimate the Reynolds number for physiologically relevant conditions next.

The reference length L is chosen based on the average radius of the cerebral vessel in the scanned part of the Circle of Willis. For the given geometry $L_r = 1.94\ mm$, which is consistent with [39] who found a value of $2.1 \pm 0.4\ mm$. The reference kinematic viscosity of the blood can be found as the ratio between the dynamic viscosity of human blood and the mass density. These quantities differ from person to person. By choosing typical values for the mass density $\rho_r = 1060\ kg/m^3$ and the dynamic viscosity $\mu_r = 3.2 \cdot 10^{-3}\ Pa\ s$ we arrive at a kinematic viscosity $\nu_r = 3.01 \cdot 10^{-6}\ m^2/s$. To complete the estimate of the Reynolds number, the reference velocity is taken as the ratio between the average volumetric flow-rate of the blood going through the vessel and an approximation of the area of a cross-section through the vessel. The flow-rate for blood can be measured by means of 3D MR angiograms [34, 67] in which values $Q = 245 \pm 65\ ml/min$ were found showing an uncertainty of about 25%. Based on the reference length L_r and an assumed circular cross section as approximation, the range for the reference velocity is $U = 0.345 \pm 0.09\ m/s$. These values are in very close agreement with the range $0.34 \pm 0.087\ m/s$ as obtained by [78] on the basis of TCD measurements. Combining these reference scales we compute typical Reynolds numbers to be in the range of $175 \lesssim Re \lesssim 300$. As key reference Reynolds number we adopt $Re = 250$, which in terms of chosen reference length and kinematic velocity corresponds to a velocity scale $U_r = 0.388\ m/s$. Later we will vary the Reynolds number to investigate the quantitative and qualitative sensitivity of the flow to this parameter. We also compute the flow at $Re = 200$ and $Re = 300$ as these reflect the differences in the blood viscosity, the sizes of the vessels and/or the velocity scales, which were found in literature. In case of diseased conditions we can expect an even wider range of Reynolds numbers, therefore we also compute the flow at $Re = 100$ and $Re = 400$. The same range of Reynolds numbers was suggested in [24, 82], based on slightly different choices for diameters and blood properties.

In order to compute pulsatile flow we need to impose a pulsatile cycle for the volumetric flow rate as an input for our numerical simulations. With the use of phase-contrast (MR) angiography [34, 67] or TCD sonography [78] the time-dependent cross-sectionally averaged velocity of the blood flow in cerebral arteries can be measured. In the current study the velocity was recorded in the middle cerebral artery by [22] using TCD. In Figure 4.2(a) we plotted a segment of 10 seconds of the pulsating velocity. The mean velocity value, obtained

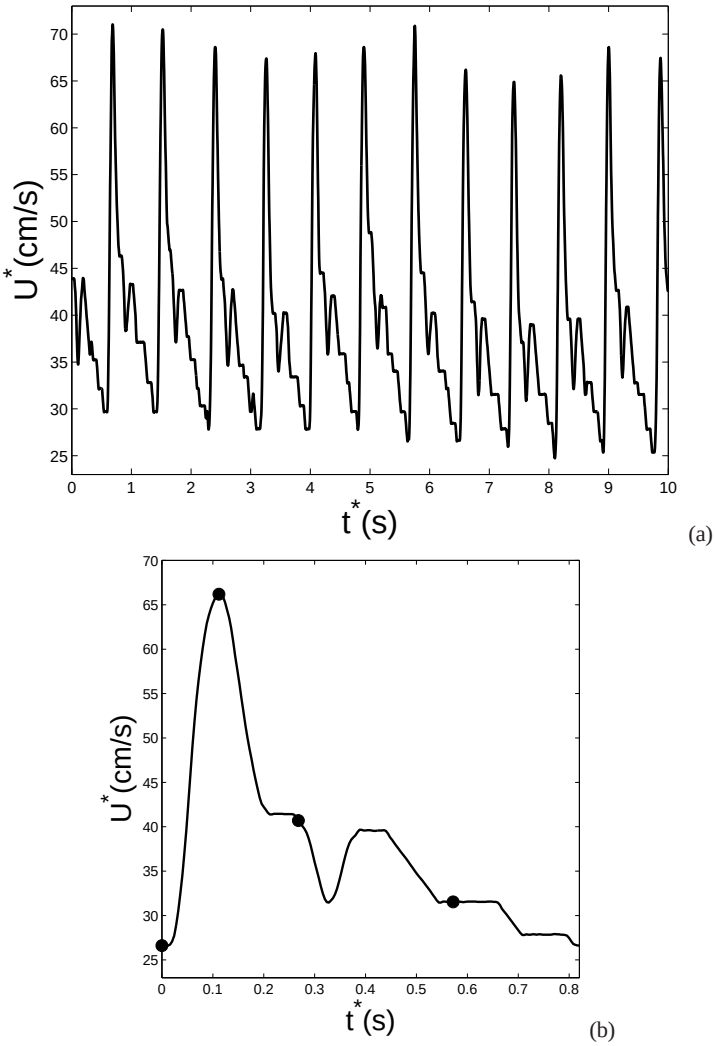

Fig. 4.2 Pulsatile velocity measured in the human brain using TCD sonography. Ten seconds velocity signal as measured in the MCA is presented in (a). The unit pulse (b) which was chosen from the original signal for computations contains also 4 points of interest during the cardiac cycle: $t_1 = 0.112\ s$, $t_2 = 0.324\ s$, $t_3 = 0.416\ s$ and $t_4 = 0.756\ s$ corresponding to peak systole, end systole, peak diastole and end diastole respectively.

by integrating this signal, is found to be $38.66\ cm/s$, which is very close to the reference scale selected above.

The computed pulsatile flow is maintained by using the actually recorded velocity signal as forcing. We choose a typical pulse (Figure 4.2(b)) and repeat it periodically. We illustrate 4 points of interest during the cardiac cycle (peak systole, end systole, peak diastole, end diastole) at which flow patterns will be analyzed in the next Subsection. For

our computations, we convert the recorded velocity pulse into a time-dependent volumetric flow rate. The selected pulse has a maximal velocity $U_{max} \approx 67.94\ cm/s$, which corresponds to a peak flow rate of $Q_{max} \approx 8.033 \cdot 10^{-6}\ m^3/s$, using the selected radius $R = L_r = 1.94\ mm$ and assuming a perfectly circular cross section. If we take the reference velocity $U_r = 0.388\ m/s$ corresponding to a Reynolds number $Re = 250$, we find similarly as reference flow rate $Q_r \approx 4.59 \cdot 10^{-6}\ m^3/s$. For convenience, we split the forcing signal in the non-dimensional formulation into a normalized flow rate pattern Q_0 which varies between 0 and 1, and an amplitude Q_{max}/Q_r such that the forcing used in the simulations becomes $Q(t) = (Q_{max}/Q_r)Q_0(t) \approx 1.75Q_0(t)$. The physical duration of one pulse is $t = 0.82\ s$. The reference time-scale can be computed as $t_r = R/U_r = 0.005\ s$. Thus at $Re = 250$ one pulse requires 164 non-dimensional time units.

The procedure to define the pulsatile flow rate can be extended to also address other Reynolds numbers. We take as reference Reynolds number Re and fix the reference length-scale to L_r (since we consider the same geometry) and the kinematic viscosity to ν_r (since we still consider the flow of blood). If we wish to simulate at another Reynolds number Re' this implies that the reference velocity scale is changed according to $U_r' = (Re'/Re)U_r$. Correspondingly, the time-scale changes into $t_r' = (Re/Re')t_r$ and hence, the 'new' number of dimensionless time-steps to take in order to complete one cycle of $0.82\ s$ of the pulsatile flow decreases with decreasing Reynolds number. Another consequence of changing the Reynolds number at constant length-scale and kinematic viscosity is that $Q_r' = (Re'/Re)Q_r$, as well as $Q_{max}' = (Re'/Re)Q_{max}$. Hence, the dimensionless forcing does not alter with changing Reynolds number and remains at $Q(t) \approx 1.75Q_0(t)$. The factor 1.75 denotes the 'contrast' in the pulsatile flow rate, i.e., the ratio between the maximal and the average velocity during a cycle - this quantity varies from one person to another and even slightly per heartbeat. The change in Re corresponds to a change in U_r, which affects the scale for the shear stress which is $\rho_r(U_r)^2$. The final result will be presented in dimensional form and include a wall shear stress in Pa and time measured in s, which allows a direct comparison with literature.

4.2.3 Reference pulsatile flow

For the reference case we perform pulsatile simulations at $Re = 250$ and first illustrate velocity traces per cardiac cycle. In 16 points, illustrated in Figure 4.1(b) we compute the velocity during one pulse and plot the results in Figure 4.3. We observe complex patterns of the streamwise velocity at all locations. In some points the flow follows the pulsatile forcing profile, as we would expect for laminar flow in roughly cylindrical vessels, e.g., points 1, 2, 12, 13, 15, 16. We also observe negative velocities, e.g., in points 4, 5, 8, which are related to the recirculation of the flow.

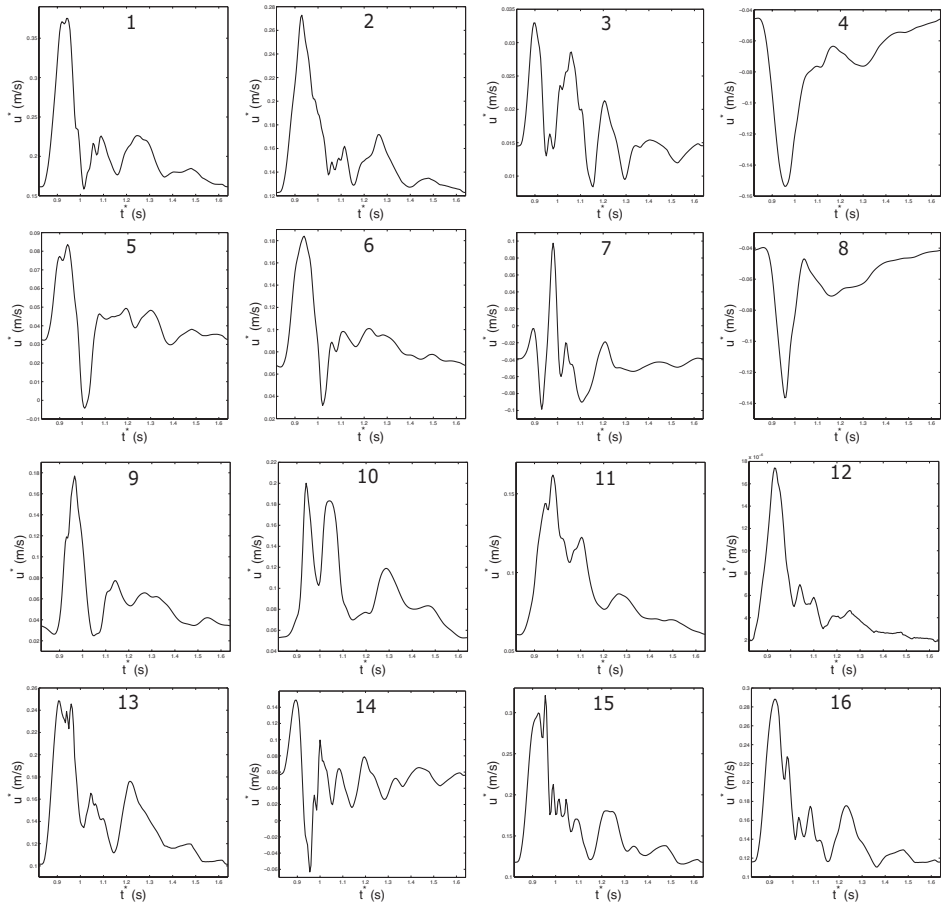

Fig. 4.3 Values of the x-wise velocity component during a heart beat at $Re = 250$ in 16 chosen locations along the aneurysm geometry. The number on top of every sub-figure corresponds to the label of the point, whose location is shown in Figure 4.1(b).

We next consider the pulsatile influence on the blood flow at characteristic stages during a cardiac cycle. Schematic representation of 4 points of interest is shown in Figure 4.2(b). The pulse duration is 0.82 s and we consider $t_1 = 0.112$ s, $t_2 = 0.324$ s, $t_3 = 0.416$ s and $t_4 = 0.756$ s corresponding to peak systole, end systole, peak diastole and end diastole respectively. These times during one cardiac cycle were also analyzed in [3, 15, 56], as they illustrate the typical behavior at peaks and minima during every stage.

In Figure 4.4 we present 2D velocity contour plots at 4 different cross sections along the aneurysm geometry and at 4 different cardiac stages. Two cross sections (first and last rows) were chosen in the vessel parts close to the ends of the selected domain at $x = L_x/8$ and $x = 7L_x/8$. Two other cross sections (second and third rows) are taken closer to the aneurysm bulge, at $x = 0.4L_x$ and $x = 0.5L_x$. The latter cross section was also analyzed for steady

flow in Chapter 3. The first column corresponds to the peak systole stage, which displays a rather intense density of contour lines, indicating the wider range of values involved. The second column as well as the fourth column correspond to the ends of systole and diastole and display relatively more quiet flow patterns, while the third column is related to the peak diastole stage, which is less vigorous than peak systole as seen from the reduced number of contour lines compared to the first column. We plotted negative velocities as dashed lines, which are clearly present in the second and third rows, displaying the circulation of the blood flow near the aneurysm bulge. In the vessels far away from the aneurysm bulge (first and fourth rows) the flow behaves much as Poiseuille flow and negative velocities are not present. Similar results were obtained in [15] where the effect of flow rate during the cardiac cycle in different aneurysm geometries was investigated.

4.3 Transitional pulsatile flow

In this Section we first show the occurrence of transition in pulsatile flow in case the Reynolds number increases from the normal range around $Re = 250$ to the pathological range as high as $Re = 400$ (Subsection 4.3.1). Then we establish the robustness of this phenomenon by showing that it can be observed in a variety of flow properties and that it arises at basically all locations in the domain (Subsection 4.3.2). This motivates to have a closer look at the transition by considering the full dynamic spectrum of pressure and velocity response (Subsection 4.3.3).

4.3.1 Shear stress response in normal and pathological flow

Experimental observations of ‘turbulence’ inside cerebral aneurysms were presented in [23], confirmed by clinical study where high frequency ‘bruits’ were measured by a phonocatheter. Later, in [45] and [49] alternative clinical studies were presented, where in a non-invasive way intracranial blood flow sounds were recorded and analyzed. It was shown that certain high frequency sounds are present in patients with cerebrovascular diseases and not in healthy people. This suggests that if a cerebral aneurysm is present, qualitative changes in the flow may occur which lead to high-frequency bruits.

Is it possible to hear an aneurysm? Can one hear one’s own aneurysm? Can critical aneurysms be detected by analyzing sound? Motivated by the experimental observations and these questions, we decided to perform a set of simulations at different Reynolds numbers. We consider the reference flow at $Re = 250$ to correspond to healthy cerebral blood flow circulation. Next to this we also perform simulations at pathological flow conditions: at lower Reynolds numbers $Re = 100, 200$ and at higher Reynolds numbers $Re = 300, 400$. The range

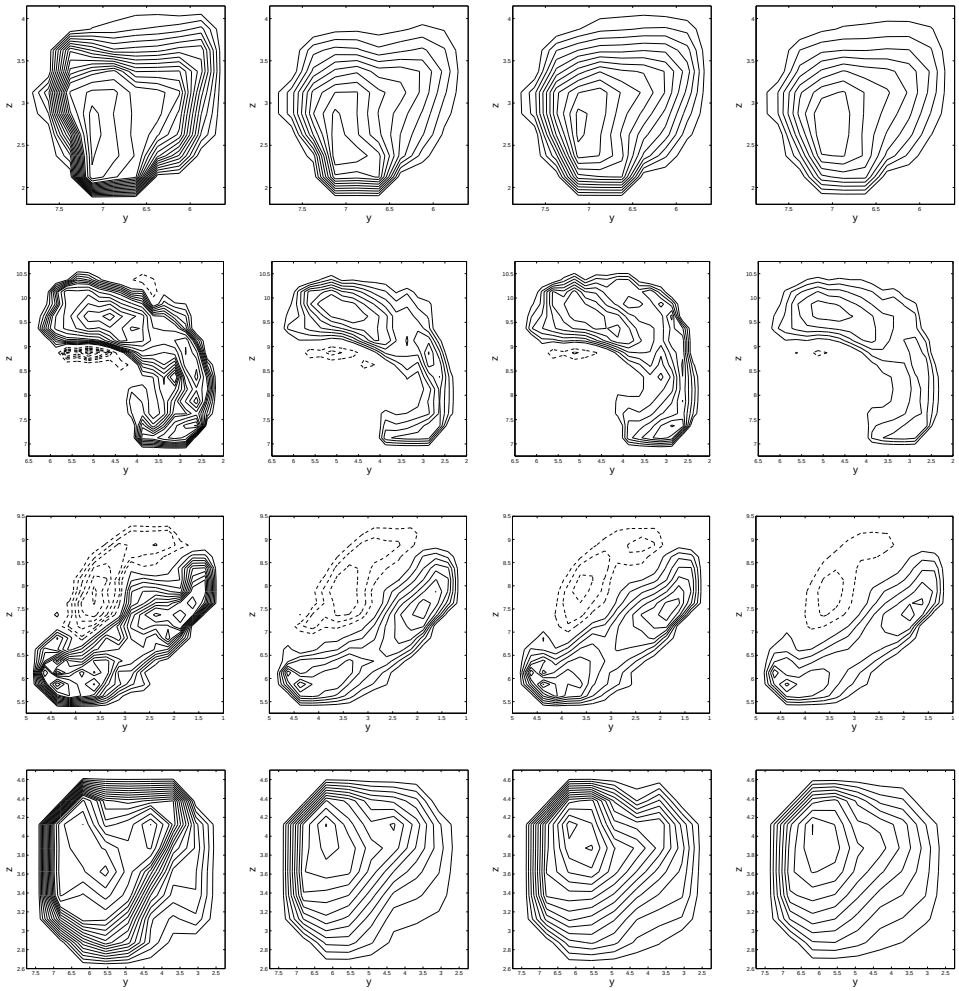

Fig. 4.4 Velocity patterns at different stages during the cardiac pulse in four cross-sections along the aneurysm geometry. The columns correspond to the stages of the cardiac cycle, related to peak systole, end systole, peak diastole and end diastole respectively. The rows correspond to the different cross sections along the aneurysm geometry. In the first and fourth rows we plot the cross sections at $x = L_x/8$ and $x = 7L_x/8$. The second and third rows correspond to the flow nearer the aneurysm bulge at $x = 0.4L_x$ and $x = 0.5L_x$. Simulations are at $Re = 250$.

$Re = 100 - 400$ was motivated in Subsection 4.2.2 as a physiologically realistic regime for cerebral blood flow.

In Figure 4.5(a) we present the dynamic response of the maximum shear stress for 10 pulse cycles. We observe different levels of magnitude at different flow regimes as well as the differences in the dynamical pattern of the computed results. To appreciate these differences in more detail we show in Figure 4.5(b) only one pulse cycle (namely corresponding to the third heart beat in these simulations). The mean value averaged over 10 pulses at $Re = 250$ is found to be around 1.4 *Pa* with peak values near 2.6 *Pa*. At higher (possibly pathological) Reynolds number $Re = 400$ we observe a change in mean value up to 2.5 *Pa* and a considerable increase in peak values to 6.2 *Pa* averaged over 10 pulses. These values show the same general magnitude as reported in [29, 70]. Transitional dynamics is clearly observed in Figure 4.5(b). Slow viscous flows at $Re = 100$ and $Re = 200$ smoothly follow the pulsatile forcing profile. At $Re = 250$ more dynamics appears to happen especially during the systole decay phase. The most interesting flows are at $Re = 300$ and $Re = 400$, where the nonlinear consequences of Navier-Stokes dynamics are firmly present. Also the level of maximal magnitude increases a lot and becomes slightly unsteady from one pulse to another at $Re = 400$ as can be seen from Figure 4.5(a). This transition was also observed in simulations of other realistic aneurysms and even for the simplified model aneurysms consisting of a curved vessel to which a spherical cavity was added [60]. Note, that these striking phenomena are not due to the size of the time-step or spatial inaccuracies, as was verified by performing a set of test simulations in which we reduced the time-step by a factor of two compared to the typical value of $\delta t = 10^{-4}$ as used in the reference case, and increased the resolution by a factor of two to record the flow during part of a cycle.

In order to establish reliability of the transition we also recorded the response in nearby inner and outer bounding geometries, which was found to give practical bounding solutions [61]. For pulsatile simulations we consider only nearby 'inner' and 'outer' geometries which have a slightly smaller and slightly larger volume of flow domain. These bounding geometries allow a narrow band of solutions, characterizing the sensitivity of the simulation results. In Figure 4.6 we show the maximum shear stress during one cycle at three Reynolds numbers - in each case we collect the basic solution together with its two bounding solutions. The variability bands are plotted as grey shading allowing to appreciate better the dynamics of the bounding solutions. Thus, at $Re = 100$ and $Re = 250$ bounding solutions closely follow the basic solution, representing relatively narrow sensitivity bands with a general variability range of 10-15 %. At $Re = 400$ the transition is present also in bounding solutions, leading to the wider variability band, with more increased peak values for the inner geometry. Now that we have transition established, we will consider the robustness of this phenomenon regarding flow-quantity and physical location at which transition is measured.

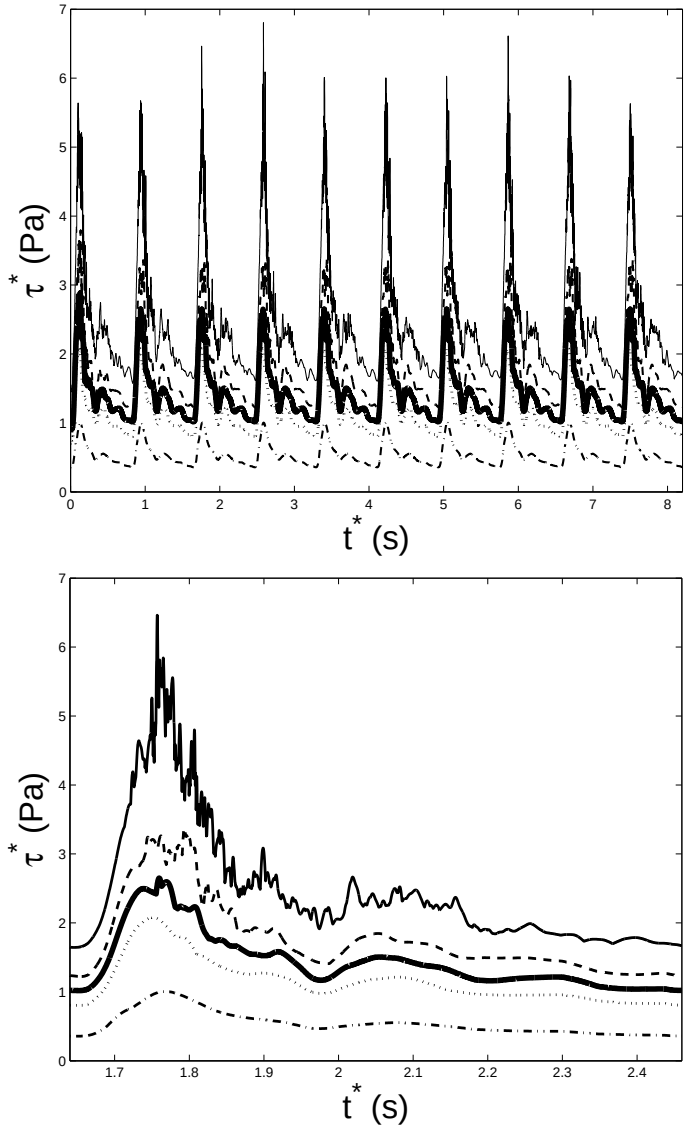

Fig. 4.5 Maximal shear stress for realistic pulsatile flow in the aneurysm geometry. The reference at $Re = 250$ is shown (bold, solid). Lower value are shown as $Re = 200$ (dot), $Re = 100$ (dash-dot), while higher values are displayed as $Re = 300$ (dash) and $Re = 400$ (thin, solid). The average stress levels decrease with decreasing Reynolds number.

4.3.2 Robustness of pulsatile transition

In this subsection we will establish the robustness of the transition phenomena observed in the previous subsection. In particular, we will show that this phenomenon is equally present

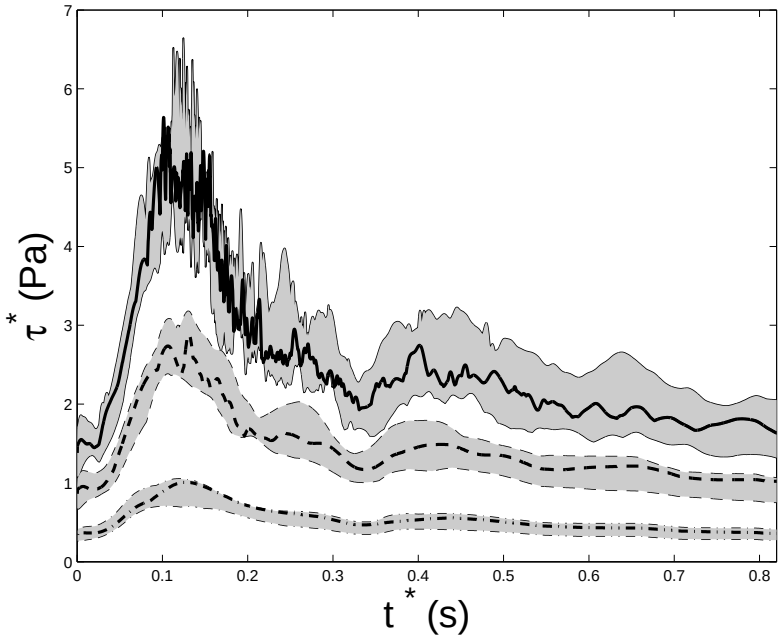

Fig. 4.6 Maximum shear stress at different Reynolds numbers, together with the variability bands computed in bounding geometries. Smooth dynamics at $Re = 100$ (dash-dot) and $Re = 250$ (dash) next to the striking unsteadiness at $Re = 400$ (solid). Transition is shown to be robust to small differences in geometries.

in a variety of flow properties such as the three velocity components and the pressure. This shows transition to be independent of the quantity that is being monitored. Subsequently, we will turn attention to the pressure response and show that the qualitative features of the transition appear similarly at different measuring points in the flow domain. This shows an independence of location.

In Figure 4.7 we show the velocity components u, v and w and the pressure P at point 11 (see Figure 4.1(b)) during one pulse at three Reynolds numbers. We observe clear transition in all presented quantities. Not only levels for u, v, w and P are increasing with Re but also the dynamic pattern of the response during one cardiac cycle is changing considerably. This illustrates that transition arises equally well in any of the flow quantities. Note that in Figure 4.7(d) we present the 'numerical pressure' P as obtained in the current flow solver. This numerical pressure is not the same as the physical value for the pressure since no zero-pressure level was fixed in the Poisson solver of the incompressible model.

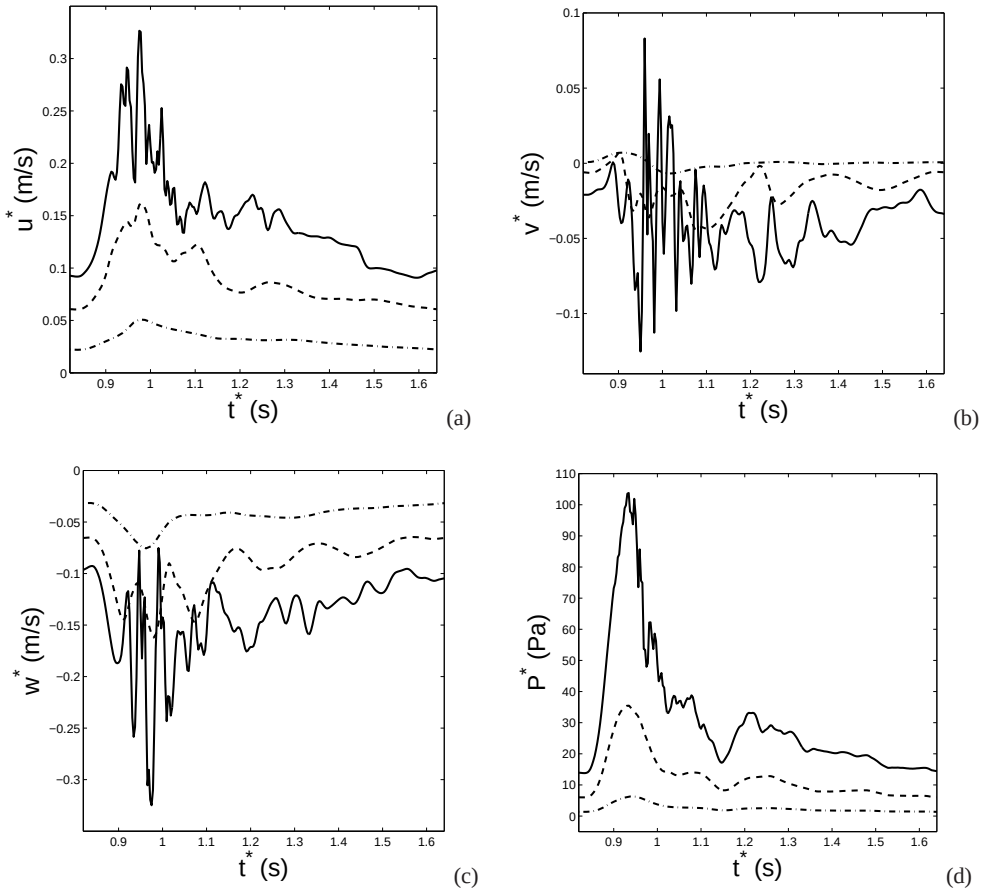

Fig. 4.7 Velocity components u, v, w and P at point 11 in the vessel opposite the aneurysm bulge. Transition at different Reynolds numbers is present for all these quantities. Simulations are at $Re = 100$ (dash-dot), $Re = 250$ (dash) and $Re = 400$ (solid).

4.3.3 Frequencies of the pulsatile solution

There are a few ways to measure the flow inside cerebral vessels and aneurysms: invasively, measuring pressure directly by inserting a pressure sensor on a catheter and non-invasively as, e.g., using TCD to obtain time-dependent mean velocity time traces in the arteries nearby the scalp. Sounds inside cerebral vessels can also be measured in both ways: with a phono-catheter [23] and with a sonic detector [45] or a transducer [49] which are applied close to the head or even attached to the scalp. Afterwards the signals recorded by any of the above listed techniques can be analyzed by considering their spectra.

We translate the numerical signals computed in the 16 monitoring points during several cycles into the corresponding spectra. As was shown before, transition occurs quite inde-

pendently of flow-quantity. Here, we concentrate on the u velocity and present the spectra in four characteristic points along the aneurysm geometry, chosen from the 16 recorded signals. In particular, we choose one point at the beginning of the aneurysm geometry (point 1), where flow is close to a Poiseuille type flow. We also include point 11, located opposite the aneurysm bulge. Two more points are 7 and 10, which are inside the aneurysm bulge at different distances from the main vessel (see Figure 4.1(b)). Similar choices for points of interest near and inside the aneurysm are shown in [3, 23]. In this way we not only obtain the spectra of u but also establish that transition arises at all locations in the flow domain.

In Figure 4.8 we show the Fourier transform of the time-trace of the u-velocity component in point 11. We computed the spectrum over five full heart beat cycles at three Reynolds numbers and plot the results in Figure 4.8(a). On the vertical axis we plot the square of the magnitude of the Fourier coefficients. The frequencies are represented in Hz on the horizontal axis. The main component due to the cardiac cycle at 0.82 s is clearly observed by the peak at 1.22 Hz. Pronounced peaks arise at all harmonics of the basic heart beat, separated by very low values for the sub-harmonics. The low sub-harmonic values illustrate the degree of periodicity of the velocity trace at the different Reynolds numbers. In order to express the dominant contributions to the spectrum more clearly we concentrate on the harmonics of the heart beat only. This is shown in Figure 4.8(b) representing the 'envelope' of the spectrum. Markers are used to indicate the discrete frequencies. Transition in the flow due to increasing Reynolds number is clearly observed by the much higher values for all frequencies. In particular, we notice an even stronger relative increase of the importance of the higher frequencies, also in the audible range. In the sequel we will represent all spectra in terms of the harmonics only.

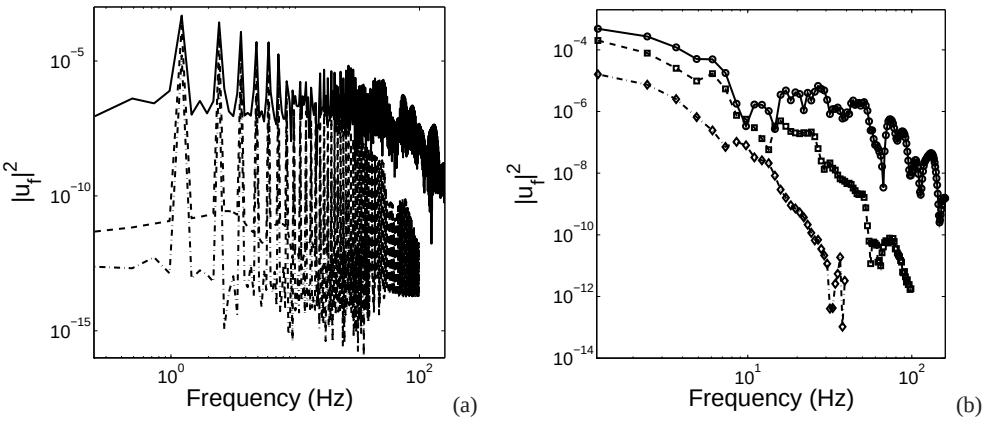

Fig. 4.8 Fourier transform of the streamwise velocity in point 11 at three different Reynolds numbers: $Re = 100$ (dash-dot), $Re = 250$ (dash) and $Re = 400$ (solid). In (a) all computed frequencies are shown, in (b) only the harmonics of the heart beat at 1.22 Hz are shown by markers.

In Figure 4.9 the Fourier transform of the u velocity component is shown in the four selected locations. The spectra clearly display transition with increasing Reynolds number, independent of the physical location in the flow domain. At all locations the tails of the spectra are well separated with increasing Re, showing the increased presence of components of high frequencies. At lower frequencies the spectra also increase with increasing Re reflecting the increase in the flow velocity in this case.

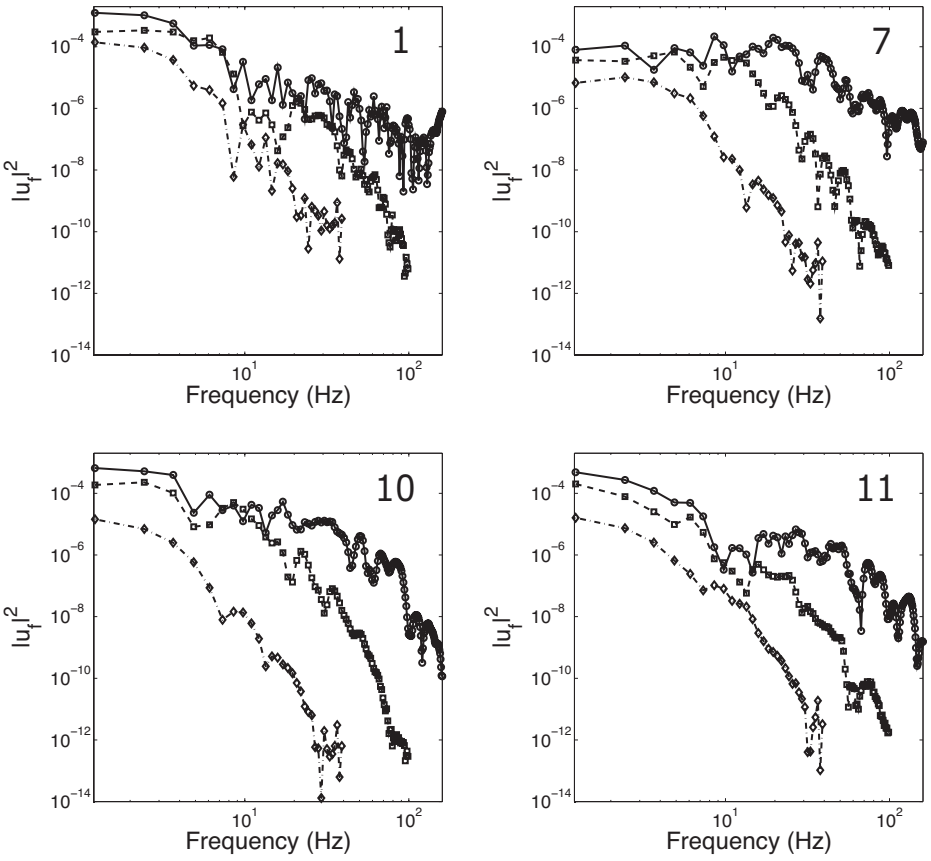

Fig. 4.9 Fourier transform of the streamwise velocity at three different Reynolds numbers in 4 points in the vessel: at the beginning of the flow domain (point 1), close to the aneurysm bulge (points 11) and inside the aneurysm bulge (points 10, 7). Simulations are at $Re = 100$ (dash-dot), $Re = 250$ (dash) and $Re = 400$ (solid). Only the harmonics of the heart beat at 1.22 Hz are shown.

4.4 Concluding remarks

In this chapter we presented a complete computational model for the simulation of pulsatile blood flow in cerebral aneurysms. Based on the volume penalizing IB method, the current model allows to compute flow and forces that emerge in aneurysms under pulsatile flow conditions. We analyzed several solutions at different flow regimes and observed strong transition to complex time-dependence at higher Reynolds number, which may be of interest for medical monitoring. We emphasized this point in terms of presenting time-traces of the solution as well as the corresponding spectra.

The aneurysm geometry considered in this study was reconstructed from 3DRA medical data. The IB method allows a quite direct transformation of the gray scale voxels contained in the images into fluid and solid 3D cells in the computational domain. Flow conditions corresponding to physiologically relevant cerebral flows were estimated, based on data obtained from literature. Numerous clinical studies show variability of the measured sizes of cerebral arteries, ranges for blood flow velocity and viscosity. Combining the variability ranges of these components we arrived at the approximate range of flow conditions, that would apply for cerebral flow in the Circle of Willis. As a typical reference cerebral flow we considered $Re = 250$. When taking into account all the uncertainties we obtained flows in a range of $100 \leq Re \leq 400$. At these different flow conditions we performed pulsatile flow simulations. The main purpose of this study was not just to compute the flow with given parameters, but to assess how the variability in the parameters translates into a confidence interval around the basic final solution.

The imposed pulsatile profile was obtained from TCD measurements of the velocity of the blood flow in the middle cerebral artery in the brain. We chose a typical pulse, normalized it and translated this into the volumetric flow rate assuming a circular cross-section of the vessel. We repeated this signal periodically as flow forcing which leads to a model for the time-dependent pulsatile flow. We performed pulsatile simulations at different Reynolds numbers and analyzed the main solution and its components. In particular, we considered velocity, pressure and maximum shear stress.

Increasing or decreasing the Reynolds number has a marked effect on the dynamic response. At the lower Reynolds numbers the response of the solution is seen to be smooth, following the imposed pulsatile profile. At the higher Reynolds numbers the natural Navier-Stokes nonlinearity seems to become dominant, which makes the numerical response lively by the emergence of relatively high frequency components of the solution. In addition, the amplitude of the solution components rises considerably, clearly expressing the transition towards complex pulsatile flow in which much higher frequencies gain in dynamic importance. We investigated in more detail this transition and showed that it is robust to choice of the computed quantity and to the location in the aneurysm geometry. The method of bounding solutions was employed to arrive at a confidence interval around the basic solution - this

was illustrated for the time-dependent maximum shear stress. Furthermore, we looked into the spectra for the streamwise velocity. Much higher levels of both - high and low frequencies arise at increased Reynolds number, which may be associated with an increased risks to the patient. Recording the spectrum of frequencies and analyzing trends in their levels may become relevant in medical practice and used as an easy monitoring procedure.

Chapter 5
Conclusions and Outlook

Overview of medical problem and role of CFD. These days several techniques are available to visualize the cerebrovascular system from which one may reconstruct the 3D geometries of a wide range of vessels. Starting from this capability, in this thesis we formulated a precise mathematical model with which the flow of blood inside the vessels can be predicted, thereby enhancing the relevance of the medical imagery on a patient-specific basis. To simulate flow in actual vessels, we developed and applied a numerical method with which the recorded 3D geometries can be handled in terms of an Immersed Boundary (IB) method. The governing equations for fluid flow were solved for the particular medical condition in which aneurysms form on vessels in the Circle of Willis - the main blood supplying system of the human brain. In this chapter we summarize the main findings of this thesis and sketch a number of further developments that are desired before the flow simulation approach can be integrated in medical practice.

Computational modeling becomes more and more important in the process of medical decision making, e.g., dealing with the dilemma whether or not to embark upon a risky but potentially life-saving surgery of a recorded aneurysm. Flow and forces associated with the flow of blood through the vessels and the aneurysm can be assessed with steadily growing reliability using Computational Fluid Dynamics (CFD). The ultimate problem is that of assessing the risk of rupture of the cerebral aneurysm due to slow degradation of the tissue in the vessel wall, and to weigh this risk against that of actual surgery. Based on the size, shape and location of the detected aneurysm, neuroradiologists currently need to advice on the best way of treatment. In practice there are two procedures to treat an aneurysm: direct clipping of the aneurysm near its neck, which requires to create access to the deeper structures in the brain, or applying a coiling procedure during which the aneurysm cavity is being filled with a thin flexible coil. In both cases the direct goal is to try to block further blood flow to enter the aneurysm bulge and to prevent its rupture. However, both procedures are highly risky and a further medical interest therefore lies in the ‘third option’, i.e., that of postponing surgery

and continuing to monitor the development of the aneurysm. In order to take this option with some confidence, prediction of the expected development of the aneurysm starting from the actual state of the patient is the key challenge. This requires knowledge of the pulsatile flow through the local vasculature and the flow-vessel wall interaction that emerges from it since this is at the root of possible further degradation of endothelial cells in the lining of the wall. Such information can only be accessed by mathematical modeling and flow simulation as non-intrusive measurements of the flow profile and vessel wall response are not possible on the scale of cerebral aneurysms. This puts computational modeling of flow in cerebral aneurysms in its timely context - only because of the combination of modern medical imaging techniques and image processing, with high-performance flow simulation of the emerging blood flow, we can now understand the hemodynamics in detail on a patient-specific basis.

Contribution of this thesis. In order to actually simulate flow in complex vessel domains a number of steps need to be taken. These were discussed in separate chapters in this thesis. To be more precise: the development of the IB method including its validation was taken up, subsequently, an extension was made to complex flow domains extracted from medical imagery, such as obtained using 3DRA, and finally pulsatile flow variations were imposed as measured using Transcranial Doppler (TCD) Sonography, to be able to track the precise evolution of the flow under transient conditions. These three main steps will be summarized in some more detail next.

- **Immersed Boundary Method. Masking strategies.** We started with the introduction of a computational model, based on the incompressible Navier-Stokes equations, in which an additional forcing term determines the complex geometry in our IB method. Numerically we solved the Navier-Stokes using a skew-symmetric finite volume discretization closely following [100]. A key element of the IB method is the so-called masking function. This is a binary function with which we identified at any location in the domain whether it is ‘solid’ or ‘fluid’, allowing to represent objects immersed in a Cartesian grid. Based on the property in the center of a cell, or associated with the corner points, we arrived at a number of slightly different strategies, to define complex-shaped fluid domains. The geometry obtained on the basis of fluid/solid properties in the center of the cell was referred to as ‘basic’, while other geometries were called ‘bounding’. The bounding geometries were further divided into ‘inner’ and ‘outer’ geometries, depending on whether the fluid part of the domain is generally smaller or larger than the basic flow domain. Each cell was allowed to be either solid or fluid, giving rise to a staircase representation of the fluid-solid interface in our method.

  A detailed validation analysis of the IB method was provided for Poiseuille flow in a tube with a circular cross section. We found first order convergence of the numerical solution

as well as of its gradients. Reliable findings with relative error below 10 % were obtained with this IB method, already at fairly coarse meshes with about 16 grid cells across a velocity profile. We also showed the influence of the masking function strategy on the level of accuracy of the numerical solution. Next, we applied our method to curved vessels and a model aneurysm, for which we studied the flow at different conditions, characterized by the values of the Reynolds number $Re = 100$ and $Re = 250$. These values for the Reynolds numbers were suggested by physiological conditions corresponding to flow of blood in the Circle of Willis. For these model geometries we computed velocity fields to understand the behavior of the flow, and shear stresses, which are related to the growth and possible rupture of aneurysms. High shear stress areas were observed near the rims of the geometry, e.g., in the region where the aneurysm is connected to the vessel and inside the aneurysm bulge, where the flow develops a vortex. Comparing two cases - flow in a curved vessel and in a model aneurysm - we noticed that the presence of an aneurysm leads to reduction of shear stress levels, which is consistent with observations in [84].

- **Realistic geometries. Reconstruction.** Next, we moved on to the application of the IB method to realistic aneurysm geometries. The segment of the cerebrovascular system that contains an aneurysm was reconstructed using medical images obtained with three-dimensional rotational angiography (3DRA). We focused on the sensitivity of flow predictions to the various steps of the vascular reconstruction process from the 3DRA data. After standard segmentation and simplification processes we considered the main steps needed to generate the masking function for our simulations. We illustrated the IB method for a realistic aneurysm and analyzed the role of (i) numerical resolution of the geometry, (ii) the actual choice of the vascular segment that is used in the flow simulations, (iii) the outflow/inflow 'connector' used to embed the recorded vessel geometry in the periodic flow domain and (iv) bounding geometries motivated by the inherent uncertainty in the medical images. We simulated steady flow for a reference geometry in which a cubic spline interpolation was used to define a smooth connector vessel at $Re = 250$ and visualized the complex vortical flow that develops in the aneurysm and its coupling to the simpler flow structure in the upstream and downstream connecting vessels.

  To quantify the sensitivity of the findings, we included two additional simulations: one in which the connector is a straight segment of pipe and one in which a shorter segment of the original recorded vessel was retained as part of the flow domain. We observed that the smoothness of the connector affects the flow only by a small amount of a few percent relative error in the added connector parts. More importantly, the differences remained spatially localized and virtually did not influence the flow in and near the actual aneurysm bulge with relative deviations reducing to 10^{-5} between the reference geometry and the geometry with straight connector. Likewise, we noticed that the use of a

considerably shorter segment of the original vessel geometry around the aneurysm bulge hardly affected the prediction of the flow in and near the aneurysm. Comparison of these simulations showed that possible artificial aspects of 'manufacturing' a vessel structure to embed the recorded vessel segment remained localized to about one vessel radius at normal physiological conditions.

Practical bounding solutions were shown to yield clear reliability bands around the reference solution obtained with the basic masking strategy. This also motivated a fast and simple method for accelerating computations of a wider reliability band, by including coarser grids which allows to perform simulations up to around 128 times faster if bounding solutions at four times reduced resolution would be sufficiently accurate for medical practice. This approach which might be very helpful for supporting medical decisions.

- **Pulsatile flow. Transition.** Finally, to complete the computational model we turned to simulations of pulsatile flow inside cerebral aneurysms. We showed that the flow undergoes a transition from an orderly state at low physiological Reynolds numbers, in which the pulsatile forcing is closely followed in time, to a complex response with strongly increased high-frequency components at higher Reynolds numbers, i.e., at higher flow rates and larger aneurysm sizes. The pulsatile variation of the flow rate was modeled in terms of measured vessel-averaged velocities in the vicinity of the aneurysm, using noninvasive TCD sonography. We simulated the pulsatile flow at a range of flow regimes: as the reference physiologically relevant situation we choose $Re = 250$. In order to capture differences due to changes in the flow regime, we also computed the flow at $Re = 100, 200, 300$ and 400. The computed velocity and stress levels were found to correspond to realistic values. For flow at $Re = 250$ the average shear stress value was found to be 1.44 *Pa*, with peak value at 2.88 *Pa*. With increasing Reynolds number, the flow shows strong transitions whereby the hydrodynamic response displays additional high-frequency components. The values for averaged shear stress increased up to 2.46 *Pa* and for the maximum shear stress - up to 6.8 *Pa* when $Re = 400$. The numerical reliability of the predicted transition was quantified on the basis of practical upper and lower bounding solutions, expressing the sensitivity of the flow to uncertainties in the recorded aneurysm geometry. The transition was found to occur in all sorts of quantities such as velocity components u, v, w and pressure p. We also showed that flow undergoes this transition independently of the location at which we monitored the flow response in the flow domain embedding the aneurysm geometry. Analyzing in more detail flow near the aneurysm and inside the aneurysm bulge, we computed the spectrum of the velocity response. The significant increase of small-scale, high-frequency structures at high Reynolds numbers was clearly expressed by large changes in the tail of the velocity fluctuation spectra, linking our simulations to earlier clinical experiments reported in [23]. The hydrodynamic transition in

developing aneurysms as predicted by simulations may have clinical non-invasive, inexpensive and fast screening application in the future based on recording high-frequency characteristics of 'aneurysm bruits' with acoustic means. This requires additional, technological investigations.

Outlook. The application of computational support in the monitoring and treatment of cerebral aneurysms is a field of much research. Accessibility of time-dependent flow fields in all relevant detail is a crucial point from which to depart toward developing predictive capability for the associated slow growth of the aneurysm bulge. In order to achieve a closer connection with medical practice several computational modeling steps still need to be taken, such as the development of higher order accurate methods, multi inflow/outflow configurations, flow-structure interaction in which a full coupling to slow degenerative processes of endothelial cells is made, as well as modeling of mechanical properties of brain tissue to also address aneurysm compliance during the pulsatile cycle. This brief sketch shows both the promise as well as the various developments that are still needed in order to make the pathway from medical imagery to quantitative decision support, including analysis of various scenarios of intervention, more reliable as well as fully automated. In more detail, we discuss possible directions for improvements next.

- **Numerical improvements.** Although several steps in the development of an IB method for prediction of blood flow inside cerebral aneurysms were made, many aspects require further attention. From the numerical point of view, the method can be improved further to obtain higher order accuracy. The current volume penalizing IB method is first order accurate. Developments in which sub-grid forcing is included [79] to impose no-slip conditions at fluid-solid interfaces, at scales smaller than a grid cell, can be used to increase the formal order of accuracy to two - this appears a relevant extension of the IB approach and should be considered in more detail in the near future, allowing to cut down on the computational cost and/or increase the accuracy of flow predictions.

  The reliability of simulations can be assessed not only for the classical case of Poiseuille flow in a cylindrical pipe, but also with data from physical and medical experiments. While performing physical experiments, care needs to be taken of the dynamic similarity of the flow in the Circle of Willis and in the experimental model. This leads to a set of possible values of diameter, viscosity and velocity in an experimental scale model. In order to maintain viscous flow, special liquids as glycerin can be involved. Pulsatile flow experiments were presented in [23], where turbulent motions were observed inside the aneurysm and high frequencies bruits were detected. We also developed a physical experiment based on water as medium, for an aneurysm phantom which was about 10

times the size of a typical aneurysm. However, measurements at the low Reynolds number required by physiological conditions are very challenging and a proper development in collaboration with an expert fluid dynamics laboratory is advised. Complex structures at rather high Reynolds number flows were easily observed inside the aneurysm cavity, by visualizing them with ink as a tracer. Thinking of realistic blood flow circulation, carrying oxygen and other important chemical elements through the vessels, the comparably long residence time of ink inside the aneurysm cavity may imply a mechanism that can lead to the degradation of the endothelial layer of vessel walls and possible growth of the aneurysm.

High performance computing is one of the main improvements needed, as the speed of computations at present is not high enough to support medical decisions 'on-line' during surgery or shortly after the diagnostics. We implemented OpenMP parallel processing, which increased the speed of computations up to a factor around 20 on 32 CPU's. However, for high grid resolution as for example needed in order to simulate the flow in the directly reconstructed geometries using 256^3 voxels, pulsatile flow simulations corresponding to one heart beat take approximately 150000 hours of total CPU time. This is not yet practical. Turning to real high-performance computing in which a much larger number of CPU's can be used effectively, can significantly reduce the wall-clock time of a computational analysis of a patient. This requires restructuring the current implementation and adopt, e.g., MPI (Message Passing Interface) as basis instead of OpenMP. Another development involves the introduction of a block-structured flow solver so that large numbers of grid points that now are in regions without flow can be eliminated from the computational model. This combination of a block-structured approach and the IB method with proper parallel performance, holds promise to yield the speed-up that is required to make integration in medical practice a reality.

- **Model improvements.** In order to bring our model to the hospital, we also need to improve the model of blood flow. We approximated blood as a Newtonian fluid, while real properties of blood suggest non-Newtonian corrections. Various numerical studies have been done to compare these two approaches [6, 15, 24, 28, 38]. General similarity in the behavior of the blood flow and its main characteristics was observed with differences up to 10% [24, 28]. For quantitative predictions it may be relevant to incorporate the non-Newtonian model of blood flow in the future.

  From a mechanical point of view, flow structure interaction (FSI) is an important element of realistic modeling. Two types of FSI can be distinguished - per heart beat and over long time. Currently, we simulate flow in the vessels with rigid walls and do not incorporate any FSI properties. The geometry is defined via the masking function before starting the

simulations. Experimental studies, e.g., based on measurements in medical images taken at different stages during the pulsatile cycle by [69] showed that in the human brain the movements of the arteries are rather small compared to the diameter of the cerebral vessels. However, for realistic modeling movable walls should be considered, which will in practice mean that the masking function becomes solution dependent and dynamic as well. Another aspect of FSI is related to the multiscale aspect of the problem, relating the 'fast' pulsatile flow scales to the long-term aneurysm development. An example of such modeling of the aneurysm growth is presented in [102], where detailed mechanisms for the interaction of blood flow with endothelial cells and tissues are incorporated in the computational model. Validation of aneurysm growth models can be performed by analyzing follow-up data of patients. In this way for different patients, and thus, different aneurysm geometries and flow conditions, the model can be validated and optimized.

- **Automation.** The IB method allows for a direct link between the recorded medical images and the masking function. Considerable (human) time saving could be found from an automated translation of the 3DRA data into the masking function. For this purpose the one inflow - one outflow boundary condition approximation should be changed into many inflow - many outflow mode. In this way the complexity of cerebral vessels and aneurysms can be fully reflected in the computational model and additional manual steps, as cutting, connecting, possibly rotating, adjusting to the computational box, will not be necessary anymore. Thus, complex geometries, e.g., the whole Circle of Willis can be used for blood flow simulations. This is essential for understanding the global blood circulation next to the localized analysis in the neighborhood of an existing aneurysm.

  The method of practical bounding solutions was put forward to quantify sensitivity of flow predictions due to uncertainties in the precise vessel geometry. It can become part of an automated process of generating masking functions and analyzing patient-specific cases. The direct transformation of voxels into the Cartesian grid cells leads to a staircase approximation of vessel and aneurysms geometries. Smoothing of the geometry implies approximating of the initial medical images, while on the other hand staircase walls of the vessels are unrealistic. We proposed to keep the initial transformation of voxels into 3D grid cells, and next to the basic geometry consider also slightly different geometries, which bound the basic configuration from inside and outside. The corresponding numerical solutions appeared to be also providing a bounding band which identifies the relevant range of simulation. Automatic generating of bounding geometries (also of lower grid resolutions) next to the basic shape converted from the initial images, will be beneficial. A first impression can be obtained very quickly at a lower grid resolution, while the precise solution can also be computed to give further details of the flow structures and an error bar signifying the reliability of the predictions.

This brief overview of future directions gives an impression of the complexity of the problem. Actual support of medical decisions in the treatment of cerebral aneurysms is a long term goal that requires involvement of experts from different disciplines. However, making the model too complex should be avoided; a balance should be found between including realistic properties and their simple approximation. After all, the variability of conditions for a single patient is already considerable in the course of a day because of different activity levels. This puts an interest in predicting a band of likely situations instead of fully detailed predictions for one particular condition. The improved understanding of flow and forces inside an aneurysm bulge that can now be obtained from simulation, may also stimulate research into the reverse process in which the question could be whether small changes in the flow would exist that can induce a process of gradual stabilization of the aneurysm, a form of self-healing that halts the progress of the disease. Reliability of the support that can be given to the medical decision process should remain the most important factor, requiring a detailed study of a sufficiently large set of patient-specific cases to reach confidence in the approach.

References

1. Angot, P., Bruneau, C.H., Frabrie, P. (1999) A penalization method to take into account obstacles in viscous flows. *Numerical Mathematics*, **81**: 497-520
2. Arthurs, K.M., Moore, L.C., Peskin, C.S., Pitman, E.B., Layton, H.E. (1998) Modeling arteriolar flow and mass transfer using the immersed boundary method. *Journal of Computational Physics*, **147**: 402-440
3. Baek, H., Jayaraman, M.V., Richardson, P.D., Karniadakis, G.E. (2009) Flow instability and wall shear stress variation in intracranial aneurysms. *Journal of the Royal Society Interface*, **7**: 967-988, doi:10.1098/rsif.2009.0476
4. Batchelor, G.K., (2007) An introduction to fluid dynamics. *Cambridge University Press*, ISBN: 9780521663960
5. Bazilevs, Y., Hsu, M.C., Zhang, Y., Wang, W., Kvamsdal, T., Hentschel, S., Isaksen, J.G. (2010) Computational vascular fluid-structure interaction: methodology and application to cerebral aneurysms. *Biomechanics and Modeling in Mechanobiology*, **9**: 481-498, doi: 10.1007/s10237-010-0189-7
6. Bernsdorf, J., Wang, D. (2009) Non-Newtonian blood flow simulation in cerebral aneurysms. *Computers and Mathematics with Applications*, **58**: 1024-1029
7. Berthelsen P.A., Faltinsen O.M. (2008) A local directional ghost cell approach for incompressible viscous flow problems with irregular boundaries. *Journal of Computational Physics*, **227**: 4354-4397
8. Bescós, J.O., Slob, M.J., Slump, C.H., Sluzewski, M., van Rooij, W.J. (2005) Volume measurement of intracranial aneurysms from 3D rotational angiography: improvement of accuracy by gradient edge detection. *American Journal of Neuroradiology*, **26**: 2569-2572
9. Boussel, L., Rayz, V., McCulloch, C.; Martin, A.; Acevedo-Bolton, G.; Lawton, M.; Higashida, R.; Smith, W.S.; Young, W.L.; Saloner, D. (2008) Aneurysm growth occurs at region of low wall shear stress: patient-specific correlation of hemodynamics and growth in a longitudinal study. *Stroke*, **39**: 2997-3002, doi: 10.1161/STROKEAHA.108.521617
10. Bridcut, R.R., Winder, R.J., Workman, A., Flynn, P. (2002) Assessment of distortion in a three-dimensional rotational angiography system. *The British Journal of Radiology*, **75**: 266-270
11. Brinjikji, W., Cloft, H., Lanzino, D.F., Kallmes, D.F. (2009) Comparison of 2D digital subtraction angiography and 3D rotational angiography in the evaluation of dome-to-neck ratio. *American Journal of Neuroradiology*, **30**: 831-834, doi: 10.3174/ajnr.A1444

12. Castro, M.A., Putman, C.M., Cebral, J.R. (2006) Computational fluid dynamics modeling of intracranial aneurysms: effects of parent artery segmentation on intra-aneurysmal hemodynamics. *American Journal of Neuroradiology*, **27**: 1703-1709
13. Castro, M.A., Putman, C.M., Sheridan, M.J., Cebral, J.R. (2009) Hemodynamic patterns of anterior communicating artery aneurysms: a possible association with rupture. *American Journal of Neuroradiology*, **30**: 297-302, doi: 10.3174/ajnr.A1323
14. Cebral, J.R., Castro, M.A., Burgess, J.E., Pergolizzi, R.S., Sheridan, M.J., Putman, C.M. (2005) Characterization of cerebral aneurysms for assessing risk of rupture by using patient-specific computational hemodynamics models. *American Journal of Neuroradiology*, **26**: 2550-2559
15. Cebral, J.R., Castro, M.A., Appanaboyina, S., Putman, C.M., Millan, D., Frangi, A.F. (2005) Efficient pipeline for image-based patient-specific analysis of cerebral aneurysms hemodynamics: technique and sensitivity. *IEEE Transactions on Medical Imaging*, **24**: 457-467, doi: 10.1109/TMI.2005.844159
16. Cebral, J.R., Mut, F., Weir, J., Putman, C. (2011) Quantitative characterization of the hemodynamic environment in ruptured and unruptured brain aneurysms. *American Journal of Neuroradiology*, **32**: 145-151, doi: 10.3174/ajnr.A2419
17. Cebral, J.R., Mut, F., Sforza, D., Löhner, R., Scrivano, E., Lylyk, P., Putman, C.M. (2011) Clinical application of image-based CFD for cerebral aneurysms. *International Journal for Numerical Methods in Biomedical Engineering*, **27**: 977-992, doi: 10.1002/cnm.1373
18. Cheny, Y., Botella, O. (2010) The LS-STAG method: a new immersed boundary/level-set method for the computation of incompressible viscous flows in complex moving geometries with good conservation properties. *Journal of Computational Physics*, **229**: 1043-1076, doi:10.1016/j.jcp.2009.10.007
19. Cortez, R., Fauci, L., Cowen, N., Dillon, R. (2004) Simulation of swimming organisms: coupling internal mechanics with external fluid dynamics. *Computing in Science and Engineering*: 38-45
20. Dillon, R., Fauci, L., Fogelson, A., Gaver III, D. (1996) Modeling biofilm processes using the immersed boundary method. *Journal of Computational Physics*, **129**: 57-73
21. Doenitz, C., Schebesch, K.M., Zoephel, R., Brawanski, A. (2010) A mechanism for the rapid development of intracranial aneurysms: a case study. *Neurosurgery*, **67**: 1213-1221
22. Duijvenboden, S., Schaafsma, A., Geurts, B.J. (2011) Usefulness of Schrodingerś operator for assessing new parameters in Transcranial Doppler sonography. Internal Report, University of Twente, The Netherlands
23. Ferguson, G.G. (1970) Turbulence in human intracranial saccular aneurysms. *Journal of Neurosurgery*, **33**: 485-497
24. Gambaruto, A.M., Janela J., Moura A., Sequeira A. (2011) Sensitivity of hemodynamics in a patient specific cerebral aneurysm to vascular geometry and blood rheology. *Mathematical Biosciences and Engineering*, **8**: 409-423, doi:10.3934/mbe.2011.8.409
25. Gao, T., Tseng, Y.H., Lu, X.Y. (2007) An improved hybrid Cartesian/immersed boundary method for fluid-solid flows. *International Journal for Numerical Methods in Fluids*, **55**: 1189-1211, doi: 10.1002/fld.1522
26. Geers, A.J., Larrabide, I., Radaelli, A.G., Bogunovic, H., Kim, M., Gratama van Andel, H.A.F., Majoie, C.B., VanBavel, E., Frangi, A.F. (2011) Patient-specific computational hemodynamics of intracranial aneurysms from 3D rotational angiography and CT angiography: an in vivo reproducibility study, *American Journal of Neuroradiology*, **32**: 581-586, doi: 10.3174/ajnr.A2306
27. Geurts, B.J. (2003) Elements of direct and Large-Eddy simulation. *Edwards Publishing*, ISBN: 1930217072

28. Gijsen, F.J.H., van de Vosse, F.N., Janssen, J.D. (1999) The influence of the non-Newtonian properties of blood on the flow in large arteries: steady flow in a carotid bifurcation model. *Journal of Biomechanics*, **32**: 601-608
29. Goubergrits, L., Schaller, J., Kertzscher, U., van der Bruck, N.; Poethkow, K.; Petz, Ch.; Hege, H.-Ch.; Spuler, A. (2012) Statistical wall shear stress maps of ruptured and unruptured middle cerebral artery aneurysms. *Journal of the Royal Society Interface*, Vol. 9, No. 69, pp. 677-688. doi: 10.1098/rsif.2011.0490
30. Gondalez, R.C., Woods, R.E. (2008) Digital image processing. *Pearson Education*, ISBN: 9780135052679
31. Grass, M., Koppe, R., Klotz, E., Proksa, R., Kuhn, M.H., Aerts, H., Op de Beek, J., Kemkers, R. (1999) Three-dimensional reconstruction of high contrast objects using C-arm image intensifier projection data. *Computerized Medical Imaging and Graphics*, **23**: 311-321
32. Griffith, B.E., Peskin, C.S. (2005) On the order of accuracy of the Immersed Boundary method: higher order convergence rates for sufficiently smooth problems. *Journal of Computational Physics*, **208**: 75-105, doi:10.1016/j.jcp.2005.02.011
33. Haralick, R.M., Shapiro, L.G. (1992) Computer and robot vision, Vol. I, *Addison-Wesley*
34. Hendrikse, J., van Raamt, A.F., van der Graaf, Y., Mali, W.P.T.M., van der Grond, J. (2005) Distribution of cerebral blood flow in the Circle of Willis. *Radiology*, **235**: 184-189, doi: 10.1148/radiol.2351031799
35. Hirsch, C. (1988) Numerical computation of internal and external flows. *Wiley and Sons*, ISBN: 0471917621
36. Hollnagel, D.I., Summers, P.E., Poulikakos, D., Kollias, S.S. (2009) Comparative velocity investigations in cerebral arteries and aneurysms: 3D phase-contrast MR angiography, laser Doppler velocimetry and computational fluid dynamics. *NMR in Biomedicine*, **22**: 795-808, doi: 10.1002/nbm.1389
37. Iaccarino, G., Verzicco, R. (2003) Immersed boundary technique for turbulent flow simulations. *Applied Mechanics Reviews, ASME*, **56**: 331-347, doi: 10.1115/1.1563627
38. Janela, J., Moura, A., Sequeira, A. (2010) A 3D non-Newtonian fluid-structure interaction model for blood flow in arteries. *Journal of Computational and Applied Mathematics*, **234**: 2783-2791, doi: 10.1016/j.cam.2010.01.032
39. Kamath, S. (1981) Observations on the length and diameter of vessels forming the Circle of Willis. *Journal of Anatomy*, **133**: 419-423
40. Kang, S., Iaccarino, G., Ham, G., Moin, P. (2009) Prediction of wall-pressure fluctuation in turbulent flows with an immersed boundary method. *Journal of Computational Physics*, **228**: 6753-6772, doi:10.1016/j.jcp.2009.05.036
41. Keetels, G.H., DÓrtona, U., Kramer, W., Clercx, H.J.H., Schneider, K., van Heijst, G.J.F. (2007) Fourier spectral and wavelet solvers for the incompressible Navier-Stokes equations with volume-penalization: convergence of a dipole-wall collision. *Journal of Computational Physics*, **227**: 919-945, doi: 10.1016/j.jcp.2007.07.036
42. Khadra, K., Angot, P., Parneix, S., Caltagirone, J.P. (2000) Fictitious domain approach for numerical modelling of Navier-Stokes equations. *International Journal for Numerical Methods in Fluids*, **34**: 651-684, doi: 10.1002/1097-0363
43. Kim, Y., Peskin, C.S. (2006) 2-D parachute simulation by the immersed boundary method. *SIAM Journal of Scientific Computing*, **28**: 2294-2312, doi: 10.1137/S1064827501389060
44. Koffijberg, H., Buskens, E., Algra, A., Wermer, M.J.H., Rinkel, G.J.E. (2008) Growth rates of intracranial aneurysms: exploring constancy. *Journal of Neurosurgery*, **109**: 176-185, doi: 10.3171/JNS/2008/109/8/0176

45. Kosugi, Y., Goto, T., Ikebe, J., Joshita, H., Takakura, K. (1983) Sonic detection of intracranial aneurysm and AVM. *Stroke*, **14**: 37-42
46. Kovalev, K. (2005) Unstructured hexahedral non-conformal mesh generation. *PhD Thesis*, Vrije University of Brussels
47. Kroon, D.J., Slump, C.H., Sluzewski, M., van Rooij, W.J. (2006) Image based hemodynamics modelling of cerebral aneurysms and the determination of the risk of rupture. *SPIE Medical Imaging 2006: Physiology, Function, and Structure from Medical Images*, **6143**, Manduca, A., Amini, A.A. (Ed.), Proc. of SPIE, 61432B, doi: 10.1117/12.648062
48. Ku, D.N. (1997) Blood flow in arteries. *Annual Review of Fluid Mechanics*, **29**: 399-434
49. Kurokawa, Y., Abiko, S., Watanabe, K. (1994) Noninvasive detection of intracranial vascular lesions by recording blood flow sounds. *Stroke*, **25**: 397 - 402, doi: 10.1161/01.STR.25.2.397
50. Lai, M.C., Peskin, C.S. (2000) An immersed boundary method with formal second-order accuracy and reduced numerical viscosity. *Journal of Computational Physics*, **160**: 705-719, doi:10.1006/jcph.2000.6483
51. Li, Y., Yun, A., Kim, J. (2012) An immersed boundary method for simulating a single axisymmetric cell growth and division. *Journal of Mathematical Biology*, **65**: 653-675, doi: 10.1007/s00285-011-0476-7
52. Liu, Q., Vasilyev, O.V. (2007) A Brinkman penalization method for compressible flows in complex geometries. *Journal of Computational Physics*, **227**: 946-966, doi: 10.1016/j.jcp.2007.07.037
53. Löhner, R., Baum, J.D., Mestreau, E.L., Rice, D. (2007) Comparison of body-fitted, embedded and immersed 3-d Euler predictions for blast loads on columns. *American Institute of Aeronautics and Astrounatics*, **1113**: 1 - 22
54. Lopez Penha, D.J., Geurts, B.J., Stolz, S., Nordlund, M. (2011) Computing the apparent permeability of an array of staggered square rods using volume-penalization. *Computers and Fluids*, **51**: 157-173, doi: 10.1016/j.compfluid.2011.08.011
55. Lusseveld, E., Brilstra, E.H., Nijssen, P.C.G., van Rooij, W.J.J., Sluzewski, M., Tulleken, C.A.F., Wijnalda, D., Schellens, R.L.L.A., van der Graaf, Y., Rinkel, G.J.E. (2002) Endovascular coiling versus neurosurgical clipping in patients with a ruptured basilar tip aneurysm, *Journal of Neurology, Neurosurgery, and Psychiatry*, **73** : 591-593, doi:10.1136/jnnp.73.5.591
56. Mantha, A.R., Benndorf, G., Hernandez, A., Metcalfe, R.W. (2009) Stability of pulsatile blood flow at the ostium of cerebral aneurysms. *Journal of Biomechanics*, **42**: 1081-1087, doi:10.1016/j.jbiomech.2009.02.029
57. Metcalfe, R.W. (2003) The promise of computational fluid dynamics as a tool for delineating therapeutic options in the treatment of aneurysms. *American Journal of Neuroradiology Editorials*, **24**: 553-554
58. Mikhal, J., Lopez Penha, D.J., Stolz, S., Geurts, B.J. (2010) Application of an immersed boundary method to flow in cerebral aneurysms and porous media, In proceedings of the *Fluids Engineering Summer Meeting, ASME 2010*, Montreal, Canada, American Society of Mechanical Engineers, **31042**.
59. Mikhal, J., Slump, C.H., Geurts, B.J. (2012) Simulation of pulsatile flow in cerebral aneurysms: from medical images to flow and forces. Aneurysm, Yasuo Murai (Ed.), *InTech*, ISBN: 9789535107309, http://dx.doi.org/10.5772/47858
60. Mikhal, J., Geurts, B.J. (2011) Pulsatile flow in model cerebral aneurysms. *Procedia Computer Science*, **4**: 811-820, doi: 10.1016/j.procs.2011.04.086
61. Mikhal, J., Geurts, B.J. (2011) Bounding solutions for cerebral aneurysms. *New Archive for Mathematics*, **5**: 163-168

62. Mittal, R., Iaccarino, G. (2005) Immersed boundary methods. *Annual Review of Fluid Mechanics*, **37**: 239-261, doi: 10.1146/annurev.fluid.37.061903.175743
63. Moin, P., Kim, J. (1982) Numerical investigation of turbulent channel flow. *Journal of Fluid Mechacnics*, **118**: 341-377, doi: 10.1017/S0022112082001116
64. Moret, J., Kemkers, R., Op de Beek, J., Koppe, R., Klotz, E., Grass, M. (1998) 3D rotational angiography: clinical value in endovascular treatment. *Medicamundi*, **42**: 8-14
65. Mori, Y. (2008) Convergence proof of the velocity field for a Stokes flow immersed boundary method. Communications on Pure and Applied Mathematics. *Wiley Periodicals, Inc.*, Vol. LXI: 1213-1263
66. Morinishi, Y., Lund, T.S., Vasilyev, O.V., Moin, P. (1998) Fully conservative higher order finite difference schemes for incompressible flow. *Journal of Computational Physics*, **123**: 90-124
67. Oktar, S.O., Yücel, C., Karaosmanoglu, D., Akkan, K., Ozdemir, H., Tokgoz, N., Tali, T. (2006) Blood-flow volume quantification in internal carotid and vertebral arteries: comparison of 3 different ultrasound techniques with phase-contrast MR imaging. *American Journal of Neuroradiology*, **27**: 363-369
68. Oubel, E., De Craene, M., Putman, C.M., Cebral, J.R., Frangi, A.F. (2007) Analysis of intracranial aneurysm wall motion and its effects on hemodynamic patterns. *SPIE Medical Imaging 2007: Physiology, Function, and Structure from Medical Images*, **6511**: 10-11, Manduca, A, Hu, X.P. (Ed.), Proc. of SPIE
69. Oubel, E., Cebral, J.R., De Craene, M., Blanc, R., Blasco, J., Macho J., Putman, C.M., Frangi, A.F. (2010) Wall motion estimation in intracranial aneurysms. *Physiological Measurement*, **31**: 1119-1135, doi: 10.1088/0967-3334/31/9/004
70. Oyre, S., Ringgaard, S., Kozerke, S., Paaske, W.P., Erlandsen, M., Boesiger, P., Pedersen, E.M. (1998) Accurate noninvasive quantification of blood flow, cross-sectional lumen vessel area and wall shear stress by three-dimensional paraboloid modeling of magnetic resonance imaging velocity data. *Journal of the American College of Cardiology*, **32**: 128-134
71. Perktold, K., Peter, R., Resch, M. (1989) Pulsatile non-Newtonian blood flow simulation through a bifurcation with an aneurysm. *Biorheology*, **26**: 1011-1030
72. Perry, C.D. (2006) Giant cerebral aneurysm: 3D computed tomography angiography vs. rotational 3D digital subtraction angiography, *The Radiographer*, **53**: 27-29
73. Peskin, C.S. (2002) The immersed boundary method, *Acta Numerica*: 1-39, doi: 10.1017/S0962492902000077
74. Poethke, J., Goubergrits, L., Kertzscher, U., Spuler, A., Petz, Ch., Hege, H.Ch. (2008) Impact of imaging modality for analysis of a cerebral aneurysm: comparison between CT, MRI and 3DRA. *IFMBE Proceedings*, **22**: 1889-1893
75. Pope, S.B. (2003) Turbulent Flows. *Cambridge University Press*, ISBN: 0521598869
76. Quarteroni, A., Formaggia, L. (2004) Mathematical modelling and numerical simulation of the cardiovascular system. Handbook of Numerical Analysis, Vol. XII: 3-127, *North-Holland*
77. Ramalho, S., Moura, A., Gambaruto, A., Sequeira A. (2012) Sensitivity to outflow boundary conditions and level of geometry description for a cerebral aneurysm. *International Journal for Numerical Methods in Biomedical Engineering*, **28**: 697-713, doi: 10.1002/cnm.2461
78. Ringelstein, E.B., Kahlscheuer, B., Niggemeyer, E., Otis, S.M. (1990) Transcranial Doppler sonography: anatomical landmarks and normal velocity values. *Ultrasound in Medicine and Biology*, **16**: 745-761
79. Sarthou, A., Vincent, S., Caltagirone, J.P., Angot, P. (2008) Eulerian-Lagrangian grid coupling and penalty methods for the simulation of multiphase flows interacting with complex objects. *International Journal for Numerical Methods in Fluids*, **56**: 1093-1099, doi: 10.1002/fld.1661

80. Saylor, P.E. (1988) Leapfrog variants of iterative methods for linear algebraic equations. *Journal of Computational and Applied Mathematics*, **24**: 169-193
81. Seo, J.H., Mittal, R. (2011) A high-order immersed boundary method for acoustic wave scattering and low-Mach number flow-induced sound in complex geometries. *Journal of Computational Physics*, **230**: 1000-1019, doi:10.1016/j.jcp.2010.10.017
82. Sforza, D.M., Löhner, R., Putman, C., Cebral, J. (2010) Hemodynamic analysis of intracranial aneurysms with moving parent arteries: basilar tip aneurysms. *International Journal for Numerical Methods in Biomedical Engineering*, **26**: 1219-1227, doi: 10.1002/cnm.1385
83. Shashkov, M., Steinberg, S. (1995) Support-operator finite-difference algorithms for general elliptic problems. *Journal of Computational Physics*, **118**: 131-151, dx.doi.org/10.1006/jcph.1995.1085
84. Shojima, M., Oshima, M., Takagi, K., Torii, R., Hayakawa, M., Katada, K., Morita, A., Kirino, T. (2004) Magnitude and role of wall shear stress on cerebral aneurysm. Computational Fluid Dynamic study of 20 middle cerebral artery aneurysms. *Stroke*, **35**: 2500-2505, doi: 10.1161/01.STR.0000144648.89172.0f
85. Spalart, P.R. (1988) Direct simulation of a turbulent boundary layer up to Rteta = 1410. *Journal of Fluid Mechanics*, **187**: 61-98, doi: 10.1017/S0022112088000345
86. Sprengers, M.E., Schaafsma, J., van Rooij, W.J., Sluzewski, M., Rinkel, G.J.E., Velthuis, B.K., van Rijn, J.C., Majoie, C.B. (2008) Stability of intracranial aneurysms adequately occluded 6 months after coiling: a 3T MR angiography multicenter long-term follow-up study. *American Journal of Neuroradiololgy*, **29**: 1768-1774, doi: 10.3174/ajnr.A1181
87. Steinman, D.A., Milner, J.S., Norley, C.J., Lownie, S.P., Holdsworth, D.W. (2003) Image-based computational simulation of flow dynamics in a giant intracranial aneurysm. *American Journal of Neuroradiology*, **24**: 559-566
88. Torres, A.M., Michniewicz, R.J., Chapman, B.E., Young, G.A.R., Kuchel, P.W. (1998) Characterisation of erythrocyte shapes and sizes by NMR diffusion-diffraction of water: correlations with electron micrographs. *Magnetic Resonance Imaging*, **16**: 423-434
89. Tseng, Y.H., Ferziger, J.H. (2003) A ghost-cell immersed boundary method for flow in complex geometry. *Journal of Computational Physics*, **192**: 593-623, doi:10.1016/j.jcp.2003.07.024
90. Turowski, B., Macht, S., Kulcsár, Z., Hänggi, D., Stummer, W. (2011) Early fatal hemorrhage after endovascular cerebral aneurysm treatment with a flow diverter (SILK-Stent): Do we need to rethink our concepts? *Neuroradiology*, **53**: 37-41, doi: 10.1007/s00234-010-0676-7
91. Valen-Sendstad, K., Mardal, K.A., Mortensen, M., Reif, B.A.P., Langtangen, H.P. (2011) Direct numerical simulation of transitional flow in a patientspecific intracranial aneurysm. *Journal of Biomechanics*, **44**: 2826-2832
92. van Ooij, P., Guédon, A., Poelma, C., Schneiders, J., Rutten, M.C.M., Marquering, H.A., Majoie, C.B., vanBavel, E., Nederveen, A.J. (2012) Complex flow patterns in a real!size intracranial aneurysm phantom: phase contrast MRI compared with particle image velocimetry and computational fluid dynamics. *NMR in Biomedicine*, **25**: 14-26, doi: 10.1002/nbm.1706
93. van Rooij, W.J. (1998) Endovascular treatment of cerebral aneurysms. *PhD Thesis*, University of Utrecht, ISBN: 9039318182
94. van Rooij, W.J., Sprengers, M.E., Sluzewski, M., Beute, G.N. (2007) Intracranial aneurysms that repeatedly reopen over time after coiling: imaging characteristics and treatment outcome. *Neuroradiology*, **49**: 343-349, doi: 10.1007/s00234-006-0200-2
95. van Rooij, W.J., Sprengers, M.E., de Gast, A.N., Peluso, A.P.P., Sluzewski, M. (2008) 3D rotational angiography: the new gold standard in the detection of additional intracranial aneurysms. *American Journal of Neuroradiology*, **29**: 976-979, doi: 10.3174/ajnr.A0964

96. van Rooij, W.J., Peluso, J.P.P., Sluzewski, M., Beute, G.N. (2008) Additional value of 3D rotational angiography in angiographically negative aneurysmal subarachnoid hemorrhage: how negative is negative?. *American Journal of Neuroradiology*, **29**: 962-966, doi: 10.3174/ajnr.A0972
97. Vasilyev, O.V., Kevlahan, N.K.R. (2002) Hybrid wavelet collocation-Brinkman penalization method for complex geometry flows. *International Journal for Numerical Methods in Fluids*, **40**: 531-538, doi: 10.1002/fld.307
98. Venugopal, P., Valentino, D., Schmitt, H., Villablanca, J.P., Viñuela, F., Duckwiler, G. (2007) Sensitivity of patient-specific numerical simulation of cerebral aneurysm hemodynamics to inflow boundary conditions. *Journal of Neurosurgery*, **106**: 1051-1060
99. Verstappen, R.W.C.P., Veldman, A.E.P. (1997) Direct numerical simulation of turbulence at lower costs. *Journal of Engineering Mathematics*, **32**: 143-159
100. Verstappen, R.W.C.P., Veldman, A.E.P. (2003) Symmetry-preserving discretization of turbulent flow. *Journal of Computational Physics*, **187**: 343-368, doi:10.1016/S0021-9991(03)00126-8
101. Wanke, I., Dörfler, A., Forsting, M. (2008) Intracranial aneurysms. Intracranial vascular malformations and aneurysms. *Springer*, ISBN: 9783540329190
102. Watton, P., Raberger, N., Ventikos, Y. (2008) Computational model can predict aneurysm growth. *SPIE Newsroom*, doi: 10.1117/2.1200801.0999
103. Wiebers, D.O., Whisnant, J.P., Forbes, G. et al. (1998) Unruptured intracranial aneurysms – risk of rupture and risks of surgical intervention. International study of unruptured intracranial aneurysms investigators. *New England Journal of Medicine*, **339**: 1725-1733
104. Wiesent, K., Barth, K., Navab, N., Durlak, P., Brunner, T., Schuetz, O., Seissler, W. (2000) Enhanced 3-d-reconstruction algorithm for C-arm systems suitable for interventional procedures. *Medical Imaging, IEEE Transactions on*, **19**: 391-403
105. Young, B, Lowe, J.S., Stevens, A., Heath, J.W. (2006) Wheater's functional histology: a text and colour atlas, 5th Edition. *Elsevier*, ISBN: 9780443068508
106. Young, D.F., Munson, B.R., Okiishi, T.H. (1997) A brief introduction to fluid mechanics. *John Wiley and Sons, Inc.*, ISBN: 0471137715

Summary

The formation of aneurysms in the human brain is an important cerebrovascular disorder which affects a large number of people. In the US, for example, 2% of the population is estimated to have one or more cerebral aneurysms, which means 6 million individuals. People suffering from this condition develop a complex shaped bulge at a weak spot of the vessel wall. Over time the aneurysm bulge may grow, thereby increasing the risk of rupture which might lead to life-threatening intracranial hemorrhage. Diagnostic procedures available these days allow to visualize cerebral vessels and to detect even very small aneurysms. Decisions about treatment of a particular cerebral aneurysm are currently often made on the basis of location, shape and size of the bulge alone, relying largely on empirical knowledge and common practice.

Mathematical modeling and computational fluid dynamics can support the medical decision-making process. Simulation may add qualitative and quantitative insight into the structure of the flow and the pulsatile forces that develop. These predictions are obtained directly on the basis of the medical imagery that is available on a patient-specific basis. The three-dimensional geometry of the cerebral vasculature of a patient can be reconstructed from the recorded medical images. This 3D geometry can be used as input for simulating the flow. Parameters characterizing the flow of blood in the human brain include bio-physical properties such as viscosity, pulsation rhythms, flow rate and diameters of arteries in the area of interest. Numerical simulations of realistic flow under physiological conditions allow to analyze velocity patterns, pressure distribution and forces which influence the growth and possible rupture of the aneurysm.

In this thesis a computational model of blood flow in the human brain was developed and applied to the simulation of pulsatile flow through a vessel segment containing a cerebral aneurysm. The simulation strategy was developed in three main steps: (i) formulation of the numerical method for incompressible flow and testing on model geometries, (ii) inclusion of realistic flow domains obtained from segmented medical imagery and simulation of the stationary flow at physiologically realistic conditions and (iii) incorporation of realistic pulsatile

variation of the flow-rate through the affected vessel segment. We briefly discuss these three steps next.

The geometry of a segment of the cerebral vasculature is represented using an Immersed Boundary (IB) method. The so-called masking function plays a key role identifying points inside the brain tissue and points inside a vessel. Defining the masking function on a Cartesian grid yields a relatively fast way of distinguishing fluid and solid cells in the total computational domain in 3D. The masking function is used to formulate a volume penalization term in the Navier-Stokes equations, reminiscent of the Brinkman model for flow in porous media. By considering the limit in which the solid porous material becomes impenetrable to flow, an effective model for the complex vessel geometry in the brain is obtained. The IB method was validated for Poiseuille flow in a cylindrical pipe, showing first order convergence of the numerical solution to the analytical solution. The method was applied to curved vessels with and without a spherical aneurysm attached to it. Results at increasing spatial resolution were compared. It was observed that reliable predictions with a relative error of less than 10% in the velocity can be arrived at when about 16 or more grid cells cover the width of a vessel cross-section.

Simulating steady flow in realistic geometries requires the masking function to be reconstructed from medical images obtained, e.g., by 3D Rotational Angiography (3DRA). To define computational models for specific ‘suspect’ areas of specific patients, basic operations such as ‘cutting’ and (smooth) ‘connection’ of segments of blood vessels were developed. At a typical Reynolds number of $Re = 250$ we observed complex vortical structures in the flow inside and near the aneurysm bulge. We focused on the sensitivity of flow predictions on the steps needed to formulate the flow domain. We found that numerical manipulations of the domain, done sufficiently far from the region of interest, have a small influence on the computed velocity and pressure distribution near the actual aneurysm. Computational models that are about 2-3 times the size of the bulge upstream as well as downstream of the neck of the aneurysm were found to give robust flow solutions in the region of interest. To quantify uncertainty in the predictions due to uncertainty in the recorded imagery we introduced so-called bounding geometries. These are obtained by incorporating slightly perturbed geometries, e.g., using different segmentation values or including perturbations due to small movements of the patient during recording. We systematically generated bounding geometries leading to a set of practical bounding solutions, which can be used to indicate outcome-intervals for pressure and shear stresses. This idea can also be used to generate a robust, rough impression of the flow properties, together with practical upper- and lower bounds, at strongly reduced computational costs.

To complete the computational model we also included realistic pulsatile forcing. This was based on variations in the flow rate during a heart beat, measured near the aneurysm using Transcranial Doppler Sonography. We simulate pulsatile flow at different conditions by

changing the Reynolds number, i.e., we change the velocity of the blood flow as we assume the diameter of the artery and the viscosity of the blood to be constant. We observe a strong transition in the solution when increasing the Reynolds number in the physiologically realistic range. This transition appears in all sorts of flow quantities such as velocity components, pressure and shear stress and it is found to arise at any location in the selected vessel segment. Not only the values of pressure, velocity and shear stress are higher at higher Reynolds numbers but also the dynamics of the flow is more lively, containing a larger contribution from high-frequency variations. To quantify the transition we analyzed spectra of the computed solutions at different Reynolds numbers. We observed the tail of the spectrum to clearly decay less rapidly with frequency, at higher *Re*. Higher frequencies are absolutely but also relatively stronger at increased *Re*, which could point to the possibility of 'hearing' potentially 'dangerous' flows in already developed aneurysms. This appears a promising mechanism with which fast scanning and monitoring of patients may be realized in the future.

Samenvatting

De vorming van aneurysmes in de hersenen is een belangrijk ziektebeeld dat tal van mensen treft. In de Verenigde Staten alleen al heeft naar schatting 2% van de bevolking één of meer aneurysmes in de hersenen, waarmee zo'n 6 miljoen mensen gemoeid zijn. Mensen die aan deze aandoening lijden ontwikkelen een 'uitstulping', meestal met zeer complexe vorm, nabij een zwakke plek in een vaatwand. Deze uitstulping kan geleidelijk in omvang toenemen, waarmee het risico van een breuk in de vaatwand toeneemt en daarmee de kans op een levensbedreigende bloeding in de hersenen. Tegenwoordig kunnen diagnostische procedures in detail bloedvaten in de hersenen zichtbaar maken en zelfs de kleinste aneurysmes in kaart brengen. Besluiten aangaande de behandeling van een bepaald aneurysme worden vaak nog genomen louter op basis van de locatie, vorm en omvang van de uitstulping, waarbij men zich veelal baseert op empirische kennis en praktijkervaring.

Wiskundige modellering en numerieke vloeistofdynamica kunnen het medische beslissingsproces ondersteunen door zowel kwalitatieve als kwantitatieve inzichten in de structuur van de stroming en de pulserende krachten te leveren. Deze computervoorspellingen kunnen direct op basis van de geregistreerde medische beelden van een specifieke patiënt worden gedaan. De drie-dimensionale geometrie van de bloedvaten in de hersenen van een patiënt kan in detail worden gereconstrueerd en als input dienen van de simulatie van de stroming. Parameters die de stroming van bloed in de hersenen karakteriseren zijn onder andere bio-fysische eigenschappen zoals de viscositeit, het pulsatie ritme van het hart, het tijdafhankelijke debiet en de typische diameter van bloedvaten in het gebied rond het aneurysme. Numerieke simulaties van de daadwerkelijke stroming onder fysiologische condities maken een analyse van het snelheidsveld, de drukverdeling en de krachten op de vaatwanden mogelijk en geven daarmee een beter begrip van de groei en mogelijke breuk van een aneurysme.

In dit proefschrift is een computermodel ontwikkeld waarmee de stroming van bloed in de hersenen kan worden gesimuleerd. Dit model is toegepast op de pulserende stroming in een deel van een bloedvat waar zich een aneurysme heeft ontwikkeld. De totale simulatie aanpak is in drie stappen ontwikkeld: (i) formulering van de numerieke methode voor incompress-

ibele stroming en het testen ervan op een aantal modelgeometrieën, (ii) uitbreiding naar realistische stromingsdomeinen die uit gesegmenteerde medische beelden zijn gereconstrueerd en simulatie van de stationaire stroming onder fysiologisch realistische condities en (iii) opnemen van het effect op de stroming van een realistisch pulserend debiet door het aangetaste segment van het bloedvat. Deze drie onderdelen zullen in meer detail worden besproken.

De geometrie van een deel van de bloedvaten in de hersenen is weergegeven met een Immersed Boundary (IB) methode. Hierin speelt de zogenaamde masking functie een centrale rol bij het identificeren van locaties die hetzij tot het hersenweefsel dan wel tot de bloedvaten behoren. Wanneer de masking functie op een Cartesisch rooster wordt gedefinieerd verkrijgen we een efficiënte en snelle methode om 'vloeistof' en 'vaste' cellen in het totale 3D domein aan te geven. De masking functie is gebruikt om een volume-penalisatie term in de Navier-Stokes vergelijkingen te formuleren die veel gelijkenis vertoont met het Brinkman model voor poreuze stromingen. Door de limiet te nemen waarin het poreuze model nagenoeg ondoordringbaar wordt voor stroming kan men een effectjef model voor de complexe bloedvatgeometrie in de hersenen afleiden. De IB methode is gevalideerd voor Poiseuille stroming in een cilindrische pijp, waarbij eerste-orde convergentie van de numerieke oplossing naar de analytische oplossing en zijn gradiënt is aangetoond. De methode is ook toegepast op gekromde bloedvaten, zowel met als zonder een bolvormige uitstulping. Resultaten bij verschillende ruimtelijke resoluties zijn met elkaar vergeleken. Betrouwbare resultaten met een relatieve fout van minder dan 10% kunnen worden verkregen wanneer zo'n 16 of meer roostercellen worden gebruikt over de breedte van een dwarsdoorsnede.

Simulaties van stationaire stroming in realistische geometrieën vereisen dat de masking functie voor het stromingsdomein gereconstrueerd wordt uit de beschikbare medische beelden, bijvoorbeeld verkregen met 3D Rotational Angiography (3DRA). Om computermodellen voor specifieke probleemgebieden van specifieke patiënten te definiëren zijn basisoperaties zoals het 'snijden' en het (glad) 'verbinden' van stukken bloedvat ontwikkeld. Bij een typisch Reynolds getal van $Re = 250$ laten simulaties complexe vortex-structuren in de stroming in en nabij de aneurysme uitstulping zien. We hebben de afhankelijkheid van numerieke voorspellingen onderzocht ten gevolge van de verschillende stappen die genomen dienen te worden om tot de definitie van het stromingsdomein te komen. De resultaten laten zien dat deze afhankelijkheid tamelijk gering is (relatieve afwijkingen minder dan 1% in de snelheden) mits numerieke manipulaties van de medische beelden bij de domeindefinitie voldoende ver van de locatie van het aneurysme zelf plaatsvinden. Computermodellen met een grootte van ongeveer 2-3 keer de omvang van de uitstulping zowel in de richting stroomopwaarts als stroomafwaarts geven een robuuste indruk van de stroming in en nabij het aneurysme. Om de betrouwbaarheid van voorspellingen ten gevolge van onzekerheden in de medische uitgangsbeelden te kwantificeren zijn zogenaamde 'grensgeometrieën' geïntroduceerd. Deze worden verkregen door nabije geometrieën te beschouwen, verkregen door kleine, systematische veranderingen in de masking functie toe te laten. Dergelijke verstoringen kunnen op-

treden, bijvoorbeeld door verandering van de segmentatie-parameters bij beeldverwerking, of door kleine bewegingen van de patiënt gedurende de 3DRA opname. We hebben systematisch grensgeometrieën gegenereerd en de daarbij behorende numerieke oplossingen geanalyseerd. Daarmee kunnen intervallen voor bijvoorbeeld drukval en maximale schuifspanning worden aangegeven die de afhankelijkheid van geometrie-onbetrouwbaarheid karakteriseren. Dit idee kan ook worden gebruikt om een robuuste, ruwe indruk van de stroming, met praktische boven- en ondergrenzen te verkrijgen tegen sterk gereduceerde rekenkosten.

Een compleet computermodel voor de doorstroming van aneurysmes verondersteld dat ook de realistische pulserende aandrijving van de stroming wordt meegenomen. Deze aandrijving wordt gekarakteriseerd door variaties in de bloedstroomsnelheid tijdens een hartslag, die gemeten kunnen worden met behulp van Transcranial Doppler Sonography. We hebben de pulserende stroming onder verschillende condities gesimuleerd door het Reynoldsgetal te variëren. Daarbij is alleen de stroomsnelheid veranderd omdat de diameter van het bloedvat en de viscositeit van het bloed constant worden verondersteld. We kunnen een sterke transitie waarnemen in de oplossing wanneer het Reynolds getal, binnen het fysiologisch realistische gebied, wordt verhoogd. Deze transitie treedt in allerlei stromingsgrootheden op, zoals de snelheid, druk en schuifspanning, en wordt op alle locaties nabij het aneurysme waargenomen. Bij deze transitie nemen niet alleen de amplitudes van druk en snelheden toe maar ook wordt de dynamica van de stroming veel levendiger en bevat de oplossing een relatief grotere bijdrage van componenten met een hogere frequentie. Om de transitie te kwantificeren zijn spectra van de numerieke oplossing bepaald bij verschillende Reynoldsgetallen. We observeerden daarbij dat de staart van het spectrum een duidelijk minder scherpe afval met frequentie laat zien wanneer *Re* toeneemt. Hogere frequenties zijn absoluut maar ook relatief sterker bij hogere Reynoldsgetallen wat zou kunnen wijzen op de mogelijkheid om ‘gevaarlijke’ stromingen in reeds ontwikkelde aneurysmes in de hersenen te horen. Dit lijkt een kansrijk mechanisme waarmee snelle scanning en monitoring van patiënten kan worden gerealiseerd in de toekomst.

Acknowledgements

I am grateful to my promotors Bernard Geurts and Kees Slump for their enthusiastic supervision during my project. You supported me to develop this work starting from a great idea: to help people. You encouraged me to choose my own direction and realize my ideas during my PhD at the University of Twente. Scientific elegance, a dose of hard work and discipline, and an understanding of medical reality came together in this wonderful project thanks to both of you - I am happy that we could work on this as a team.

My thesis would have been quite different without the help and support from Hans Kuerten and Rajat Mittal. Hans, you helped me realize that precision is essential, even in the smallest of details - I appreciate your patience in showing me how to speed-up and parallelize simulations. My enthusiasm for the application of computational modeling to medical problems was stimulated during the few but inspiring discussions I could have with Rajat - your passion for your work is contagious.

I would also like to thank the members of MMS and SAS for the good working atmosphere and the nice activity-days together. The whole staff in the Department of Applied Mathematics I will remember for their frequent interest shown in my work - it was great to be part of such an international community. Many thanks go to all my former office mates in both groups where I worked and to my tea- and lunch- 'teams': Bettina, David, Lilya, Marcel, Nastya and Sid at the Mathematics Department and Bianca, Meiru, Rita and Xiaoying at SAS. I will keep warm memories of the secretaries Mariëlle, Linda, Anneke and Sandra who always had time to patiently listen to some of my worries and found practical answers for most of them. I would also like to thank Marc Berenschot and Geert Jan Laanstra for often-needed help with my laptop, and Henny Kuipers for setting up my experiment and supporting me a lot while working on it.

For the past three years I spent most Monday evenings with the MSO symphonic orchestra playing all sorts of classical music. I am very thankful to all the MSO members, and to the second violins in particular for the friendly atmosphere during our rehearsals, long musical

week-ends and of course our concerts. Personally, I would like to thank Jeanette Silvius and Sietske Vonck for the nice times we had over the years and especially during our trip to Italy in 2011, and our conductor Frans-Aert Burghgraef for showing a good example of a person loving his job and being infinitely enthusiastic about it.

A special thank-you goes to all my friends in Ukraine, and to my sister Lena, her husband Kolya and their son Vadik and my brother Andrey, his wife Julia and their son Maxim, born while I was in the Netherlands. Some of you could come to visit me in the Netherlands, many others supported me by listening and talking to me via Skype. I would like to thank especially Olya, Olchik, Olik, Lida, Vika, Lena and Tanya for staying my closest friends even though we could be scattered all over the world - it was always special to come back home to Kharkov and find all of you there to welcome me and to be with me.

My deepest thanks are for my parents - for their permanent and unconditional support. The many hours in Skype which you spent with me talking, listening, suggesting, worrying, laughing gave a bit of home even while being so far from you. I am happy we could also travel together, exploring Europe and visiting new places, giving us new stories and hundreds of gigabytes of photos to share. Мама и Папа, спасибо вам за всё, что вы для меня делали и делаете, за вашу поддержку и понимание, и за то, что у вас всегда есть время для меня.

Julia Mikhal
Юлия Михаль

Enschede,
September 2012

About the author

Julia Mikhal was born on June 6 1984 in Kharkiv, Ukraine. She obtained her secondary education at Physics and Mathematics Lyceum #27 in 2001. She also studied at music school and in 1998 got her diploma in violin.

In 2001 she started studies in Mathematics at the National University of Kharkiv, Ukraine. She graduated, with honors, in 2006 with the MSc thesis ”Discrete almost periodic sets” in the field of Theory of Functions and Functional Analysis.

During her Master studies she became involved in teaching and after graduation in 2006 she obtained a position of Teaching Assistant at the National University of Kharkiv. Next to this she worked at a software company developing Geo-Informational Systems. In these years her interest in the application of mathematics to problems of real life developed.

In 2008 she started her PhD research under supervision of Prof. Bernard Geurts in the group Multiscale Modeling and Simulation at the University of Twente, The Netherlands. She worked on the development and application of a new immersed boundary method for the computational modeling and analysis of blood flow in cerebral aneurysms. In collaboration with Prof. Kees Slump from the Signals and Systems group at the University of Twente this methodology could be applied to realistic medical cases. The results of her work on a new method for the simulation of blood flow in cerebral aneurysms are presented in this thesis.

List of publications

Refereed journals

- Transition of pulsatile flow in cerebral aneurysms, Mikhal, J., Geurts, B.J. (2012) Submitted to *Journal of Biomechanics*
- Flow predictions in cerebral aneurysms based on geometry reconstruction from 3D rotational angiography, Mikhal, J., Kroon, D.J., Slump, C.H., Geurts, B.J. (2012) Submitted to *International Journal for Numerical Methods in Biomedical Engineering*
- Development and application of a volume penalization immersed boundary method for the computation of blood flow and shear stress in model aneurysms, Mikhal, J., Geurts, B.J. (2011) Submitted to *Journal of Mathematical Biology*
- Pulsatile flow in model cerebral aneurysms, Mikhal, J., Geurts, B.J. (2011) *Procedia Computer Science*, **4**: 811-820
- Bounding solutions for cerebral aneurysms, Mikhal, J., Geurts B.J. (2011) *New Archive for Mathematics*, **5**: 163-170

Book chapter

- Simulation of pulsatile flow in cerebral aneurysms: from medical images to flow and forces, Mikhal, J., Slump, C.H., Geurts, B.J. (2012) *Aneurysm*, Y. Murai (Ed.), InTech, ISBN: 978-953-51-0730-9, doi: http://dx.doi.org/10.5772/47858

Conference proceedings

- Development of an immersed boundary method for pulsatile flow predictions in cerebral aneurysms, Mikhal, J., Slump, C.H., Geurts, B.J. (2012) *VPH 2012*, London, September 18-20, 2012

- Immersed boundary method for pulsatile flow in cerebral aneurysms, Mikhal, J., Geurts, B.J. (2012) *ECCOMAS 2012*, Vienna, September 10-14, 2012
- Pulsatile flow patterns in cerebral aneurysms, Mikhal, J., Geurts, B.J. (2012) *ESB 2012*, Lisbon, July 1-4, 2012
- Tomographic immersed boundary method for permeability prediction of realistic porous media: Simulation and experimental validation, Lopez Penha, D.J., Geurts, B.J., Nordlund, M., Kuczaj, A.K., Zinovik, I., Winkelmann, C., Mikhal, J. (2012) *ICPM 2012*, Potsdam, June 17-22, 2012
- Simulation of pulsatile flow in cerebral aneurysm, Mikhal, J., Geurts, B.J. (2012) *National Mathematics Days NWD 2012*, Noordwijkerhout, February 3-4, 2012
- Simulation of realistic pulsatile flow in cerebral aneurysms, Mikhal, J., Geurts, B.J. (2011) *Euromech 529 Cardiovascular Fluid Mechanics*, Cagliari, June 27-29, 2011
- Development of an immersed boundary method for analyzing pulsatile flow in cerebral aneurysms, Mikhal, J., Geurts, B.J. (2011) *WSC Spring Day*, Delft, June 6, 2011
- Immersed boundary method for pulsatile flow in cerebral aneurysms, Mikhal, J., Geurts, B.J. (2011) *Dutch Mathematical Congress NMC 2011*, Enschede, April 14-15, 2011
- Prediction of blood flow in cerebral aneurysms using the immersed boundary method, Mikhal, J., Geurts, B.J. (2010) *KKMP 2010*, Poznan, September 5-9, 2010
- Application of an immersed boundary method to flow in cerebral aneurysms and porous media, Mikhal, J., Lopez Penha, D.J., Stolz, S., Geurts, B.J. (2010) *ASME and FEDSM-ICNMM 2010*, Montreal, Canada, August 1-4, 2010, Refereed 31042
- Immersed boundary method predictions of shear stresses for different flow topologies occurring in cerebral aneurysms, Mikhal, J., Lopez Penha, D.J., Slump, C.H., Geurts, B.J. (2010) *ECCOMAS CFD 2010*, Lisbon, June 14-17, 2010, Refereed 01156, J.C.F. Pereira, A. Sequeira (Eds)
- Shear stress predictions for a model aneurysm using the immersed boundary method, Mikhal, J., Geurts, B.J. (2010) *The 5th International Symposium on Biomechanics in Vascular Biology and Cardiovascular Disease*, Rotterdam, April 15-16, 2010